

EXPERIMENTAL AND THEORETICAL STUDIES ON THE ELECTRONIC PROPERTIES  
AND DISSOCIATION REACTIONS OF GAS-PHASE METAL OXIDE NITRATE  
COMPLEXES

by

THOMAS HINTON HESTER III

DANIEL J. GOEBBERT, COMMITTEE CHAIR

MICHAEL K. BOWMAN  
CHRISTOPHER S. BRAZEL  
CAROLYN J. CASSADY  
TIMOTHY S. SNOWDEN

A DISSERTATION

Submitted in partial fulfillment of the requirements  
for the degree of Doctor of Philosophy  
in the Department of Chemistry  
in the Graduate School of  
The University of Alabama

TUSCALOOSA, ALABAMA

2016

Copyright Thomas Hinton Hester III 2016  
ALL RIGHTS RESERVED

## ABSTRACT

This dissertation discusses dissociation studies performed on various gas-phase transition and main group metal nitrate anion complexes using a tandem mass spectrometer. The dissociation of these complexes, via consecutive loss of  $\text{NO}_2^\bullet$ , results in the formation of multiple metal-oxygen bonds. The dissertation focuses primarily on the metal oxide products in an attempt to gain a better understanding of the nature of metal-oxygen bonds, with an emphasis on the assignment of oxidation states for the atoms in these species.

The dissociation behavior for each system was found to be characteristic to the metal in that system. Specifically, the elimination of  $\text{NO}_2^\bullet$  results in abstraction of  $\text{O}^{\bullet-}$  by the metal and formation of a metal-oxygen bond. The formation of this bond can result in oxidation of the metal, reduction of the metal, or show an absence of redox activity for the metal.

The main group metals, such as aluminum, gallium, and the pseudo-main group metal zinc, have valences lower in energy than that of the  $\text{O}^{\bullet-}$  ligand and do not undergo oxidation or reduction upon metal-oxygen bond formation. The oxygen ligand retains the radical and is the reactive site in those systems, illustrated by the observed high degree of dissociation. The late transition metal, copper(II), has a low-lying  $3d$  vacancy that allows metal reduction upon metal-oxygen bond formation. The copper(I) system, with its full  $3d$  valence shows dissociation behavior identical to that of the main group metals.

The nickel(II) cation has a nearly degenerate valence to that of the  $\text{O}^{\bullet-}$  ligand, resulting in dissociation similar to that of the main group metals. The dissociation patterns are similar

because the  $O^{\cdot-}$  ligands are the primary reactive sites in the nickel system. Metal reduction can occur upon elimination of atomic and molecular oxygen from some complexes. This metal reduction occurs at relatively low energy due to the low-lying  $3d$  vacancies for nickel. There are two instances of electron transfer that result in partial metal and partial ligand reduction, due to the near degeneracy of the valences for the nickel cation and  $O^{\cdot-}$  ligand. The unusual, half-integer values for the oxidation state assignments in these two cases introduce a larger unanswered question of, “What do the oxidation states tell us about these types of metal oxide systems?”

Early-to-mid transition metals, such as chromium through cobalt, undergo metal oxidation upon metal-oxygen bond formation. These metals have high energy valence occupancies relative to the valence of the  $O^{\cdot-}$  ligand. An electron transfers from the metal  $3d$  subshell to the  $2p$  subshell of the oxygen ligand, reducing it to an  $O^{2-}$  ligand. Metal reduction can occur for these systems upon elimination of atomic and molecular oxygen, but it occurs at high energy due to the high energy  $3d$  subshell.

## DEDICATION

This dissertation is dedicated simply to those who read and enjoy it.

## LIST OF ABBREVIATIONS AND SYMBOLS

*	anti-bonding orbital (subscript)
→	redox or dissociation reaction arrow
°	degrees, as in angle
•	radical electron
Δ	change in or difference
∇ <sup>2</sup>	symbol for electron kinetic energy
-	hyphen or signifies a bond
—	negative or signifies a bond
+	addition symbol, plus, positive charge
×	multiplication symbol, times
=	equals symbol
brackets	contain ionic complex formula
parentheses	contain a discrete ligand (in molecular formula)
roman numerals	signify oxidation state of metal
subscript	signifies number of atoms or groups
superscript	signifies spin multiplicity, isotope, charge, number of electrons in orbital
<sup>1</sup> S	term symbol for singlet O atom
<sup>3</sup> P	term symbol for triplet O atom
Å	Ångstrom, unit of length, 10 <sup>-10</sup> meters

AC	alternating current, typically radio frequency
AO	atomic orbital
$\alpha$	alpha-spin electron
B3LYP	Becke 3-parameter Lee-Yang-Parr, hybrid functional for DFT
$b_m$	$b$ -type ion with subscript $m$ for number of monomer units
$\beta$	beta-spin electron
CID	collision-induced dissociation
c.m.	center-of-mass frame
$d$	notation for atomic orbital with quantum number $l=2$
DC	direct current
DFT	density functional theory
$\delta$	notation for molecular orbital with $d$ symmetry
$e$	charge of an electron, elementary charge, $1.602 \times 10^{-19}$ Coulombs
E	energy
$\hat{E}$	energy operator
$E_{\text{cm}}$	center-of-mass frame energy
$E_{\text{elec}}$	electronic energy
$E_{\text{lab}}$	lab-frame energy
ERMS	energy-resolved mass spectrometry
ESI	electrospray ionization
eV	electron-volt, amount of energy an electron gains across a 1 V field
$eV_{\text{cm}}$	center-of-mass frame energy in units of electron-volts
$\epsilon_0$	vacuum permittivity, $8.85 \times 10^{-12}$ Farad per meter

$f$	notation for atomic orbital with quantum number $l=3$
g	gram, $10^{-3}$ kilogram, unit of mass
$\hat{H}$	Hamiltonian operator
HF	Hartree-Fock
HV	high voltage
$\hbar$	Planck's constant divided by $2\pi$
kV	kilovolt, $10^3$ volts, unit of energy
LCAO	linear combination of atomic orbitals
m	mass
$m$	integer
$m_e$	mass of an electron, $9.11 \times 10^{-31}$ kilograms
$m/z$	mass-to-charge ratio, atomic mass unit per elementary charge
min	minute
$m_{\text{ion}}$	mass of ion
mL	milliliter, $10^{-3}$ liters or $10^{-6}$ cubic meters, unit of volume
mM	millimolar, $10^{-3}$ moles per liter, unit of concentration
MO	molecular orbital
$m_{\text{target}}$	mass of target gas
mTorr	millitorr, $10^{-3}$ Torr or 0.133 Pascals, unit of pressure
$\mu\text{L}$	microliter, $10^{-6}$ liters or $10^{-9}$ cubic meters, unit of volume
$n$	integer
$\text{net}(\alpha - \beta)$	value for difference in $\alpha$ -spin and $\beta$ -spin density within an orbital
NPA	natural population analysis

$N_e$	number of electrons
o2	octopole 2
p	notation for atomic orbital with quantum number $l=1$
PEG	polyethylene glycol
$\Phi(\mathbf{r})$	wavefunction containing only electronic coordinates
$\phi(\mathbf{r})$	wavefunction for a single electron
$\pi$	notation for molecular orbital with $p$ symmetry, irrational number 3.14
$\Psi(\mathbf{R},\mathbf{r})$	wavefunction containing nuclear and electronic coordinates
$\psi(\mathbf{R})$	wavefunction containing only nuclear coordinates
$\Sigma$	sum of
$\Pi$	product of
Q1	Quadrupole 1
Q1MS	Quadrupole 1 mass spectrometry
Q3	Quadrupole 3
QoQ	Quadrupole-octopole-Quadrupole configuration mass spectrometer
Q-TOF	Quadrupole-time-of-flight configuration mass spectrometer
R	nuclear coordinate
r	electron coordinate
$R_{\text{avg}}$	average distance between metal and ligand
$\rho(\mathbf{r})$	symbol for electron density
s	notation for atomic orbital with quantum number $l=0$
SCF	self-consistent field
$\sigma$	notation for molecular orbital with $s$ symmetry

Torr	133 Pascals, unit of pressure
TS	transition state
(U)	theoretical calculation performed using unrestricted wavefunction
V	volt, unit of potential energy
x	integer
Z <sub>A</sub>	nuclear charge
ZPE	zero-point vibrational energy

## ACKNOWLEDGMENTS

I have to acknowledge three guiding factors in my life, in no certain order: my mother who showed me to be considerate, my father who taught me to be deliberate, and my grandmother who made me to be persistent. I wouldn't have made it through the toughest period of my life, with respect to the challenges of seeking a Ph.D. and an environment of poor health for me and others, without readily available family and friends. Three friends are especially important to me: Dr. Carl Saint-Louis, Daniel Castillo, and Dr. Chelsea Plummer. I met them all at Alabama and although they have already started other lives, they stay the same great people for conversation and reminiscing. My favorite group members, Dr. Dan Goebbert and Dr. C.J. Pruitt, have been really helpful to my slow growth in organization and time management and have been great friends besides. Every one of the people I mentioned was indispensable to my time at Alabama and it would have been a hollow victory to make it out without knowing them.

## CONTENTS

ABSTRACT.....	ii
DEDICATION.....	iv
LIST OF ABBREVIATIONS AND SYMBOLS .....	v
ACKNOWLEDGMENTS .....	x
LIST OF TABLES .....	xv
LIST OF FIGURES .....	xvi
CHAPTER 1. INTRODUCTION .....	1
1.1 Current Issues in Metal Oxide Studies.....	1
1.2 Formation of Metal Oxides.....	2
1.3 Previous Studies.....	3
1.4 Direction of Dissertation Research .....	5
1.5 References.....	7
CHAPTER 2. METHODS.....	9
2.1 Experimental Methods.....	9
2.1.1 Instrumentation .....	9
2.1.2 Operational Modes.....	12
2.2 Theoretical Methods .....	15
2.2.1 Outline of Computational Chemistry.....	15
2.2.2 Basis Sets .....	17
2.2.3 Post Hartree-Fock Methods .....	19
2.2.4 Molecular Properties.....	20

2.2.5 Computational Chemistry .....	21
2.3 References .....	21
CHAPTER 3. GALLIUM NITRATE ANION COMPLEXES .....	23
3.1 Introduction.....	23
3.2 Methods.....	25
3.3 Experimental Results .....	26
3.4 Theoretical Results.....	30
3.5 Gallium-Oxygen Bonding.....	34
3.6 Conclusions.....	36
3.7 References.....	37
CHAPTER 4. ZINC NITRATE ANION COMPLEXES .....	38
4.1 Introduction.....	38
4.2 Methods.....	40
4.3 Experimental Results .....	40
4.4 Theoretical Results.....	44
4.5 Zinc-Oxygen Bonding .....	46
4.6 Conclusions.....	51
4.7 References.....	52
CHAPTER 5. NICKEL NITRATE ANION COMPLEXES .....	54
5.1 Introduction.....	54
5.2 Methods.....	55
5.3 Experimental Results .....	56
5.4 Theoretical Results.....	60
5.5 Nickel-Oxygen Bonding .....	63
5.6 Conclusions.....	68

5.7	References.....	69
CHAPTER 6. COBALT NITRATE ANION COMPLEXES .....		70
6.1	Introduction.....	70
6.2	Methods.....	71
6.3	Experimental Results .....	71
6.4	Theoretical Results.....	76
6.5	Cobalt-Oxygen Bonding .....	79
6.6	Conclusions.....	86
6.7	References.....	86
CHAPTER 7. PROTONATED POLYETHYLENE GLYCOL .....		88
7.1	Introduction.....	89
7.2	Methods.....	91
7.3	Results.....	92
7.3.1	Collision-Induced Dissociation.....	95
7.3.2	Energy-Dependent Fragmentation .....	95
7.3.3	In-Source Fragmentation .....	99
7.4	Discussion .....	100
7.5	Conclusions.....	103
7.6	References.....	104
CHAPTER 8. DEPROTONATED POLYETHYLENE GLYCOL.....		106
8.1	Introduction.....	107
8.2	Methods.....	109
8.3	Results and Discussion .....	109
8.4	Conclusions.....	116
8.5	References.....	116

CHAPTER 9. CONCLUSIONS AND OUTLOOK .....	119
9.1 Summary of Dissociation Trends.....	119
9.2 Gallium System.....	122
9.3 Zinc System .....	123
9.4 Nickel System .....	125
9.5 Cobalt System .....	126
9.6 Future Outlooks .....	126
9.7 References.....	127
APPENDIX.....	128

## LIST OF TABLES

2.1	Common operational modes for the tandem mass spectrometer, TSQ-7000. The functions listed for each mass selector determines whether a QIMS spectrum, a CID spectrum, or an ERMS spectrum is produced. ...	12
4.1	Calculated electron configurations for zinc atom and orbital occupancies for unique oxygen atoms from a natural population analysis at the (U)B3LYP/6-311+G(df) level of theory. ....	47
5.1	Calculated electron configurations for nickel from a natural population analysis at the (U)B3LYP/6-311+G(3df) level of theory. ....	64
5.2	Calculated nickel 3 <i>d</i> spin density and atomic properties for nickel and oxygen from a natural population analysis at the (U)B3LYP/6-311+G(3df) level of theory. ....	65
6.1	Calculated atomic charges, excess spin values, and 3 <i>d</i> orbital occupancies for cobalt atom from a natural population analysis at the (U)B3LYP/6-311+G(3df) level of theory. ....	81
6.2	Calculated electron configurations for cobalt atom from a natural population analysis at the (U)B3LYP/6-311+G(3df) level of theory. ....	82
6.3	Calculated atomic charges, excess spin values, and 2 <i>p</i> orbital occupancies for unique oxygen atoms from a natural population analysis at the (U)B3LYP/6-311+G(3df) level of theory. ....	83
9.1	Overview of the dissociation reactions for the metal oxide nitrates. Observed losses are listed for each metal complex and the corresponding reduction event is given. The sequential loss of NO <sub>2</sub> <sup>•</sup> is observed for all metals studied, except for the metal complexes listed in that row. Complexes containing no nitrate ligands are labeled as “BARE”. ....	124

## LIST OF FIGURES

1.1	Two representative molecular orbital diagrams for metal oxide bond formation. Panel A shows the hypothetical diagram for CuO. Panel B shows the hypothetical diagram for $[\text{CrO}]^{2+}$ .....4	4
2.1	Representative schematic for the tandem mass spectrometer, TSQ-7000. Each region is labeled with relative pressures given in Torr. ....10	10
2.2	Representative spectra obtained for the various operational modes on the TSQ-7000. Each panel represents A) the Q1MS spectrum for a copper nitrate sample, B) the CID spectrum of $[\text{Cu}(\text{NO}_3)_3]^-$ , and C) the ERMS curves for $[\text{Cu}(\text{NO}_3)_3]^-$ dissociation. ....14	14
3.1	Representative Q1MS spectrum of gallium nitrate solution.....26	26
3.2	CID mass spectra of (A) $[\text{Ga}(\text{NO}_3)_4]^-$ , (B) $[\text{GaO}(\text{NO}_3)_3]^-$ , (C) $[\text{GaO}_2(\text{NO}_3)_2]^-$ , and (D) $[\text{GaO}(\text{NO}_3)_2]^-$ . Spectra were recorded using 1.00 mTorr of Ar collision gas at 30 eV <sub>lab</sub> for (A) and (B) and 50 eV <sub>lab</sub> for (C) and (D). ....28	28
3.3	Energy-dependent fragmentation spectra for dissociation of $[\text{Ga}(\text{NO}_3)_4]^-$ . ....29	29
3.4	Calculated relative energy differences for the decomposition of $[\text{Ga}(\text{NO}_3)_4]^-$ at the (U)B3LYP/6-311+G(df) level of theory. All energies include zero-point corrections. Atom colors: pink for gallium, blue for nitrogen, and red for oxygen. ....31	31
3.5	Potential energy diagram for $^3\text{O}_2$ elimination from $[\text{GaO}(\text{NO}_3)_3]^-$ . ....31	31
3.6	Potential energy diagram for $^1\text{O}_2$ elimination from $[\text{GaO}_2(\text{NO}_3)_2]^-$ . ....31	31
3.7	Hypothetical zero-order orbital interaction diagram illustrating the formation of $[\text{GaO}]^{2+}$ from $\text{Ga}^{3+}$ and $\text{O}^-$ . ....35	35

4.1	Representative Q1MS spectrum for the zinc nitrate solution. The inset shows an enlarged portion of the spectrum containing $[\text{Zn}(\text{NO}_3)_3]^-$ to highlight the isotope pattern for Zn. ....	41
4.2	Representative CID spectra for (A) $[\text{Zn}(\text{NO}_3)_3]^-$ and (B) $[\text{ZnO}(\text{NO}_3)_2]^-$ at 30 eV <sub>lab</sub> collision energy with 0.50 mTorr Ar collision gas. ....	42
4.3	ERMS spectrum for the dissociation of $[\text{Zn}(\text{NO}_3)_3]^-$ . ....	43
4.4	Calculated relative energy differences for the decomposition of $[\text{Zn}(\text{NO}_3)_3]^-$ at the (U)B3LYP/6-311+G(df) level of theory. All energies include zero-point corrections. Select bond lengths and charges for the metal and unique oxygen atoms are indicated. Atom colors: gray for zinc, blue for nitrogen, and red for oxygen. ....	45
4.5	Potential energy diagram for $^3\text{O}_2$ elimination from $[\text{ZnO}(\text{NO}_3)_2]^-$ . All energies include zero-point corrections. Select bond lengths and NPA charges are indicated. ....	45
4.6	Potential energy diagram for $^3\text{O}_2$ elimination from $[\text{ZnO}_2(\text{NO}_3)]^-$ . Select bond lengths and NPA charges are indicated. Black lines indicate isomerization over the transition state barrier, TS1, via O atom transfer from the nitrate ligand to the reactive $\text{O}^{\bullet-}$ ligand. Blue lines indicate isomerization over TS2 via O-O bond formation to yield an $\text{O}_2^{\bullet-}$ ligand. ....	47
4.7	Hypothetical molecular orbital diagram for the formation of $[\text{ZnO}]^+$ from $\text{Zn}^{2+}$ and $\text{O}^{\bullet-}$ . The relative orbital energies suggest the zinc atom is neither oxidized nor reduced upon bond formation with oxygen and the unpaired electron remains on the oxygen atom. ....	50
5.1	Representative Q1MS spectrum of nickel nitrate solution. ....	56
5.2	CID mass spectra of (A) $[\text{Ni}(\text{NO}_3)_3]^-$ and (B) $[\text{NiO}(\text{NO}_3)_2]^-$ recorded at 40 eV <sub>lab</sub> with 0.50 mTorr of Ar collision gas. ....	57
5.3	Energy-dependent fragmentation spectra of (A) $[\text{Ni}(\text{NO}_3)_3]^-$ and (B) $[\text{NiO}(\text{NO}_3)_2]^-$ . ....	59
5.4	Calculated relative energy differences for the decomposition of $[\text{Ni}(\text{NO}_3)_3]^-$ at the (U)B3LYP/6-311+G(3df) level of theory. All energies include zero-point corrections. Select bond lengths and	

	charges for the metal and unique oxygen atoms are indicated. Atom colors: teal for nickel, blue for nitrogen, and red for oxygen. ....	61
5.5	Potential energy diagram for decomposition of $[\text{NiO}_2(\text{NO}_3)]^-$ . Color description: black and gray dashes = elimination of $\text{O}_2$ ; blue dashes = elimination of $\text{NO}_2^\bullet$ . ....	62
5.6	Hypothetical zero-order orbital interaction diagram illustrating the formation of $[\text{NiO}]^+$ from $\text{Ni}^{2+}$ and $\text{O}^{\bullet-}$ . ....	67
6.1	Representative Q1MS spectrum of cobalt nitrate solution. ....	72
6.2	Representative CID spectra for (A) $[\text{Co}(\text{NO}_3)_3]^-$ , (B) $[\text{CoO}(\text{NO}_3)_2]^-$ , (C) $[\text{CoO}_2(\text{NO}_3)]^-$ , and (D) $[\text{CoO}_3]^-$ at 30 eV <sub>lab</sub> collision energy with 0.50 mTorr Ar collision gas. ....	73
6.3	ERMS spectra for the dissociation of (A) $[\text{Co}(\text{NO}_3)_3]^-$ , (B) $[\text{CoO}(\text{NO}_3)_2]^-$ , (C) $[\text{CoO}_2(\text{NO}_3)]^-$ , and (D) $[\text{CoO}_3]^-$ . ....	74
6.4	Calculated relative energy differences for the decomposition of $[\text{Co}(\text{NO}_3)_3]^-$ at the (U)B3LYP/6-311+G(3df) level of theory. All energies include zero-point corrections. Select bond lengths are indicated. Atom colors: gray for cobalt, blue for nitrogen, and red for oxygen. ....	76
6.5	Potential energy diagram for (A) oxygen atom elimination from $[\text{CoO}_2(\text{NO}_3)]^-$ and (B) $\text{O}_2$ elimination from $[\text{CoO}_3]^-$ . Select bond lengths are indicated. Black lines indicate the lowest elimination route, red lines indicate the intermediate energy pathway, and blue lines indicate the highest energy pathway. ....	77
6.6	Hypothetical molecular orbital diagram for the formation of $[\text{CoO}]^+$ from $\text{Co}^{2+}$ and $\text{O}^{\bullet-}$ . The relative orbital energies suggest cobalt is oxidized upon bond formation with oxygen. ....	79
7.1	Representative Q1MS spectrum for a $\text{PEG}_n$ solution with peaks for $n = 4 - 9$ labeled. ....	92
7.2	Schematic decomposition reactions for single and multiple monomer unit loss from $[\text{H+PEG}_n]^+$ via the formation of cyclic intermediates. Bond cleavage adjacent to the positively charged oxygen atom yields a neutral cyclic ether and a smaller fragment ion. This reaction can repeat to yield multiple smaller fragments. ....	93

7.3	Alternative schematic decomposition reaction for single monomer unit loss from $[\text{H+PEG}_n]^+$ via a 1,2-hydride shift. Bond cleavage adjacent to the positively charged oxygen atom yields neutral acetaldehyde and a smaller fragment ion. ....	94
7.4	Representative CID spectra of $[\text{H+PEG}_n]^+$ , $n = 4 - 9$ , at a collision energy of 20 eV <sub>lab</sub> . The fragment ions, labeled as $b_m$ , are located at regularly space intervals according to the equation $m/z = m(44) + 1$ . ....	96
7.5	Representative ERMS studies of the fragments $b_1$ to $b_4$ from dissociation of $[\text{H+PEG}_n]^+$ , $n = 4 - 9$ . The intensities reflect the relative intensities of each ion, and the collision energy scale is plotted in the center-of-mass frame. ....	98
7.6	Representative CID spectra of the fragment ions, $b_2 - b_5$ at 10 eV <sub>lab</sub> . The ions were generated by in-source dissociation of $[\text{H+PEG}_n]^+$ . The precursor ions A) $b_2$ , B) $b_3$ , C) $b_4$ , and D) $b_5$ and their fragment ions are labeled in each spectrum. ....	101
8.1	Negative-ion CID spectra of deprotonated PEG, $[\text{PEG}_n - \text{H}]^-$ ( $n = 1 - 8$ ). All spectra were recorded at 30 eV collision energy, lab-frame, with argon collision gas at a pressure of 0.20 mTorr. ....	110
8.2	Schematic decomposition reaction for multiple monomer unit loss from $[\text{PEG}_n - \text{H}]^-$ via the formation of a cyclic intermediate. Cleavage at the external C-O bond of the cyclic moiety yields a neutral cyclic ether and a smaller anion fragment. This reaction can repeat to yield ever smaller fragments. ....	113
8.3	Negative-ion CID of $[\text{PEG}_4 - \text{H}]^-$ at 30 eV <sub>lab</sub> with 1.00 mTorr argon collision gas. ....	114
8.4	Schematic decomposition reaction for loss of H <sub>2</sub> from $[\text{PEG}_n - \text{H}]^-$ for $n = 1, 2$ . ....	115
8.5	Schematic decomposition reaction for loss of H <sub>2</sub> O from $[\text{PEG}_1 - \text{H}]^-$ . ...	115
9.1	Three representative molecular orbital diagrams for metal oxide bond formation in the three redox regimes of the transition metals studied. Panel A shows the hypothetical diagram for $[\text{CoO}]^+$ , panel B shows the hypothetical diagram for $[\text{NiO}]^+$ , and panel C shows the hypothetical diagram for $[\text{ZnO}]^+$ . ....	120

## CHAPTER 1

### INTRODUCTION

The research discussed in this dissertation deals primarily with dissociation studies of metal nitrate anion complexes. The studies were performed to gain insight into the metal-oxygen bond in the metal oxide product complexes. Trends in the decomposition of complexes containing various transition and main group metals were discovered and correlate with properties specific to each metal. Many of the findings have been published,<sup>1-5</sup> whereas others are prepared for submission. Research was performed and published on small polymer chains to initially determine the capabilities of and standard procedures for using the mass spectrometer.<sup>6,7</sup>

#### *1.1 Current Issues in Metal Oxide Studies*

Modern industrial chemistry relies on heterogeneous catalysts, often composed of metals or metal oxides, to increase yields and reduce waste and energy costs. Surprisingly, the most economical approach to identify catalysts for industrial use involves combinatorial or trial-and-error searches. These methods can be used to select viable catalysts, but they offer little insight as to why a particular catalyst works at the molecular level. The development of new catalysts tailored for applications with increased activity, specificity, turnover, minimal waste generation, and low cost, requires a fundamental understanding of catalyst active site properties.

Experiments that provide fundamental atomic-level information on active site structures promise to usher in a new era of advanced high-performance catalysis. A variety of experimental methods are needed to realize these goals. Gas-phase ion chemistry allows direct

investigation of model, size-selected metal oxide complexes under carefully controlled conditions.<sup>8-12</sup> These studies make it possible to observe changes that depend on stoichiometry, oxidation state, spin state, and size. For example, research on nanoclusters has repeatedly demonstrated that addition or removal of a single atom can drastically alter reactivity.<sup>8,10,12-17</sup> We are interested in measuring properties of metal oxides composed of a few atoms with the goal of better understanding metal-oxygen bonding. Experiments on small model systems provide a conceptual foundation that improves our understanding of bonding, electronic structure, and reactivity in more complex and larger clusters.

## *1.2 Formation of Metal Oxides*

Mass spectrometry provides a readily accessible method to generate and investigate small metal oxide clusters. Previous studies have shown that electrospray ionization, ESI, can be used to transfer solution-phase metal nitrate ions into the gas phase. These gas-phase metal complexes can be fragmented via collision-induced dissociation, CID, to yield metal oxide product complexes. This approach has been used to study numerous metal nitrate systems solely to determine how the complexes dissociate,<sup>18,19</sup> but the more fundamental search into the redox characteristics of the product metal oxides was absent in the literature. Our group performed dissociation studies for three different metal nitrate systems, using computational methods to correlate calculated oxidation states to the observed dissociation from experimentally obtained mass spectra. The calculations provide theoretical values for atomic charge, metal electron configuration, valence orbital occupancies, and values for the excess electron spin on each atom.

### 1.3 Previous Studies

The Goebbert group performed mass spectrometry studies on copper nitrate anions to yield copper oxide complexes.<sup>1</sup> The copper system revealed an important distinction between the dissociation patterns of complexes with metals in different oxidation states. The  $[\text{Cu}(\text{NO}_3)_3]^-$  complex contains a  $\text{Cu}^{2+}$  cation with a  $3d^9$  electron configuration. The copper cation has a low energy vacancy in the  $3d$  subshell that is readily filled upon loss of  $\text{NO}_3^\bullet$ . The product complex,  $[\text{Cu}(\text{NO}_3)_2]^-$ , contains a  $\text{Cu}^+$  cation with a  $3d^{10}$  electron configuration. This complex undergoes a distinct set of dissociation reactions due to the filled  $3d$  subshell and high energy, vacant  $4s$  orbital of  $\text{Cu}^+$ . Sequential losses of  $\text{NO}_2^\bullet$  from  $[\text{Cu}(\text{NO}_3)_2]^-$  are the primary dissociation route since reduction of  $\text{Cu}^+$  is unfavorable. Elimination of  $\text{NO}_2^\bullet$  occurs via abstraction of  $\text{O}^{\bullet-}$  from a nitrate ligand, yielding a metal-oxygen bond. Theoretical calculations show copper maintains the  $3d^{10}$  electron configuration upon sequential metal-oxygen bond formation. A hypothetical molecular orbital, MO, diagram is shown in Figure 1.1A for the formation of the Cu-O bond of the neutral CuO core in  $[\text{CuO}(\text{NO}_3)]^-$ . The  $3d$  subshell of copper is too low in energy to engage in orbital mixing, so the oxygen ligand retains its  $-1$  oxidation state. The copper system shows a low degree of decomposition, but an important finding became apparent. The decomposition patterns for  $\text{Cu}^{2+}$  and  $\text{Cu}^+$  correspond directly to the oxidation states of the metal.

A second study was performed for the chromium system.<sup>2</sup> The nitrate anion complexes containing this early transition metal show dissociation very different from that observed for the copper complexes. Chromium nitrate complexes dissociate primarily via  $\text{O}^{\bullet-}$  abstraction upon  $\text{NO}_2^\bullet$  loss. The metal is oxidized upon each  $\text{O}^{\bullet-}$  abstraction, yielding chromium in an increased oxidation state and an  $\text{O}^{2-}$  ligand. The chromium system displays these dissociation characteristics due to the high energy  $3d$  subshell of the early transition metal. The hypothetical

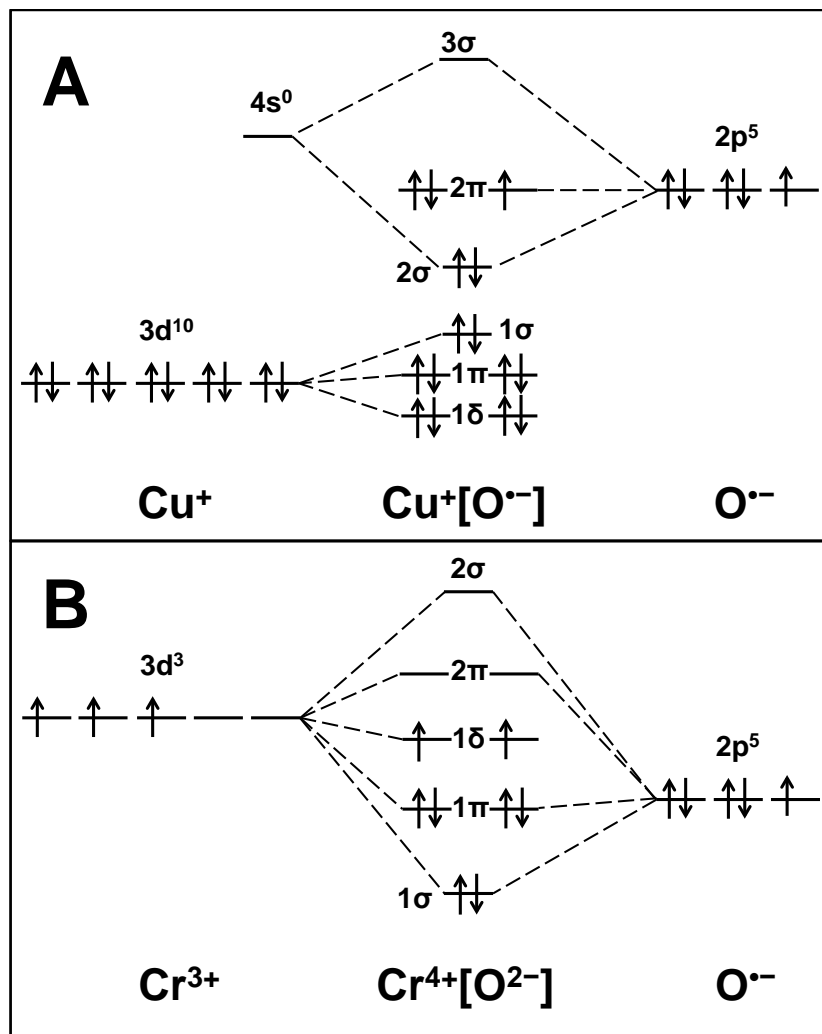


Figure 1.1 Two representative molecular orbital diagrams for metal oxide bond formation. Panel A shows the hypothetical diagram for CuO. Panel B shows the hypothetical diagram for  $[\text{CrO}]^{2+}$ .

MO diagram, Figure 1.1B, shows the formation of the Cr-O bond involves electron transfer from a high energy Cr(3d) orbital to a lower energy O(2p) orbital. The chromium oxide complexes with no further nitrate ligands, called bare metal oxides, undergo competitive losses of atomic and molecular oxygen. These losses necessarily result in reduction of the metal. The high oxidation states of +6 and +5 for chromium in the respective bare metal oxides,  $[\text{CrO}_4]^-$  and  $[\text{CrO}_3]^-$ , facilitate metal reduction upon loss of O atom and  $\text{O}_2$ .

Another study on aluminum nitrate complexes was carried out to determine the contribution of main group metals to the observed dissociation characteristics of metal anion complexes.<sup>3</sup> Aluminum contains no *d*-orbitals and has a very high charge state of +3, relative to the common charge states for most transition metals. The nitrate anion complexes show dissociation via  $\text{NO}_2^\bullet$  and  $\text{NO}_3^\bullet$  loss. There are instances of  $\text{O}_2$  loss via low energy nitrate isomerization. This isomerization step involves abstraction of O atom from a nitrate ligand. A superoxide ligand is formed that is eliminated as neutral  $\text{O}_2$  upon electron transfer. The +3 oxidation state of aluminum is maintained for the majority of product complexes, and the dissociation reactions for each complex are driven primarily by the presence of any radical oxygen ligands. The *4s* orbital of aluminum is too high in energy to engage in redox chemistry, whereas the O(2p) orbitals contain low energy vacancies that are reactive.

#### *1.4 Direction of Dissertation Research*

This dissertation contains an expanded collection of metals being studied by the Goebbert group. These studies were performed to determine the full scope of the relationship between the occupancy of the metal valence orbitals and the observed dissociation pathways. Metals with the most similarities to those previously studied were chosen for further studies. Gallium is used to

determine more properties of the main group metals. Zinc, nickel,<sup>4</sup> and cobalt were chosen to investigate transition metals more thoroughly.

Chapter 3 contains the results of research into gallium nitrate complexes. The gallium studies are a logical follow-up to the aluminum studies, with Ga<sup>3+</sup> differing only in ionic radius and in having a vacant *4s* valence. The larger size of gallium may favor specific dissociation reactions, whereas the relative energy of the *4s* valence may influence dissociation.

Chapter 4 discusses the studies on zinc nitrate complexes. Zinc was chosen since it has an identical electron configuration to that of two previously studied cations, Cu<sup>+</sup> and Ga<sup>3+</sup>. The zinc cation differs by its +2 oxidation state, making this study important for determining the effect of oxidation state on dissociation, with no need to regard identical electron configurations.

Chapters 5 and 6 contain the results of research into the nitrate complexes of two transition metals located between chromium and copper in the *3d* series. The *3d*<sup>8</sup> configuration for Ni<sup>2+</sup> makes it an interesting candidate for determining whether oxidation state or electron configuration has a larger influence on observed dissociation reactions. The nickel system can be compared to other systems with a +2 oxidation state, such as Cu<sup>2+</sup> and Zn<sup>2+</sup>, while being contrasted to those same systems due to their different electron configurations.

Chapter 6 discusses the studies on cobalt nitrate complexes. The *3d*<sup>7</sup> electron configuration of Co<sup>2+</sup> can expound on the importance of orbital occupancies and valence energy levels on the dissociation of metal nitrate anions. It is expected that somewhere in the transition metal series, a break must occur in the primary mode of dissociation from metal reduction upon NO<sub>3</sub><sup>•</sup> loss, as observed for Cu<sup>2+</sup>, to metal oxidation upon NO<sub>2</sub><sup>•</sup> loss, as observed for Cr<sup>3+</sup>. The ultimate goals of this dissertation research are 1) to determine the oxidation states of the metals in the complexes of interest, 2) to correlate the influence of oxidation states, orbital occupancies,

and orbital energy levels to dissociation properties, and 3) to determine an overall trend of dissociation within the transition and main group metals as it relates to placement in the periodic table for future reference.

### 1.5 References

- [1] Pruitt, C.J.M.; Goebbert, D.J. Experimental and Theoretical Study of the Decomposition of Copper Nitrate Cluster Anions. *J. Phys. Chem. A*. **2015**, *119* (20), 4755-4762.
- [2] Albury, R.M.; Pruitt, C.J.M.; Hester, T.H.; Goebbert, D.J. Fragmentation of  $\text{Cr}(\text{NO}_3)_4^-$ : Metal Oxidation upon  $\text{O}^-$  Abstraction. *J. Phys. Chem. A*. **2015**, *119* (47), 11471-11478.
- [3] Lightcap, J.; Hester, T.H.; Kamena, K.; Albury, R.M.; Pruitt, C.J.M.; Goebbert, D.J. Gas-Phase Fragmentation of Aluminum Oxide Nitrate Anions Driven by Reactive Oxygen Radical Ligands. *J. Phys. Chem. A*. **2016**, *120* (9), 1501-1507.
- [4] Hester, T.H.; Albury, R.M.; Pruitt, C.J.M.; Goebbert, D.J. Fragmentation of  $[\text{Ni}(\text{NO}_3)_3]^-$ : A Study of Nickel-Oxygen Bonding and Oxidation States in Nickel Oxide Fragments. *Inorg. Chem.* **2016**, *55* (13), 6634-6642.
- [5] Hester, T.H.; Goebbert, D.J. Experimental and Theoretical Study of the Decomposition of  $[\text{Zn}(\text{NO}_3)_3]^-$ . *Chem. Phys. Lett.* **2016**, In Press.
- [6] Hester, T.H.; McCraney, K.K.; Castillo, D.E.; Goebbert, D.J. The Sequential Dissociation of Protonated Polyethylene Glycols. *J. Mass Spectrom.* **2013**, *48* (4), 459-464.
- [7] Hester, T.H.; Castillo, D.E.; Goebbert, D.J. Fragmentation of Deprotonated Polyethylene Glycols,  $[\text{PEG} - \text{H}]^-$ . *R. Comm. Mass Spectrom.* **2013**, *27* (14), 1643-1648.
- [8] Johnson, G.E.; Reilly, N.M.; Castleman Jr, A.W. Effect of Charge State and Stoichiometry on the Structure and Reactivity of Nickel Oxide Clusters with CO. *Int. J. Mass Spectrom.* **2009**, *280*, 93-100.
- [9] Vann, W.D.; Bell, R.C.; Castleman, A.W. Gas-Phase Reactions of Nickel and Nickel Oxide Clusters with Nitrogen Oxides. 3. Reactions of Cations with Nitric Oxide. *J. Phys. Chem. A*. **1999**, *103* (50), 10846-10850.
- [10] Vann, W.D.; Castleman, A.W. Gas-Phase Reactions of Nickel and Nickel Oxide Clusters with Nitrogen Dioxide. 4. Continued Kinetic and Mechanistic Investigation of Nickel Cluster Reactions with  $\text{NO}_x$  Gases. *J. Phys. Chem. A*. **1999**, *103* (7), 847-857.
- [11] Vann, W.D.; Wagner, R.L.; Castleman, A.W. Gas-Phase Reactions of Nickel Oxide Clusters with Nitric Oxide. 1. Formation of Nitrogen Dioxide on Nickel Oxide Cluster Anions. *J. Phys. Chem. A*. **1998**, *102* (10), 1708-1718.

- [12] Vann, W.D.; Wagner, R.L.; Castleman, A.W. Gas-Phase Reactions of Nickel and Nickel-Rich Oxide Cluster Anions with Nitric Oxide. 2. The Addition of Nitric Oxide, Oxidation of Nickel Clusters, and the Formation of Nitrogen Oxide Anions. *J. Phys. Chem. A*. **1998**, *102* (45), 8804-8811.
- [13] Sakuma, K.; Miyajima, K.; Mafuné, F. Oxidation of CO by Nickel Oxide Clusters Revealed by Post Heating. *J. Phys. Chem. A*. **2013**, *117* (16), 3260-3265.
- [14] Felton, J.A.; Ray, M.; Waller, S.E.; Kafader, J.O.; Jarrold, C.C.  $Ce_xO_y^-$  ( $x = 2-3$ ) +  $D_2O$  Reactions: Stoichiometric Cluster Formation from Deuterioxide Decomposition and Anti-Arrhenius Behavior. *J. Phys. Chem. A*. **2014**, *118* (43), 9960-9969.
- [15] Ray, M.; Waller, S.E.; Saha, A.; Raghavachari, K.; Jarrold, C.C. Comparative Study of Water Reactivity with  $Mo_2O_y^-$  and  $W_2O_y^-$  Clusters: A Combined Experimental and Theoretical Investigation. *J. Chem. Phys.* **2014**, *141* (10), 104310.
- [16] Morita, K.; Sakuma, K.; Miyajima, K.; Mafuné, F. Thermally and Chemically Stable Mixed Valence Copper Oxide Cluster Ions Revealed by Post Heating. *J. Phys. Chem. A*. **2013**, *117* (40), 10145-10150.
- [17] Vardhan, D.; Liyanage, R.; Armentrout, P.B. Guided Ion Beam Studies of the Reactions of  $Ni_n^+$  ( $n=2-18$ ) with  $O_2$ : Nickel Cluster Oxide and Dioxide Bond Energies. *J. Chem. Phys.* **2003**, *119* (8), 4166-4178.
- [18] Frański, R.; Sobieszczuk, K.; Gierczyk, B. Mass Spectrometric Decomposition of  $[M^{n+}(NO_3^-)_{n+1}]^-$  Anions Originating from Metal Nitrates  $M(NO_3)_n$ . *Int. J. Mass Spectrom.* **2014**, *369*, 98-104.
- [19] Li, F.; Byers, M.A.; Houk, R.S. Tandem Mass Spectrometry of Metal Nitrate Negative Ions Produced by Electrospray Ionization. *J. Am. Soc. Mass Spectrom.* **2003**, *14* (6), 671-679.

## CHAPTER 2

### METHODS

Research has been performed previously on metal oxides and involved the generation of gas-phase metal nitrate complexes by specific ionization methods. These ions could be dissociated to form metal oxide products using mass spectrometric techniques.<sup>1-7</sup> The metal oxide cores of these product complexes were not previously analyzed using the common computational methods described in this chapter. Published studies on polyethylene glycol, PEG, systems also contain the following methods.<sup>8,9</sup>

#### *2.1 Experimental Methods*

Mass spectrometers are designed to manipulate the trajectories of ions that are generated by an ionization source. The ions can be guided using ion optics and optionally subjected to dissociation and other chemical probing methods. Ions, fragments, and adducts are detected to produce a mass spectrum from data acquired.

##### 2.1.1 Instrumentation

Figure 2.1 shows an instrumental diagram for the Finnigan MAT tandem mass spectrometer, model TSQ-7000 (Finnigan MAT, San Jose, CA). The source region contains the electrospray ionization, ESI, source at a pressure around 760 Torr. This ionization source can be used to generate either anions and cations, depending on the polarity of the 4 kV needle voltage. Two standard compositions were used for the sample solutions in this dissertation research. The

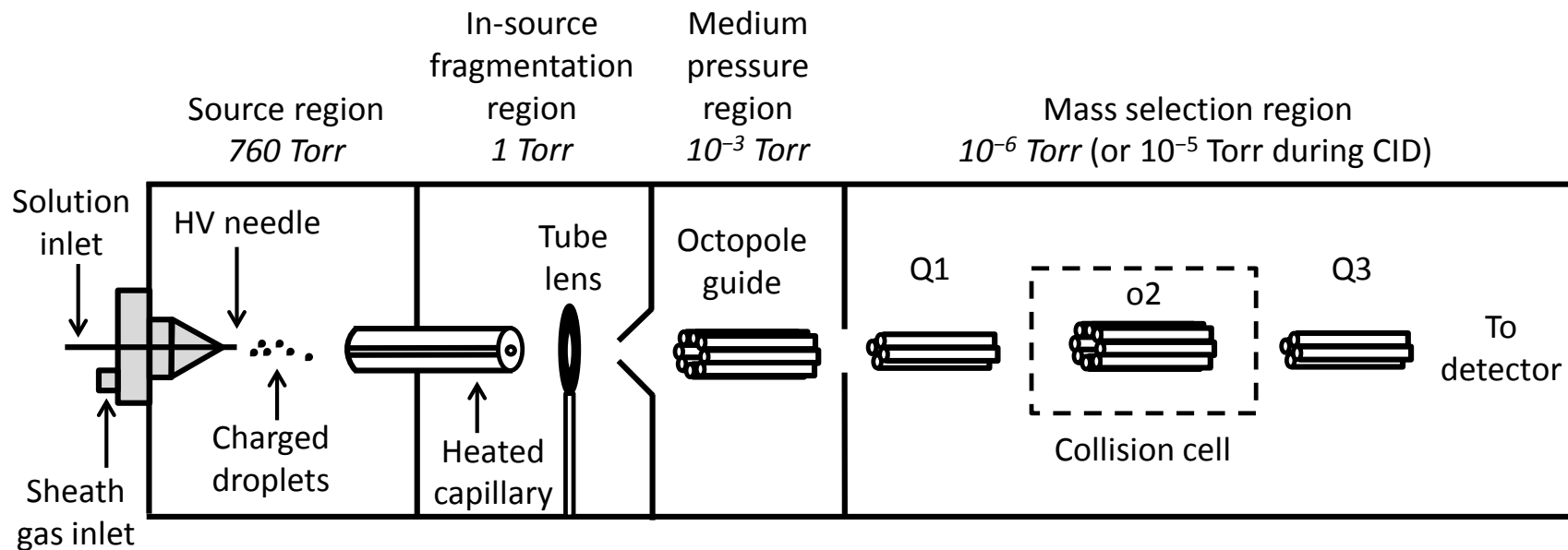


Figure 2.1 Representative schematic for the tandem mass spectrometer, TSQ-7000. Each region is labeled with relative pressures given in Torr.

metal nitrate studies were performed using a concentration of 1 mM metal salt in a solvent mixture of HPLC-grade acetonitrile and methanol in a 1:1 (volume/volume) ratio. The polymer studies were performed using a sample concentration of 1 mM in a solvent mixture of water and methanol in a 1:1 (volume/volume) ratio. The ionic solutions were infused into the ESI source by a syringe pump at a constant rate of 4  $\mu\text{L}/\text{min}$ . The optimal solution flow rate is paired with an optimized sheath gas pressure, typically 60 psi for negative-mode studies and 40 psi for positive-mode studies, so the solvated ions of interest are efficiently emitted from the ESI needle tip. The fundamentals of ESI and the operation of ESI sources have been detailed extensively in the literature.<sup>10-13</sup>

A heated capillary facilitates the removal of solvent from the small charged droplets generated during ESI. The bare ions enter another region, called the in-source fragmentation region, maintained at a pressure around 1 mTorr. The ions are directed through a tube lens, with an applied voltage that can optionally induce in-source fragmentation. A skimmer collimates the ion beam before entrance into a medium pressure region containing an octopole ion guide and maintained at a pressure at  $10^{-3}$  Torr.

The ions enter the mass selection region, maintained at a pressure at  $10^{-5}$  Torr. Focusing lenses guide ions through the first quadrupole, Q1, mass selector. This mass selector scans a specified range of ions by their mass-to-charge,  $m/z$ , ratio. The ions with stable paths under the applied conditions, i.e. a set DC voltage superimposed with a radio-frequency AC voltage is applied to the four poles of Q1, are transmitted to the second mass selector. Ions with unstable paths in Q1 are emitted and become neutralized upon impact with the quadrupole rods or inner walls of the mass spectrometer. An octopole, o2, serves as the second mass selector rather than a quadrupole for a more uniform electric field. This uniform field benefits ion transmission during

optional dissociation studies. A metal shroud that acts as a collision cell surrounds the octopole. Dissociation studies can be performed within this collision cell, using the relative voltage of the octopole to fragment ions in an energy-dependent manner. The octopole can be used in this fashion for various ion-neutral interaction studies, or it can be used simply as an ion guide to the third mass selector, Q3. This final quadrupole scans a  $m/z$  range and transmits that selection of ions to the detector.

### 2.1.2 Operational Modes

Table 2.1 lists the modes for mass selector operation commonly used on our tandem mass spectrometer. The Q1-mass spectrometry, Q1MS, mode involves scanning the first quadrupole over a specified  $m/z$  range. The other mass selectors act as ion guides that transmit the Q1-selected ions to the detector. A mass spectrum, as shown in Figure 2.2A, is generated for all ions within the  $m/z$  range scanned by Q1. At least three Q1MS spectra are collected on separate days to ensure reproducibility. A representative spectrum is provided for each system.

Table 2.1 Common operational modes for the tandem mass spectrometer, TSQ-7000. The functions listed for each mass selector determines whether a Q1MS spectrum, a CID spectrum, or an ERMS spectrum is produced.

	<b>Q1</b>	<b>o2</b>	<b>Q3</b>
<b>Q1MS</b>	Scan $m/z$ range	Ion guide	Ion guide
<b>CID</b>	Set precursor $m/z$	Set voltage	Scan $m/z$ range
<b>ERMS</b>	Set precursor $m/z$	Scan voltage	Set fragment $m/z$

The collision-induced dissociation, CID, mode involves scanning a  $m/z$  range of ESI-generated ions in Q1 and transmitting those ions to the octopole. An inert target gas, argon, fills the collision cell at a set pressure of 0.50-1.00 mTorr. The transmitted precursor ions are accelerated by the applied voltage on the octopole into the collision cell and undergo collisions

with the target gas. An amount of ion kinetic energy is converted into ion internal energy upon impact with the target gas as determined by Equation 2.1, showing conversion from the lab frame collision energy to the center-of-mass frame. The internal energy redistributes into the vibrational modes and, over a few vibrational periods, re-accumulates into a single bond.

Dissociation of this bond results in the generation of a product ion and a neutral fragment. The product ions are transmitted through Q3, an ion guide in CID mode, and impact the detector. A CID spectrum, as shown in Figure 2.2B, contains peaks for the precursor and fragment ions. At least three dissociation spectra are collected on separate days to ensure reproducibility. A representative spectrum is provided for each system.

$$E_{\text{c.m.}} = E_{\text{lab}} \times \frac{m_{\text{target}}}{m_{\text{target}} + m_{\text{ion}}} \quad \text{Equation 2.1}$$

In-source fragmentation is a method of generating authentic product ions in the source region. A high voltage can be applied to the tube lens to induce fragmentation of ESI-generated ions. The fragment ions are transmitted through Q1, can be fragmented in the collision cell, and can be transmitted through Q3 to be detected.

The final operational mode in Table 2.1 is energy-resolved mass spectrometry, ERMS. This mode involves scanning Q1 over a  $m/z$  range that is 1  $m/z$  unit wide. The first quadrupole is effectively set to transmit only ions with that specified  $m/z$  ratio. The transmitted precursor ions are subjected to CID over a given energy range, determined by the scanned voltage on the octopole. A homemade software program was created to automate the setting of parameters for ERMS data acquisition. The program code is provided in the Appendix. The precursor ions are accelerated over the range of collision energies and collide with the Ar target gas. The pressure inside the collision cell is held at low pressure, 0.15-0.20 mT, to minimize multiple collisions for

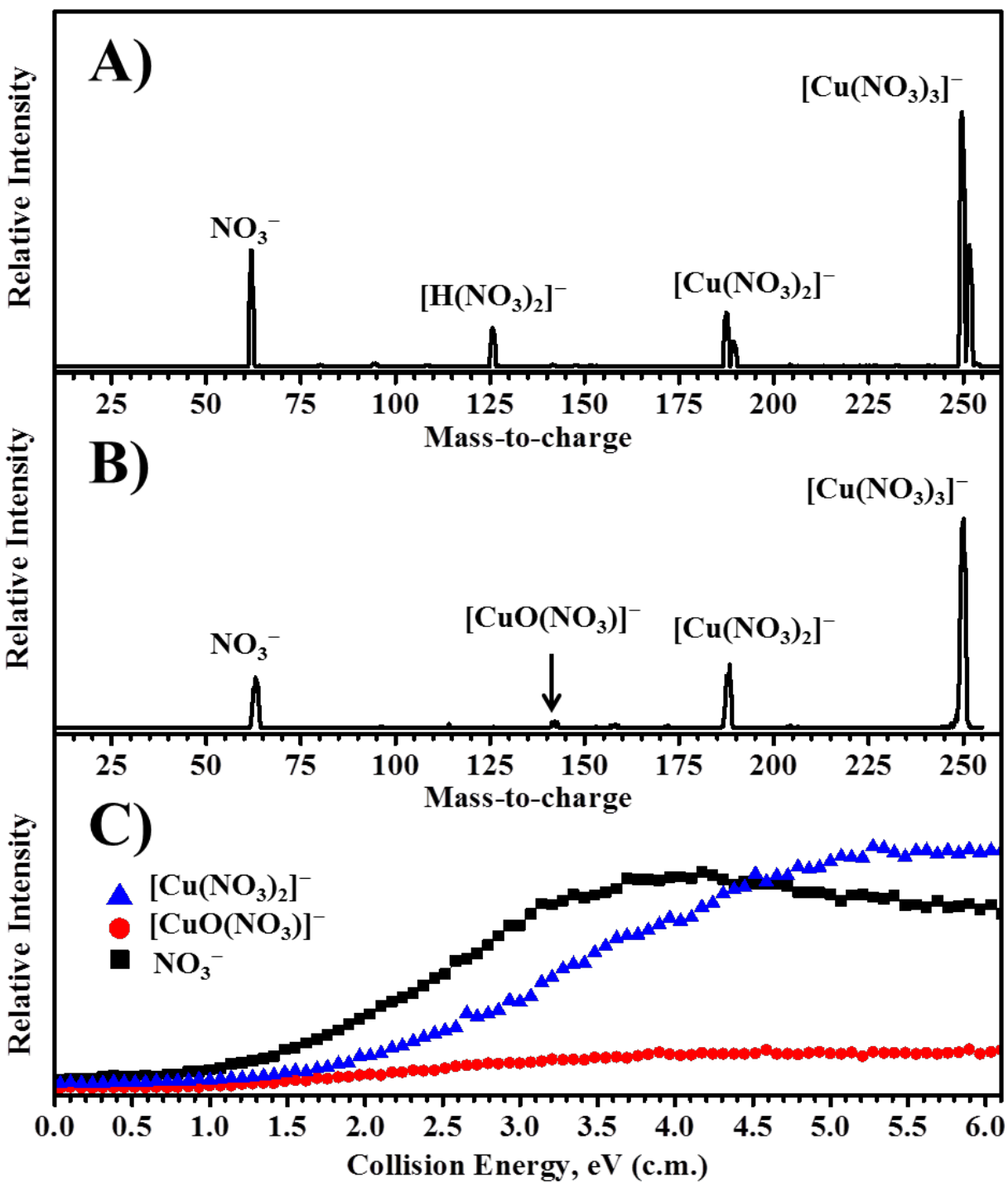


Figure 2.2 Representative spectra obtained for the various operational modes on the TSQ-7000. Each panel represents A) the Q1MS spectrum for a copper nitrate sample, B) the CID spectrum of  $[\text{Cu}(\text{NO}_3)_3]^-$ , and C) the ERMS curves for  $[\text{Cu}(\text{NO}_3)_3]^-$  dissociation.

more accurate energy deposition upon collision. The final quadrupole scans a 1  $m/z$  unit range for a given product ion and transmits the range to the detector to determine the individual intensity of that ion at each collision energy. All product ions are individually monitored by ERMS and the intensity curves for all product ions from a given precursor are plotted together on an ERMS spectrum, as shown in Figure 2.2C. All ERMS curves for a specific precursor ion are collected each day on at least three separate days to ensure reproducibility. The curves for each fragment ion represent an average of at least three curves obtained during that day's acquisition.

## 2.2 *Theoretical Methods*

Theoretical methods have been developed as a tool for readily determining intrinsic properties of chemical species that are not easily found through experiment. The fundamentals of this approach rely on the description of atomic and chemical species through the wave picture of matter. Electrons in atoms and molecules can be described using wavefunctions. Theoretical chemists have developed models of varying degrees of sophistication that can be used by computational chemists for determination of properties, such as structure, vibrational modes and energies, and reaction energies.

### 2.2.1 Outline of Computational Chemistry

The theoretical calculations performed by our group rely on well-established methods implemented in commercially available software. Because quantum mechanics is the foundation for computational chemistry, we provide a brief sketch of how these calculations are carried out. This section is by no means complete or comprehensive, and the interested reader can find a more in-depth description of computational chemistry in standard references.<sup>14-17</sup>

Wavefunctions, in principle, contain all of the properties for a molecule. Mathematical operators extract a desired value that corresponds to a certain property such as position, momentum, or energy. For instance, Equation 2.2 shows a molecular wavefunction depends on nuclear,  $\mathbf{R}$ , and electron coordinates,  $\mathbf{r}$ . The operator,  $\hat{H}$  or Hamiltonian, operates on the wavefunction to yield the total energy,  $E$ , corresponding to that specific wavefunction.

$$\hat{H}\Psi(\mathbf{R},\mathbf{r}) = E\Psi(\mathbf{R},\mathbf{r}) \quad \text{Equation 2.2}$$

Solution of Equation 2.2 is difficult for all but the simplest molecules, and several approximations are typically implemented to reduce the problem into a solvable set of equations.

The first approximation is the Born-Oppenheimer approximation which separates nuclear and electron coordinates. This is possible due to the nearly instantaneous response of electron motion to nuclear motion. The wavefunction,  $\Psi(\mathbf{R},\mathbf{r})$ , in Equation 2.2 can be factored as  $\psi(\mathbf{R})\Phi(\mathbf{r})$ , shown in Equation 2.3, and the nuclear repulsion energy is constant for fixed coordinates.

$$\Psi(\mathbf{R},\mathbf{r}) = \psi(\mathbf{R})\Phi(\mathbf{r}) \quad \text{Equation 2.3}$$

The Born-Oppenheimer approximation thus requires a solution of the Schrödinger equation for the just the electronic part of the wavefunction,  $\Phi(\mathbf{r})$ , with a parametric dependence on nuclear coordinates.

The many-electron wavefunction,  $\Phi(\mathbf{r})$ , contains all coordinates for a molecule system with  $N_e$  total electrons. It can be written as a product of single-electron functions,  $\phi_a(i)$ , as shown in Equation 2.4. The energy calculated for a finite number of orbitals will be greater than or equal to the exact energy of the system as required by the variational principle. Larger basis sets improve the accuracy of the calculation but increase computational time.

$$\Phi(1, 2, \dots, N_e) = \phi(1)\phi(2)\dots\phi(N_e) \quad \text{Equation 2.4}$$

The product is incomplete however, because electrons are indistinguishable and the total wavefunction must be antisymmetric with respect to exchange of electrons. These properties can be incorporated by writing the total wavefunction as a Slater determinant.

$$\hat{H} = -\frac{\hbar^2}{2m_e} \sum_i^{\text{electrons}} \nabla_i^2 - \frac{e^2}{4\pi\epsilon_0} \sum_i^{\text{electrons}} \sum_A^{\text{nuclei}} \frac{Z_A}{r_{iA}} + \frac{e^2}{4\pi\epsilon_0} \sum_j^{\text{electrons}} \sum_{i<j}^{\text{electrons}} \frac{1}{r_{ij}} \quad \text{Equation 2.5}$$

With these approximations in place, we solve the *electronic Schrödinger Equation*, given by Equation 2.5, where the first term is the electron kinetic energy, the second term is the electron-nuclear Coulombic energy, and the final term is the electron-electron Coulombic energy. The nuclear-nuclear Coulombic energy is added at the end of the calculation. In the Hartree-Fock, HF, approximation, this problem is solved by the self-consistent-field, SCF, procedure. The HF method yields a set of differential equations. The energy for a single electron is minimized keeping all other electrons fixed. The process is repeated for all electrons in the system. A new set of functions for each electron is generated, and the new solutions are inserted into the equations by an iterative procedure. An optimized set of orbitals is obtained once the energy difference from one iteration to the next is under a given threshold. The major limitation of the HF treatment is the treatment of electron-electron interactions in an average way. Thus, HF energies are too large because instantaneous electron-electron interactions have not been incorporated into the model.

### 2.2.2 Basis Sets

Each solution to the electron functions,  $\Phi(\mathbf{r})$  in Equation 2.4, defines a molecular orbital, MO. The MOs have electron density over many atoms and can be thought of as being formed through hybridization of atomic orbitals, AOs. The contributions of AOs toward the formation

of each MO can be approximated by assuming the MOs are constructed as a linear combination of AOs, i.e. using the LCAO approximation. Gaussian-type orbitals can be used to mathematically describe AOs. Each of these Gaussian-type orbitals is called a primitive Gaussian function. The linear combination of primitive Gaussian functions yields a contracted function that converges toward an accurate description of the AOs with each addition of a primitive Gaussian. The linear combination of Gaussian-type orbitals is handled through integration, which is very fast for Gaussian functions because of their exponential form.<sup>14</sup>

A Pople basis set, such as 6-311G++(3df), can be used to reliably treat orbitals for the atoms within a molecule.<sup>14,17</sup> The number before the hyphen refers to the use of six primitive Gaussian functions to describe the core electrons for atoms. The numbers after the hyphen refer to the use of a split valence description, in this case a triply-split valence. The first number corresponds to a contracted valence orbital comprised of three primitive Gaussian functions. The next number corresponds to an un-contracted valence orbital made from a single primitive function. The last number corresponds to the number of primitive functions used to describe hydrogen atoms within the molecule and is superfluous in calculations of molecules containing no hydrogen atoms. These sets of Gaussian groups describe the valence in a way that allows the valence orbitals to contract and expand. This treatment, using a split valence description, allows for a change in orbital size to obtain the correct MO environment.

The “+” symbol corresponds to the addition of diffuse functions to non-hydrogen and hydrogen atoms respectively.<sup>14,17</sup> These diffuse functions are a set of functions of the same type already present in the valence that are added to the basis set to allow the electron density to expand. The diffuse functions are used to accurately handle multiple adjacent lone pairs, especially in anions.

Polarization functions are given in parentheses, such as (3df) for a 3d valence atom. The addition of polarization functions allows the valence orbitals to distort to form bonds.<sup>14,17</sup> The orbital energies are optimized to their correct bonding and non-bonding geometries, in this case by adding a single set of *f*-type functions to the basis sets of all non-hydrogen atoms in the molecule. The function effectively distorts the 3d orbital into a larger three-dimensional space with f-orbital character. The larger parameter-space allows the electrons within the orbital to explore more states to reach the lowest energy.

### 2.2.3 Post Hartree-Fock Methods

Hartree-Fock theory is useful for many calculations, but the inherent neglect of electron correlation leads to errors. A number of post HF methods have been developed, including configuration interaction, CI, many-body perturbation theory, and density functional theory, DFT. Of these methods, DFT is popular due to its efficiency.<sup>14,17,18</sup> Theoretical studies in this dissertation rely on DFT methods. Equation 2.6 shows the relationship between the electron density, which depends upon spatial coordinates, and an exact electronic energy,  $E_{\text{elec}}$ , determined using the energy operator,  $\hat{E}$ . Kohn and Sham devised a functional that solves for the orbitals in the molecular system that minimizes the total electronic energy. The Kohn-Sham procedure uses a similar process to that of the HF method, producing Kohn-Sham orbitals that are analogous to HF MOs. Calculations using the DFT level of theory improve upon those obtained from HF and other SCF methods since DFT has the advantage of implicitly treating and including electron correlation in the obtained electronic energy.

$$\hat{E} \rho(r) = E_{\text{elec}} \quad \text{Equation 2.6}$$

The most commonly used functional is the B3LYP hybrid functional. Electron correlation is treated separately from electron exchange to improve theoretical results. The acronym refers to the creators of the embedded functionals: Becke for the treatment electron exchange and Lee, Yang, and Parr for the treatment of electron correlation. Three correction variables are used to modify this hybrid functional to fit experimental data.

#### 2.2.4 Molecular Properties

Reasonable geometries can be obtained from most levels of theory. Vibrational frequencies can be determined using the optimized molecular geometry from an HF or DFT calculation. A collection of energy gradients with respect to the movement of multiple atoms is used to generate a set of second derivatives, called a Hessian matrix, of the “movement” energy. A local minimum is established, and operations on the Hessian matrix generate the vibrational frequencies of the molecule and, most importantly, the zero-point vibrational energy. Theory can also identify transition state geometries, using the “quadratic synchronous transit” or QST approach. Transition states have a single imaginary frequency corresponding to motion along the reaction coordinate.

The total electron density of the molecule can be considered as a collection of MOs that are filled by electrons. A Mulliken population analysis can be performed that very simply distributes the electrons of a given molecule into the AOs that are centered on specific atoms. A more-involved natural population analysis, NPA, can be performed that generates a new set of orthonormal AOs that are maximally occupied, in an effort to localize orbitals to given atoms. The NPA method negates a common problem for Mulliken population analyses, in which electron density that is diffuse over multiple atoms results in the misplacement of electrons.

### 2.2.5 Computational Chemistry

Computational chemistry can be used as a low-cost tool to probe the structures, properties, and reactivities of chemical systems without performing time-intensive experiments for the same results. This section lists the methods discussed in this dissertation.

Molecular structures are optimized using the HF level of theory. The lowest energy HF structures are optimized by DFT using the B3LYP functional with various basis sets, such as 6-311G++(d,p) for the PEG studies and 6-311G++(df) or 6-311G++(3df) for the metal nitrate studies. A natural population analysis can be carried out by placing electrons in localized orbitals to get effective atomic charge and orbital occupancy values. The occupied orbital density of atoms also yields values for excess electron spin on each atom. Transition states are saddle-points along the potential energy surface and can be determined by evaluating vibrational frequencies, specifically a negative frequency corresponding to translational movement along the reaction coordinate. Reaction energies are reported as HF electronic energies with a zero-point energy correction for the fundamental vibrational energies within the molecule.

### 2.3 References

- [1] Frański, R.; Sobieszczuk, K.; Gierczyk, B. Mass Spectrometric Decomposition of  $[M^{n+}(\text{NO}_3^-)_{n+1}]^-$  Anions Originating from Metal Nitrates  $M(\text{NO}_3)_n$ . *Int. J. Mass Spectrom.* **2014**, *369*, 98-104.
- [2] Li, F.; Byers, M.A.; Houk, R.S. Tandem Mass Spectrometry of Metal Nitrate Negative Ions Produced by Electrospray Ionization. *J. Am. Soc. Mass Spectrom.* **2003**, *14* (6), 671-679.
- [3] Pruitt, C.J.M.; Goebbert, D.J. Experimental and Theoretical Study of the Decomposition of Copper Nitrate Cluster Anions. *J. Phys. Chem. A.* **2015**, *119* (20), 4755-4762.
- [4] Albury, R.M.; Pruitt, C.J.M.; Hester, T.H.; Goebbert, D.J. Fragmentation of  $\text{Cr}(\text{NO}_3)_4^-$ : Metal Oxidation upon  $\text{O}^-$  Abstraction. *J. Phys. Chem. A.* **2015**, *119* (47), 11471-11478.
- [5] Lightcap, J.; Hester, T.H.; Kamena, K.; Albury, R.M.; Pruitt, C.J.M.; Goebbert, D.J. Gas-Phase Fragmentation of Aluminum Oxide Nitrate Anions Driven by Reactive Oxygen Radical Ligands. *J. Phys. Chem. A.* **2016**, *120* (9), 1501-1507.

- [6] Hester, T.H.; Albury, R.M.; Pruitt, C.J.M.; Goebbert, D.J. Fragmentation of  $[\text{Ni}(\text{NO}_3)_3]^-$ : A Study of Nickel-Oxygen Bonding and Oxidation States in Nickel Oxide Fragments. *Inorg. Chem.* **2016**, *55* (13), 6634-6642.
- [7] Hester, T.H.; Goebbert, D.J. Experimental and Theoretical Study of the Decomposition of  $[\text{Zn}(\text{NO}_3)_3]^-$ . *Chem. Phys. Lett.* **2016**, In Press.
- [8] Hester, T.H.; McCraney, K.K.; Castillo, D.E.; Goebbert, D.J. The Sequential Dissociation of Protonated Polyethylene Glycols. *J. Mass Spectrom.* **2013**, *48* (4), 459-464.
- [9] Hester, T.H.; Castillo, D.E.; Goebbert, D.J. Fragmentation of Deprotonated Polyethylene Glycols,  $[\text{PEG} - \text{H}]^-$ . *R. Comm. Mass Spectrom.* **2013**, *27* (14), 1643-1648.
- [10] Henderson, W.; McIndoe, J.S.: *Mass Spectrometry of Inorganic, Coordination and Organometallic Compounds*, John Wiley & Sons, Inc., Chichester, 2005.
- [11] Crotti, S.; Traldi, P.; Seraglia, R. Review: Some Thoughts on Electrospray Ionization Mechanisms. *Eur. J. Mass Spectrom.* **2011**, *17* (2), 85-99.
- [12] Wilm, M. Principles of Electrospray Ionization. *Molec. and Cell. Proteomics.* **2011**, *10* (7), July 1, 2011.
- [13] Konermann, L.; Ahadi, E.; Rodriguez, A.D.; Vahidi, S. Unraveling the Mechanism of Electrospray Ionization. *Anal. Chem.* **2013**, *85* (1), 2-9.
- [14] Bachrach, S.M.: *Computational Organic Chemistry*, John Wiley & Sons, Inc., Hoboken, NJ, 2007.
- [15] Cramer, C.J.: *Essentials of Computational Chemistry: Theories and Models*, John Wiley & Sons, Inc., Chichester, 2004.
- [16] Jensen, F.: *Introduction to Computational Chemistry*, John Wiley & Sons, Inc., Chichester, 2006.
- [17] Ramachandran, K.I.; Deepa, G.; Namboori, K.: *Computational Chemistry and Molecular Modeling: Principles and Applications*, Springer, Heidelberg, 2008.
- [18] Demtröder, W.: *Atoms, Molecules and Photons*, Springer, Heidelberg, 2010.

## CHAPTER 3

### GALLIUM NITRATE ANION COMPLEXES

Studies of gallium nitrate anion complexes were performed to determine the influence of cation size on the dissociation pathways. Previous studies on a main group metal system, aluminum nitrate, showed the formation of multiple metal oxides, various routes for O<sub>2</sub> loss, and nitrate isomerization.<sup>1</sup> The findings will be published in a peer-reviewed journal in 2016.

#### *3.1 Introduction*

Gas-phase metal nitrate anion complexes are readily generated by electrospray ionization. These complexes can be mass-selected and studied by mass spectrometry. Previous studies have shown metal nitrate anion clusters have interesting fragmentation patterns. The most common dissociation reactions involve loss of nitrate anion, loss of NO<sub>3</sub><sup>•</sup> by electron transfer from a nitrate ligand, and loss of NO<sub>2</sub><sup>•</sup> by transfer of O<sup>-</sup> from a nitrate ligand to the metal. Previous studies on metal nitrate complexes did not thoroughly examine fragmentation mechanisms, and no theoretical work has been carried out on these clusters. Conflicting assignments for metal oxidation states upon O<sup>-</sup> abstraction are found in the literature due to the lack of proper, in-depth investigation.<sup>2,3</sup> A recent paper suggested the oxygen anion, O<sup>-</sup>, typically oxidizes transition metals to yield O<sup>2-</sup>,<sup>2</sup> whereas an earlier study suggested metals are not oxidized due to their large ionization potentials.<sup>3</sup> However, no experimental or theoretical justification was provided for the assigned metal oxidation states in either study.

We used theoretical calculations in support of our experimental study of  $[\text{Cu}(\text{NO}_3)_2]^-$  dissociation<sup>4</sup> to show metal cations with a low-lying  $3d$  subshell are not oxidized upon  $\text{O}^{\bullet-}$  abstraction. Differences in the fragmentation reactions of  $[\text{Cu}(\text{NO}_3)_3]^-$  and  $[\text{Cu}(\text{NO}_3)_2]^-$  were compared, accounting for the electronic structure of the metal ion. Fragmentation of the Cu(I) complex,  $[\text{Cu}(\text{NO}_3)_2]^-$ , was interesting because the metal is not oxidized upon sequential  $\text{O}^{\bullet-}$  abstraction to yield  $[\text{CuO}(\text{NO}_3)]^-$  and  $[\text{CuO}_2]^-$ .

The dissociation reactions of main group metal nitrate complexes can be compared with transition metal clusters. The +3 oxidation state of the main group metal, gallium, is isoelectronic with  $\text{Cu}^+$ . Complexes containing  $\text{Ga}^{3+}$  should undergo similar  $\text{O}^{\bullet-}$  abstraction reactions to those of  $\text{Cu}^+$ , but metal oxidation is not possible for  $\text{Ga}^{3+}$ . This means the oxygen atom in  $[\text{GaO}(\text{NO}_3)_3]^-$  should retain radical character. Li and coworkers<sup>3</sup> reported  $[\text{Ga}(\text{NO}_3)_3]^-$  and  $\text{NO}_3^-$  as the sole products from collision-induced dissociation, CID, of  $[\text{Ga}(\text{NO}_3)_4]^-$ , but did not provide a mass spectrum. Frański and coworkers<sup>2</sup> also attributed the formation of  $[\text{Ga}(\text{NO}_3)_2]^-$  to sequential loss of  $\text{NO}_3^{\bullet}$ , but their published spectra show no peak corresponding to the single loss of  $\text{NO}_3^{\bullet}$ . Peaks were observed for  $[\text{GaO}(\text{NO}_3)_3]^-$ ,  $[\text{GaO}(\text{NO}_3)_2]^-$ ,  $[\text{Ga}(\text{NO}_3)_2]^-$ , and  $[\text{GaO}_2(\text{NO}_3)]^-$ . The major discrepancy between the previous sets of experiments and our more recent fragmentation spectrum is the assignment of a  $[\text{Ga}^{\text{II}}(\text{NO}_3)_3]^-$  product that is not observed as an intermediate for the formation of  $[\text{Ga}(\text{NO}_3)_2]^-$ .

Our group has investigated the fragmentation of a similar metal nitrate anion complex,  $[\text{Al}(\text{NO}_3)_4]^-$ . The major fragments corresponded to  $[\text{AlO}(\text{NO}_3)_3]^-$ ,  $[\text{AlO}_2(\text{NO}_3)_2]^-$ , and  $[\text{AlO}(\text{NO}_2)(\text{NO}_3)]^-$ . Experimental and theoretical studies revealed the  $[\text{AlO}(\text{NO}_2)(\text{NO}_3)]^-$  product is generated by  $^1\text{O}_2$  elimination from  $[\text{AlO}_2(\text{NO}_3)_2]^-$  through a complex mechanism involving oxygen atom transfer from a nitrate ligand. A previously published fragmentation

spectrum for the gallium nitrate system shows an unlabeled, low intensity peak corresponding to  $[\text{GaO}_2(\text{NO}_3)_2]^-$ , the ion analogous to  $[\text{AlO}_2(\text{NO}_3)_2]^-$ . This ion could eliminate  $\text{O}_2$  to yield  $[\text{Ga}(\text{NO}_3)_2]^-$  or the isomer,  $[\text{GaO}(\text{NO}_2)(\text{NO}_3)]^-$ .

The decomposition of  $[\text{Ga}(\text{NO}_3)_4]^-$  and  $[\text{Al}(\text{NO}_3)_4]^-$  show many similarities, as expected for metals belonging to the same group. Related dissociation mechanisms were expected to occur for  $[\text{Ga}(\text{NO}_3)_4]^-$ , and one goal of this study was to investigate sequential decomposition reactions using both experiment and theory. In addition, we investigated whether the  $[\text{Ga}(\text{NO}_3)_3]^-$  fragment could be detected, and how the ion corresponding to the nominal loss of two  $\text{NO}_3^\bullet$  molecules is formed. We report experimental and theoretical studies of  $[\text{Ga}(\text{NO}_3)_4]^-$  decomposition, and the previously unstudied oxide complexes  $[\text{GaO}(\text{NO}_3)_3]^-$  and  $[\text{GaO}_2(\text{NO}_3)_2]^-$  by collision-induced dissociation.

### 3.2 Methods

A solution with 1 mM concentration was prepared by dissolving a sample of gallium nitrate hydrate (0.033 g, 98% pure, Acros Organics), purchased from VWR International (Randor, PA, USA), in a mixture of HPLC-grade solvents, methanol (50 mL) and acetonitrile (50 mL). The TSQ-7000 tandem mass spectrometer (Finnigan MAT, San Jose, CA) was used for dissociation experiments. Authentic product ions were generated by in-source fragmentation for CID and ERMS studies.

Density functional calculations were performed using the (U)B3LYP functional and the 6-311G+(df) basis set. Open-shell calculations were performed for singlet complexes to determine the relative energies of the closed- and open-shell singlet species. The keyword “guess = (mix, always)” was used to disfavor electron pairing for open-shell singlet calculations.

The lowest energy structures, with correct spin-states, were determined by geometry optimization. Natural population analysis, NPA, calculations were performed on the optimized structures to determine the electron configurations, spin densities, and atomic charges of the metal and oxygen ligands.

### 3.3 Experimental Results

Four ions were studied experimentally in this work: the gallium nitrate anion,  $[\text{Ga}(\text{NO}_3)_4]^-$ , and the oxide complexes  $[\text{GaO}(\text{NO}_3)_3]^-$ ,  $[\text{GaO}_2(\text{NO}_3)_2]^-$ , and  $[\text{GaO}(\text{NO}_3)_2]^-$ . These species and their observed CID fragments were investigated using theory. The main focus of these studies is to determine the mechanism of fragmentation for  $[\text{GaO}_2(\text{NO}_3)_2]^-$ . This ion is expected to eliminate neutral  $\text{O}_2$  via O-O bond formation and electron transfer to the metal. This process was observed for the similar Group 13 aluminum oxide nitrate anions.

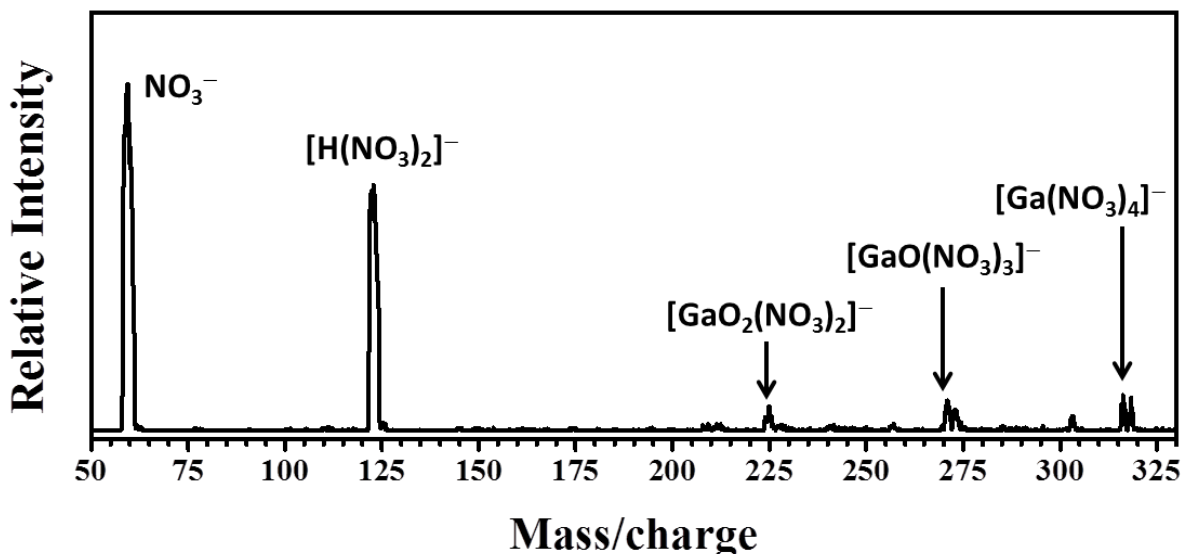


Figure 3.1 Representative Q1MS spectrum of gallium nitrate solution.

The Q1MS spectrum in Figure 3.1 shows a range of ions are produced in the source region. The precursor ion,  $[\text{Ga}(\text{NO}_3)_4]^-$ , and two in-source fragments,  $[\text{GaO}(\text{NO}_3)_3]^-$  and

$[\text{GaO}_2(\text{NO}_3)_2]^-$ , are present at moderate intensity. The typical nitrate solution species,  $[\text{H}(\text{NO}_3)_2]^-$  and  $\text{NO}_3^-$ , are also labeled in the spectrum. The spectra obtained for gallium nitrate solutions were noisy compared to the other metal nitrate studies, presumably due to a low quality solid sample purchased from VWR International.

The  $[\text{Ga}(\text{NO}_3)_4]^-$  complex at  $m/z$  317 was chosen as the precursor due to the higher relative abundance of the  $^{69}\text{Ga}$  isotope. This complex was subjected to CID and yields the fragments shown in Figure 3.2A. A large intensity peak corresponding to the loss of  $\text{NO}_2^\bullet$ , labeled as  $[\text{GaO}(\text{NO}_3)_3]^-$ , is observed along with other low intensity gallium-containing peaks. The spectrum in Figure 3.2A agrees with a previously published study using a quadrupole-time-of-flight, Q-TOF, mass spectrometer, with slight variation in relative peak intensity for the different instrumental setups and dissociation energies.<sup>2</sup>

Figure 3.2B shows the CID spectrum for  $[\text{GaO}(\text{NO}_3)_3]^-$ . This intermediate is present at low intensity in the Q1MS spectrum, Figure 3.1, but was generated with higher intensity by modifying the source conditions as discussed in Chapter 2. All of the gallium-containing fragments in Figure 3.2A are sequential dissociation products from the  $[\text{GaO}(\text{NO}_3)_3]^-$  intermediate. Figure 3.2B shows primary fragment peaks corresponding to the elimination of  $\text{O}_2$ ,  $\text{NO}_2^\bullet$ , and  $\text{NO}_3^\bullet$  to yield  $[\text{Ga}(\text{NO}_2)(\text{NO}_3)_2]^-$ ,  $[\text{GaO}_2(\text{NO}_3)_2]^-$ , and  $[\text{GaO}(\text{NO}_3)_2]^-$  respectively. The irregular formula for  $[\text{Ga}(\text{NO}_2)(\text{NO}_3)_2]^-$ , an ion generated by loss of  $\text{O}_2$ , will be discussed. Secondary fragments are also labeled as  $[\text{Ga}(\text{NO}_3)_2]^-$ ,  $[\text{GaO}_2(\text{NO}_3)]^-$ , and  $[\text{GaO}_2]^-$ .

Figure 3.2C shows the CID spectrum for  $[\text{GaO}_2(\text{NO}_3)_2]^-$ . The most important fragment to notice is  $[\text{Ga}(\text{NO}_3)_2]^-$ , which corresponds to  $\text{O}_2$  elimination from  $[\text{GaO}_2(\text{NO}_3)_2]^-$ . These CID spectra reveal the formation of  $[\text{Ga}(\text{NO}_3)_2]^-$  occurs via sequential loss of  $\text{NO}_2^\bullet$ , followed by  $\text{O}_2$  elimination. The other primary fragment,  $[\text{GaO}(\text{O}_2)(\text{NO}_3)]^-$  is produced via elimination of  $\text{NO}_2^\bullet$ .

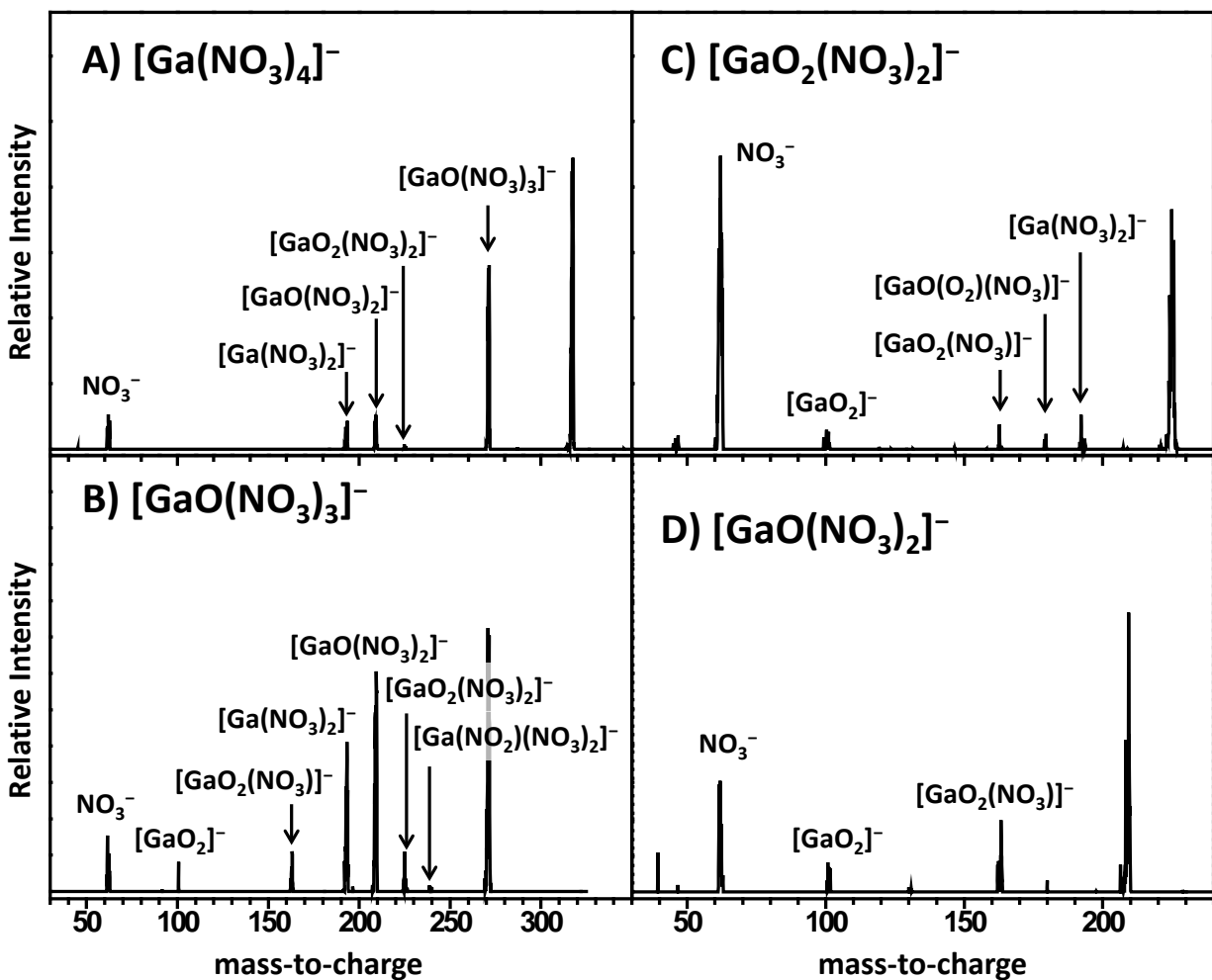


Figure 3.2 CID mass spectra of (A)  $[\text{Ga}(\text{NO}_3)_4]^-$ , (B)  $[\text{GaO}(\text{NO}_3)_3]^-$ , (C)  $[\text{GaO}_2(\text{NO}_3)_2]^-$ , and (D)  $[\text{GaO}(\text{NO}_3)_2]^-$ . Spectra were recorded using 1.00 mTorr of Ar collision gas at 30 eV<sub>lab</sub> for (A) and (B) and 50 eV<sub>lab</sub> for (C) and (D).

from  $[\text{GaO}_2(\text{NO}_3)_2]^-$ . The remaining gallium-containing ions,  $[\text{GaO}_2(\text{NO}_3)]^-$  and  $[\text{GaO}_2]^-$ , are observed in both CID spectra in Figures 3.2C-D. They can be produced via sequential losses of  $\text{NO}_3^\bullet$  from  $[\text{GaO}_2(\text{NO}_3)_2]^-$  or via consecutive loss of  $\text{NO}_2^\bullet$  and  $\text{NO}_3^\bullet$  from  $[\text{GaO}(\text{NO}_3)_2]^-$ .

Energy-dependent CID spectra were recorded for the precursor,  $[\text{Ga}(\text{NO}_3)_4]^-$ . The relative intensities of the fragments are plotted as a function of the center-of-mass collision energy. Figure 3.3 shows a representative spectrum for the two product ions with sufficient intensity for recording ERMS data. The curves for elimination of  $\text{NO}_2^\bullet$  and loss of nitrate anion both have an onset around 1 eV, suggesting the dissociation reactions for these processes occur with similar energy. The higher intensity of the  $[\text{GaO}(\text{NO}_3)_3]^-$  fragment relative to that of  $\text{NO}_3^-$  is consistent with the relative intensities observed in the CID spectrum for  $[\text{Ga}(\text{NO}_3)_4]^-$ ,

Figure 3.2A.

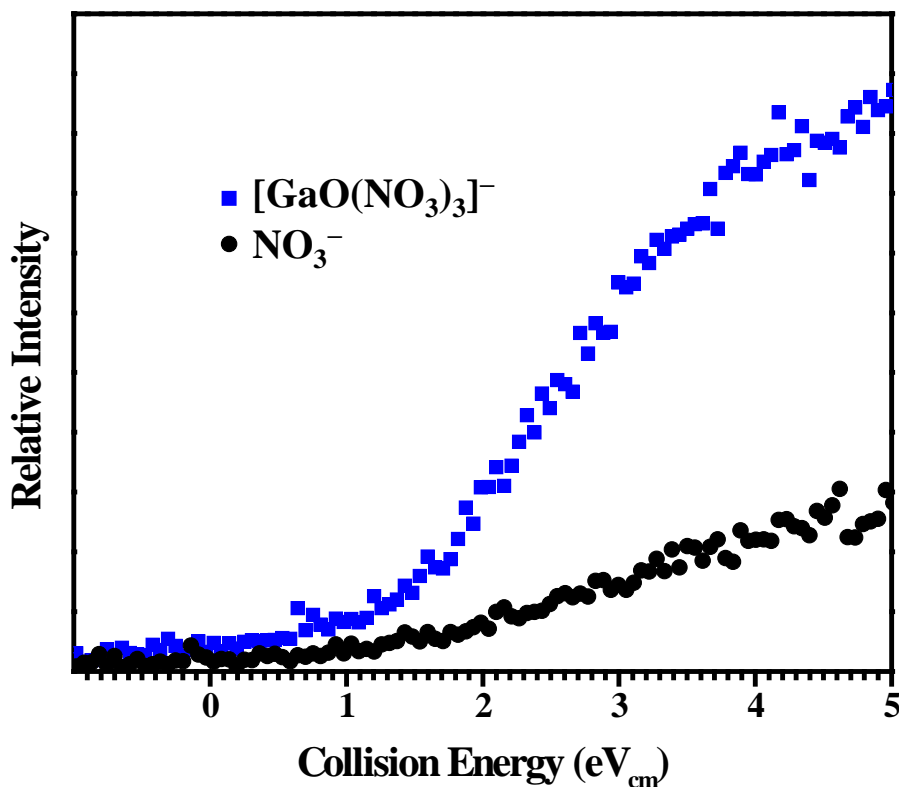


Figure 3.3 Energy-dependent fragmentation spectra for dissociation of  $[\text{Ga}(\text{NO}_3)_4]^-$ .

### 3.4 Theoretical Results

Calculations were performed on the precursor ion and all of the observed products. The complexes will be discussed following the dissociation schemes shown in Figures 3.4-3.6. Selected geometric parameters are provided for each structure, including distances for nitrate oxygen-metal coordination  $R_{\text{avg}}(\text{Ga-O})$  and for unique Ga-O and O-O bonds. The reaction energies assigned to each process are the lower limits for decomposition, equal the energy difference of the reactant and product. Transition states were not calculated for processes whose transition states were considered to be “loose”, whereas transition state structures were located and shown explicitly for reactions with “tight” transition states.

Figure 3.4 shows the calculated structure of the  $[\text{Ga}(\text{NO}_3)_4]^-$  precursor with a gallium cation surrounded by four nitrate ligands. Natural population analysis, NPA, calculations show gallium with a charge of +1.639, lower than the expected +3 charge due to donation of electron density from the ligands. The calculated electronic energy difference for  $\text{NO}_2^\bullet$  elimination is 2.06 eV, similar to the 2.07 eV calculated for  $\text{NO}_3^-$  loss. The experimental onsets, extrapolated to around 1 eV, differ from the calculated energies due to excess internal energy of the ions.

The  $[\text{GaO}(\text{NO}_3)_3]^-$  complex contains a  $[\text{GaO}]^{2+}$  core coordinated to three nitrate ligands. The Ga-O bond distance was calculated to be 1.82 Å. The NPA charges are +1.764 for gallium and -0.618 for oxygen. The charge ratio of -2.85 is similar to the expected value of -3 for the  $\text{Ga}^{3+}[\text{O}^{\bullet-}]$  ion contact pair. The abstraction of  $\text{O}^{\bullet-}$  does not result in metal reduction or oxidation. Rather, the oxygen ligand retains the radical in the product complex,  $[\text{GaO}(\text{NO}_3)_3]^-$ .

Figure 3.4 predicts the reaction,  $[\text{GaO}(\text{NO}_3)_3]^- \rightarrow [\text{GaO}_2(\text{NO}_3)_2]^- + \text{NO}_2^\bullet$ , occurs with a calculated energy of 2.10 eV, similar in energy to the first  $\text{NO}_2^\bullet$  loss. The  $[\text{GaO}_2(\text{NO}_3)_2]^-$  product was calculated with an open-shell singlet ground state using the procedure from the

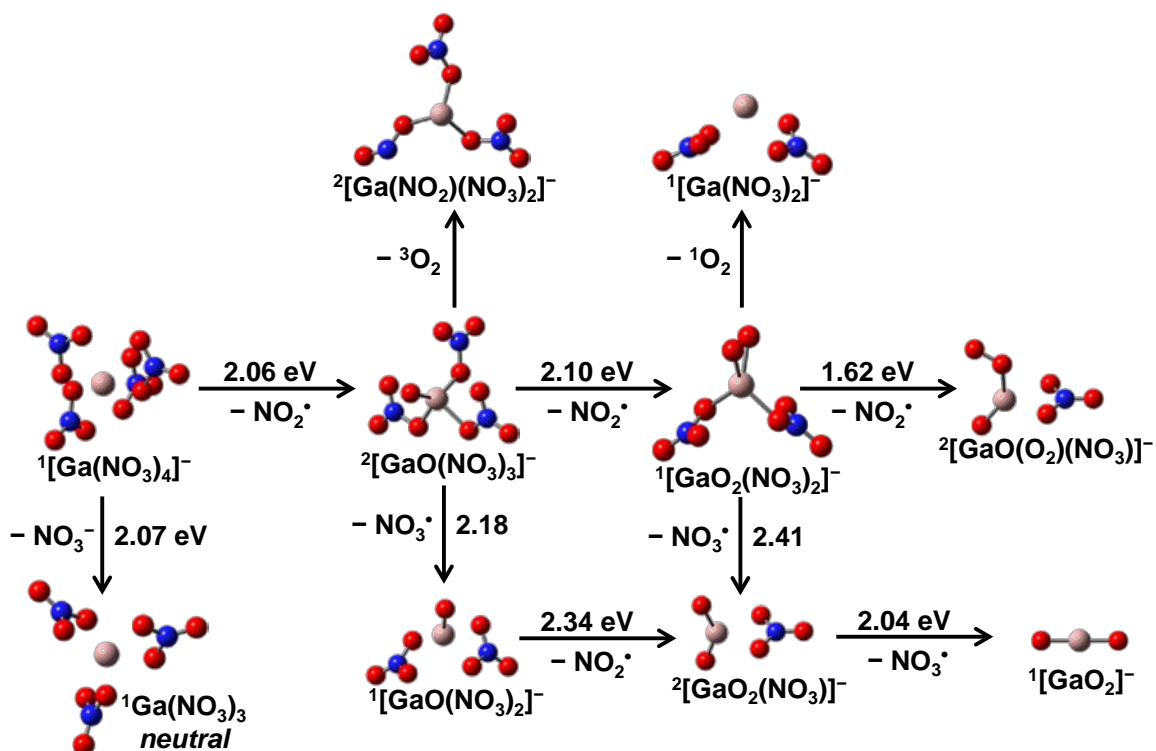


Figure 3.4 Calculated relative energy differences for the decomposition of  $[\text{Ga}(\text{NO}_3)_4]^-$  at the (U)B3LYP/6-311+G(df) level of theory. All energies include zero-point corrections. Atom colors: pink for gallium, blue for nitrogen, and red for oxygen.

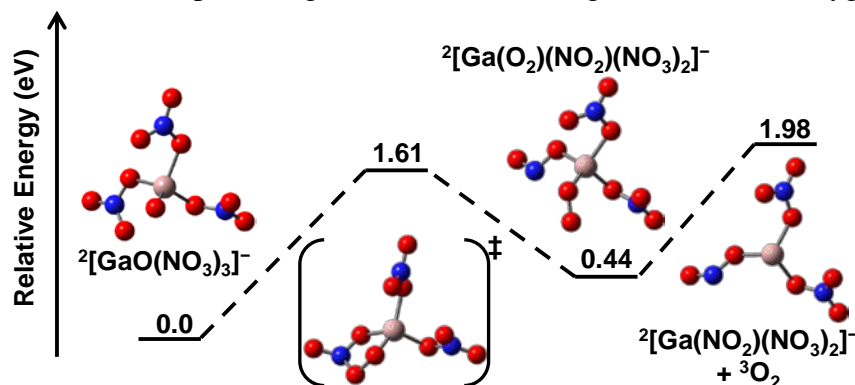


Figure 3.5 Potential energy diagram for  $^3\text{O}_2$  elimination from  $[\text{GaO}(\text{NO}_3)_3]^-$ .

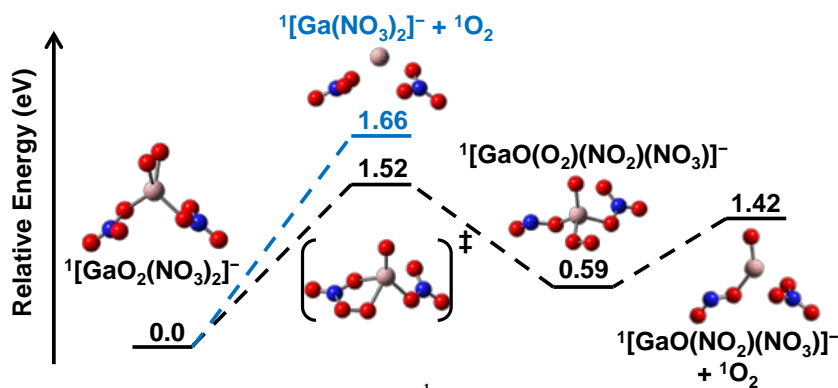


Figure 3.6 Potential energy diagram for  $^1\text{O}_2$  elimination from  $[\text{GaO}_2(\text{NO}_3)_2]^-$ .

*Methods* section of this chapter. The complex is  $C_2$ -symmetric and contains two monodentate nitrate ligands coordinated to a  $[\text{GaO}_2]^+$  core. The oxygen atoms are located in close proximity to one another, at an O-Ga-O angle of  $52.1^\circ$ . The O-O bond distance is  $1.60 \text{ \AA}$ , consistent with that of a peroxide,  $\text{O}_2^{2-}$ , ligand. The distance from gallium to the center of the peroxide ligand is  $1.60 \text{ \AA}$ .

The elimination reaction,  $[\text{GaO}(\text{NO}_3)_3]^- \rightarrow [\text{GaO}(\text{NO}_3)_2]^- + \text{NO}_3^\bullet$ , was calculated with an electronic energy difference of  $2.18 \text{ eV}$ , nearly identical to the  $2.10 \text{ eV}$  calculated for  $\text{NO}_2^\bullet$  elimination. The product,  $[\text{GaO}(\text{NO}_3)_2]^-$ , contains a  $[\text{GaO}]^+$  core. The NPA charges of  $+1.700$  for gallium and  $-1.273$  for oxygen indicate this metal oxide core is best described as the  $\text{Ga}^{3+}[\text{O}^{2-}]$  ion contact pair.

The  $[\text{GaO}(\text{NO}_3)_3]^-$  complex has a third dissociation reaction,  $[\text{GaO}(\text{NO}_3)_3]^- \rightarrow [\text{Ga}(\text{NO}_2)(\text{NO}_3)_2]^- + \text{O}_2$ . Figure 3.5 shows how the  $[\text{GaO}(\text{NO}_3)_3]^-$  complex undergoes isomerization of a nitrate ligand to eliminate  $\text{O}_2$  and yield the  $[\text{Ga}(\text{NO}_2)(\text{NO}_3)_2]^-$  product. The potential energy diagram shows an oxygen atom is transferred from a nitrate ligand to the  $\text{O}^{\bullet-}$  ligand, producing the intermediate,  $[\text{Ga}(\text{O}_2)(\text{NO}_2)(\text{NO}_3)_2]^-$ , over a transition state barrier of  $1.61 \text{ eV}$ . This intermediate eliminates  $\text{O}_2$  by electron transfer to the metal, yielding the  $[\text{Ga}(\text{NO}_2)(\text{NO}_3)_2]^-$  product at  $1.98 \text{ eV}$ .

The CID spectra in Figures 3.2C-D show  $[\text{GaO}_2(\text{NO}_3)_2]^-$  and  $[\text{GaO}(\text{NO}_3)_2]^-$  share a common fragment,  $[\text{GaO}_2(\text{NO}_3)]^-$ . The reaction,  $[\text{GaO}_2(\text{NO}_3)_2]^- \rightarrow [\text{GaO}_2(\text{NO}_3)]^- + \text{NO}_3^\bullet$ , is calculated to occur at  $2.41 \text{ eV}$ . The convergent reaction,  $[\text{GaO}(\text{NO}_3)_2]^- \rightarrow [\text{GaO}_2(\text{NO}_3)]^- + \text{NO}_2^\bullet$ , has a calculated energy of  $2.34 \text{ eV}$ . The identical product ion,  $[\text{GaO}_2(\text{NO}_3)]^-$ , contains a neutral  $\text{GaO}_2$  core with an O-Ga-O angle of  $140.8^\circ$ . The Ga-O bond distances are both  $1.75 \text{ \AA}$ . The complex has  $C_{2h}$  symmetry and NPA charges of  $+1.707$  for the gallium atom and  $-0.983$  for

each oxygen atom. The increased magnitude of the negative charges on the oxygen atoms indicate the metal oxide core is best considered as  $[\text{O}^{1.5-}]_2\text{Ga}^{3+}$ .

The  $[\text{GaO}_2(\text{NO}_3)]^-$  complex is calculated to eliminate  $\text{NO}_3^\bullet$  to yield  $[\text{GaO}_2]^-$  at 2.04 eV. The metal oxide product complex has an O-Ga-O angle of  $180^\circ$ , as shown in Figure 3.4. The gallium cation has an NPA charge of +1.643, consistent with  $\text{Ga}^{3+}$  and a  $-1.321$  charge for each oxygen atom, consistent with two  $\text{O}^{2-}$  ligands.

The CID spectrum in Figure 3.2C shows the dissociation reaction,  $[\text{GaO}_2(\text{NO}_3)_2]^- \rightarrow [\text{GaO}(\text{O}_2)(\text{NO}_3)]^- + \text{NO}_2^\bullet$ , occurs. Figure 3.4 shows this product is calculated to form at 1.64 eV, has  $C_s$  symmetry, and contains two oxygenic ligands within the neutral  $\text{OGa}(\text{O}_2)$  core. The NPA charge of +1.706 for gallium indicates the metal retains the +3 oxidation state upon  $\text{O}^\bullet$  abstraction. The oxygen ligand has an NPA charge of  $-1.277$ , indicative of the  $-2$  oxidation state. The bond distance between gallium and the oxygen ligand is  $1.69 \text{ \AA}$ . The dioxygen ligand has a combined charge of  $-0.710$  and a Ga-O bond distance of  $1.92 \text{ \AA}$ . The moderately negative NPA charge for the dioxygen ligand and the short O-O bond distance of  $1.33 \text{ \AA}$  are consistent with the presence of an  $\text{O}_2^{\bullet-}$  ligand in the core.<sup>5-8</sup>

The  $[\text{GaO}_2(\text{NO}_3)_2]^-$  complex was observed to eliminate  $\text{O}_2$  in Figure 3.2C. Calculations for this elimination yield two reasonable reactions, a direct elimination pathway via  $[\text{GaO}_2(\text{NO}_3)_2]^- \rightarrow [\text{Ga}(\text{NO}_3)_2]^- + \text{O}_2$  and a combined nitrate isomerization and subsequent elimination pathway via  $[\text{GaO}_2(\text{NO}_3)_2]^- \rightarrow [\text{GaO}(\text{NO}_2)(\text{NO}_3)]^- + \text{O}_2$ . Figure 3.6 shows the potential energy diagram for the two  $\text{O}_2$  loss routes for  $[\text{GaO}_2(\text{NO}_3)_2]^-$ . The estimated energy for  $^1\text{O}_2$  was determined using the theoretical energy for  $^3\text{O}_2$  with a correction factor from the experimental triplet-singlet splitting,  $0.98 \text{ eV}$ .<sup>9</sup> The formation of the product ion,  $[\text{Ga}(\text{NO}_3)_2]^-$ , was incorrectly attributed in the literature as occurring via sequential  $\text{NO}_3^\bullet$  loss from

$[\text{Ga}(\text{NO}_3)_4]^-$ .<sup>3</sup> The CID spectra in Figures 3.2A-C clearly show  $[\text{Ga}(\text{NO}_3)_2]^-$  is produced from  $[\text{Ga}(\text{NO}_3)_4]^-$  via sequential  $\text{NO}_2^\bullet$  loss, followed by loss of  $\text{O}_2$ . The  $[\text{GaO}_2(\text{NO}_3)_2]^-$  ion can directly eliminate  $\text{O}_2$ , as shown in blue, at 1.66 eV, or undergo a slightly lower energy isomerization pathway, shown in black. The energy of the nitrate isomerization transition state is 1.52 eV. The  $[\text{GaO}(\text{O}_2)(\text{NO}_2)(\text{NO}_3)]^-$  intermediate is formed at 0.59 eV relative to  $[\text{GaO}_2(\text{NO}_3)_2]^-$ . The product,  $[\text{GaO}(\text{NO}_2)(\text{NO}_3)]^-$ , is formed spontaneously upon isomerization since the energy of the products, 1.42 eV, is lower than the transition state barrier.

### 3.5 Gallium-Oxygen Bonding

The nature of the metal oxide bonds in the gallium complexes was analyzed using NPA calculations. The gallium oxide bond of  $[\text{GaO}(\text{NO}_3)_3]^-$  is produced via  $\text{O}^\bullet$  abstraction by the metal. A hypothetical MO diagram is shown in Figure 3.7 for the formation of the Ga-O bond of the  $[\text{GaO}]^{2+}$  core. The filled  $3d$  subshell does not engage in bonding and the oxygen retains the unpaired electron. The calculated charge of +1.764 corresponds to Ga in the +3 oxidation state, indicating no reduction or oxidation of gallium upon  $\text{O}^\bullet$  abstraction. A closer look at the NPA charge of -0.618 for oxygen shows the radical electron is located on the oxygen atom. The experimentally observed loss of  $\text{O}_2$  from this complex supports the description of the  $[\text{GaO}]^{2+}$  core as having a radical oxygen ligand. The radical electron drives the nitrate isomerization process, in which an oxygen atom is transferred to the  $\text{O}^\bullet$  ligand to yield a superoxide ligand. This superoxide ligand is ultimately eliminated as neutral  $\text{O}_2$ .

Elimination of  $\text{NO}_2^\bullet$  from  $[\text{GaO}(\text{NO}_3)_3]^-$  yields  $[\text{GaO}_2(\text{NO}_3)_2]^-$ . The  $[\text{GaO}_2]^+$  core of this complex contains a gallium atom in the +3 oxidation state, with an NPA charge of +1.768 and two oxygen atoms with an identical -0.674 charge. The  $[\text{GaO}_2]^+$  core has an O-Ga-O angle of

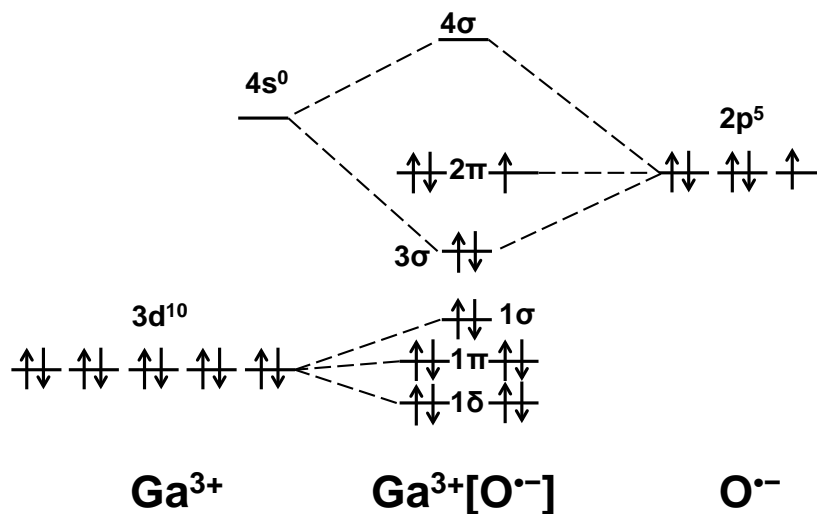


Figure 3.7 Hypothetical zero-order orbital interaction diagram illustrating the formation of  $[\text{GaO}]^{2+}$  from  $\text{Ga}^{3+}$  and  $\text{O}^{\bullet-}$ .

$52.1^\circ$  and an O-O bond distance of  $1.60 \text{ \AA}$ , indicative of a peroxide,  $\text{O}_2^{2-}$ , ligand. The singlet multiplicity for the complex and the zero value for Mulliken spin indicate the core is closed-shell, consistent with the presence of a peroxide ligand.

The  $[\text{GaO}_2(\text{NO}_3)_2]^-$  ion can undergo  $\text{O}^{\bullet-}$  abstraction upon elimination of  $\text{NO}_2^\bullet$  to yield the neutral  $\text{OGa}(\text{O}_2)$  core in  $[\text{GaO}(\text{O}_2)(\text{NO}_3)]^-$ . This core has a doublet spin multiplicity and contains a  $\text{Ga}^{3+}$  cation, an  $\text{O}^{2-}$  ligand, and an  $\text{O}_2^{\bullet-}$  ligand. The gallium atom has a  $+1.706$  calculated charge. The dioxygen ligand has a combined NPA charge of  $-0.710$  and a combined  $1.00\alpha$  Mulliken spin value, whereas the oxygen ligand has a  $-1.277$  charge. The core can be accurately described as  $[\text{O}^{2-}]\text{Ga}^{3+}[\text{O}_2^{\bullet-}]$ .

The  $[\text{GaO}_2(\text{NO}_3)_2]^-$  ion can undergo oxygen ligand reduction upon elimination of  $\text{NO}_3^\bullet$  to yield a neutral  $\text{OGaO}$  core of  $[\text{GaO}_2(\text{NO}_3)]^-$ . This neutral core has a doublet spin multiplicity and contains a  $\text{Ga}^{3+}$  cation, an  $\text{O}^{\bullet-}$  ligand, and an  $\text{O}^{2-}$  ligand. The identical oxygen atom charges of  $-0.983$  and Mulliken spin values of  $0.57\alpha$  indicate equal distribution of radical character over both oxygen atoms, yielding a core that is best described as  $[\text{O}^{1.5-}]\text{Ga}^{3+}[\text{O}^{1.5-}]$ .

The  $[\text{GaO}_2(\text{NO}_3)]^-$  complex can undergo elimination of  $\text{NO}_3^\bullet$  to yield  $[\text{GaO}_2]^-$ . This metal oxide anion contains gallium in the +3 oxidation state and two oxygen ligands, both in the -2 oxidation state. The NPA charges are +1.643 for the gallium atom and -1.321 for each oxygen atom. The gallium charge is significantly lowered due to donation of electron density from the highly negative oxygen ligands.

### 3.6 Conclusions

Elimination of  $\text{NO}_2^\bullet$  from gallium nitrate complexes can lead to Ga-O bond formation. This  $\text{O}^\bullet$  abstraction process does not cause metal oxidation or reduction since the vacant  $4s$  orbital of  $\text{Ga}^{3+}$  does not contain electrons that can be transferred and it is too high in energy to be reduced. The oxygen atom of the  $[\text{GaO}]^{2+}$  core retains the unpaired electron upon  $\text{O}^\bullet$  abstraction.

A superoxide,  $\text{O}_2^{\bullet-}$ , ligand can also be formed upon  $\text{O}^\bullet$  abstraction. The superoxide ligand of the neutral  $\text{OGa}(\text{O}_2)$  core is formed upon electron delocalization across the atoms in the metal oxide core. The oxygen atom and the  $\text{O}^\bullet$  ligand it abstracts are both partially oxidized upon O-O bond formation, whereas the remaining oxygen ligand is reduced to form an  $\text{O}^{2-}$  ligand.

Theoretical calculations show elimination of  $\text{NO}_3^\bullet$  results in the reduction of an available radical oxygen ligand to produce an  $\text{O}^{2-}$  ligand. The preference for ligand reduction is due to the lower energy  $2p$  orbital of  $\text{O}^\bullet$  that makes transfer of an electron favorable, whereas the vacant  $4s$  orbital of  $\text{Ga}^{3+}$  is too high in energy to favorably undergo electron transfer.

Two instances of  $\text{O}_2$  loss were observed to occur. Calculations show direct elimination via double electron transfer is slightly higher in energy than the transfer of an oxygen atom from

a nitrate ligand to an  $O^{\bullet-}$  ligand to produce a superoxide ligand. The  $O^{\bullet-}$  ligand receiving the O atom undergoes partial oxidation to form the O-O bond. The superoxide ligand ultimately transfers an electron to the metal to eliminate neutral  $O_2$ . The  $4s$  orbital is the lowest energy electron acceptor in both cases, and gallium becomes reduced accordingly.

### 3.7 References

- [1] Lightcap, J.; Hester, T.H.; Kamena, K.; Albury, R.M.; Pruitt, C.J.M.; Goebbert, D.J. Gas-Phase Fragmentation of Aluminum Oxide Nitrate Anions Driven by Reactive Oxygen Radical Ligands. *J. Phys. Chem. A*. **2016**, *120* (9), 1501-1507.
- [2] Frański, R.; Sobieszczuk, K.; Gierczyk, B. Mass Spectrometric Decomposition of  $[M^{n+}(NO_3^-)_{n+1}]^-$  Anions Originating from Metal Nitrates  $M(NO_3)_n$ . *Int. J. Mass Spectrom.* **2014**, *369*, 98-104.
- [3] Li, F.; Byers, M.A.; Houk, R.S. Tandem Mass Spectrometry of Metal Nitrate Negative Ions Produced by Electrospray Ionization. *J. Am. Soc. Mass Spectrom.* **2003**, *14* (6), 671-679.
- [4] Pruitt, C.J.M.; Goebbert, D.J. Experimental and Theoretical Study of the Decomposition of Copper Nitrate Cluster Anions. *J. Phys. Chem. A*. **2015**, *119* (20), 4755-4762.
- [5] Hersleth, H.-P.; Hsiao, Y.-W.; Ryde, U.; Görbitz, C.H.; Andersson, K.K. The Crystal Structure of Peroxymyoglobin Generated through Cryoradiolytic Reduction of Myoglobin Compound III During Data Collection. *Biochem. J.* **2008**, *412* (2), 257-264.
- [6] Pedio, M.; Wu, Z.Y.; Benfatto, M.; Mascaraque, A.; Michel, E.; Ottaviani, C.; Crotti, C.; Peloi, M.; Zacchigna, M.; Comincioli, C. NEXAFS Experiment and Multiple Scattering Calculations on  $KO_2$ : Effects on the  $\pi$  Resonance in the Solid Phase. *Phys. Rev. B*. **2002**, *66* (14), 144109/144101-144109/144104.
- [7] Sawyer, D.T.; Valentine, J.S. How Super Is Superoxide? *Acc. Chem. Res.* **1981**, *14* (12), 393-400.
- [8] Unno, M.; Chen, H.; Kusama, S.; Shaik, S.; Ikeda-Saito, M. Structural Characterization of the Fleeting Ferric Peroxo Species in Myoglobin: Experiment and Theory. *J. Am. Chem. Soc.* **2007**, *129* (44), 13394-13395.
- [9] Ervin, K.M.; Anusiewicz, I.; Skurski, P.; Simons, J.; Lineberger, W.C. The Only Stable State of  $O_2^-$  Is the  $X^2\Pi_g$  Ground State and It (Still!) Has an Adiabatic Electron Detachment Energy of 0.45 eV. *J. Phys. Chem. A*. **2003**, *107* (41), 8521-8529.

## CHAPTER 4

### ZINC NITRATE ANION COMPLEXES

Studies on zinc nitrate anion complexes were performed and reveal the importance of the low-lying *3d* subshell in how sequential dissociation proceeds. Upon formation of a zinc oxide core, the *3d* subshell is too low in energy to engage in mixing, leaving the oxygen ligand with a reactive radical that drives the observed dissociation. The findings were published as an article in 2016 in the journal *Chemical Physics Letters*.<sup>1</sup>

#### 4.1 Introduction

Zinc oxides,  $\text{ZnO}_x$ , are used as promoters,<sup>2,3</sup> co-catalysts,<sup>4,5</sup> or selective catalysts, such as in the degradation of chemical warfare agents.<sup>6,7</sup> The identification of reactive sites on  $\text{ZnO}_x$  surfaces is challenging due to a large number of surface defects and diverse topology.<sup>4,8</sup> Despite their extensive use, fundamental reaction mechanisms and physical properties of reactive sites often remain elusive. Complicated electronic structure, multiple spin states, and variable oxidation states make transition metal oxide materials more challenging to characterize than main group metal oxides. Unlike most *3d* metals, zinc has limited redox chemistry and is often considered a main group element rather than a transition metal.<sup>9,10</sup>

Metal oxide complexes can be readily synthesized from decomposition of metal nitrate anion clusters generated by electrospray ionization, ESI.<sup>11,12</sup> This study focuses on the decomposition and properties of  $[\text{Zn}(\text{NO}_3)_3]^-$  to form zinc oxide fragments decorated by nitrate ligands. The metal cation,  $\text{Zn}^{2+}$ , at the core of the complex can be compared with research on

previously studied metal nitrates:  $[\text{Cu}(\text{NO}_3)_2]^-$ ,  $[\text{Ni}(\text{NO}_3)_3]^-$ , and  $[\text{Al}(\text{NO}_3)_4]^-$ .<sup>13-15</sup> Zinc(II) is isoelectronic with copper(I); thus  $[\text{Cu}(\text{NO}_3)_2]^-$  and  $[\text{Zn}(\text{NO}_3)_3]^-$  complexes can be expected to have similar fragmentation. The copper complex undergoes elimination of  $\text{NO}_2^\bullet$  to yield  $[\text{CuO}(\text{NO}_3)]^-$  without metal oxidation. The neutral CuO core within  $[\text{CuO}(\text{NO}_3)]^-$  is best described as a  $\text{Cu}^+[\text{O}^\bullet]$  ion contact pair. Previous studies on zinc nitrate show the analogous reaction for  $[\text{Zn}(\text{NO}_3)_3]^-$  generates  $[\text{ZnO}(\text{NO}_3)_2]^-$ ,<sup>11,12</sup> and the  $[\text{ZnO}]^+$  core is expected to be a  $\text{Zn}^{2+}[\text{O}^\bullet]$  ion contact pair. The second elimination of  $\text{NO}_2^\bullet$  from  $[\text{CuO}(\text{NO}_3)]^-$  to yield  $[\text{CuO}_2]^-$  was also found to be a non-redox process, with the core best described as  $[\text{Cu}^+][\text{O}^\bullet]_2$ .<sup>13</sup> The analogous elimination of  $\text{NO}_2^\bullet$  from  $[\text{ZnO}(\text{NO}_3)_2]^-$  to yield  $[\text{ZnO}_2(\text{NO}_3)]^-$  should also be redox silent since the oxidation of zinc to the +3 oxidation state is not expected.<sup>16</sup>

Another factor influencing dissociation is the charge density of the metal. The charge of +1 on copper(I) is about half the magnitude of the +2 charge for zinc(II). Complexes containing divalent metal cations, such as  $\text{Ni}^{2+}$  within  $[\text{Ni}(\text{NO}_3)_3]^-$ , may exhibit fragmentation similar to  $[\text{Zn}(\text{NO}_3)_3]^-$  if dissociation is largely driven by charge density. The decomposition of  $[\text{Ni}(\text{NO}_3)_3]^-$  is complicated due to the  $3d^8$  electron configuration of nickel. Reduction of the nickel cation is predicted for several complexes<sup>14</sup> because of the increased charge density and the low energy unfilled  $3d$  orbitals in  $\text{Ni}^{2+}$ . Reduction of  $\text{Zn}^{2+}$  would require electron occupation of the  $4s$  orbital, and the large  $3d-4s$  energy splitting makes reduction less likely. The expectation of limited redox chemistry suggests the fragmentation of zinc complexes should be compared to main group metal cations. Our previous study on  $[\text{Al}(\text{NO}_3)_4]^-$  revealed significant dissociation.<sup>15</sup> The increased reactivity arises from the presence of a highly reactive oxygen radical anion ligand in the primary product ion,  $[\text{AlO}(\text{NO}_3)_3]^-$ . The aluminum cation in these complexes has the highest initial charge density of all the metals studied, but unlike the transition metals, oxidation

or reduction of aluminum is not favorable and the metal favors retention of the +3 oxidation state. These previous studies have demonstrated dissociation reactions depend on three factors: the electronic structure of the metal, the charge densities of the core atoms, and the overall redox chemistry. The current experiment uses a combination of mass spectrometry and theoretical calculations to investigate which factors are important to the decomposition of  $[\text{Zn}(\text{NO}_3)_3]^-$ .

#### 4.2 Methods

A solution with 1 mM concentration was prepared by dissolving a sample of zinc nitrate hexahydrate (0.030 g, 98% pure, Acros Organics), purchased from VWR International (Randor, PA, USA), in a mixture of HPLC grade solvents, methanol (50 mL) and acetonitrile (50 mL). The TSQ-7000 tandem mass spectrometer (Finnigan MAT, San Jose, CA) was used to perform CID and ERMS experiments. Authentic product ions were generated using in-source fragmentation for in-depth dissociation studies.

Density functional calculations were performed using the (U)B3LYP functional and the 6-311G+(df) basis set. The lowest energy structures, with correct spin-states, were determined using a standard approach involving geometry optimization, followed by determination of the lowest energy structures for the product ions. Natural population analysis, NPA, calculations were performed on the optimized structures to determine the electron configurations and atomic charges of the metal and oxygen ligands.

#### 4.3 Experimental Results

Two ions were studied experimentally in this work: the zinc nitrate ion,  $[\text{Zn}(\text{NO}_3)_3]^-$ , and the primary oxide complex,  $[\text{ZnO}(\text{NO}_3)_2]^-$ . These species and their observed CID fragments

were investigated using theory. The main focus of these studies is to determine common fragmentation reactions for the nitrate complexes of a pseudo-main group metal system.

The Q1MS spectrum in Figure 4.1 shows the observed anions:  $[\text{Zn}(\text{NO}_3)_3]^-$  around  $m/z$  250,  $[\text{H}(\text{NO}_3)_2]^-$  at  $m/z$  125, and  $\text{NO}_3^-$  at  $m/z$  62. The inset shows the isotopic distribution for zinc in the  $[\text{Zn}(\text{NO}_3)_3]^-$  complex. The higher relative abundance of the  $^{64}\text{Zn}$  isotope yields a high intensity precursor ion with  $m/z$  250 that was used for CID studies. This complex yielded the fragments shown in Figure 4.2A. A low-intensity peak corresponding to the loss of  $\text{NO}_2^\bullet$  and a higher intensity peak for the loss of  $\text{NO}_3^-$  were observed. The spectrum agrees well with a previously published spectrum recorded on a Q-TOF instrument.<sup>11</sup>

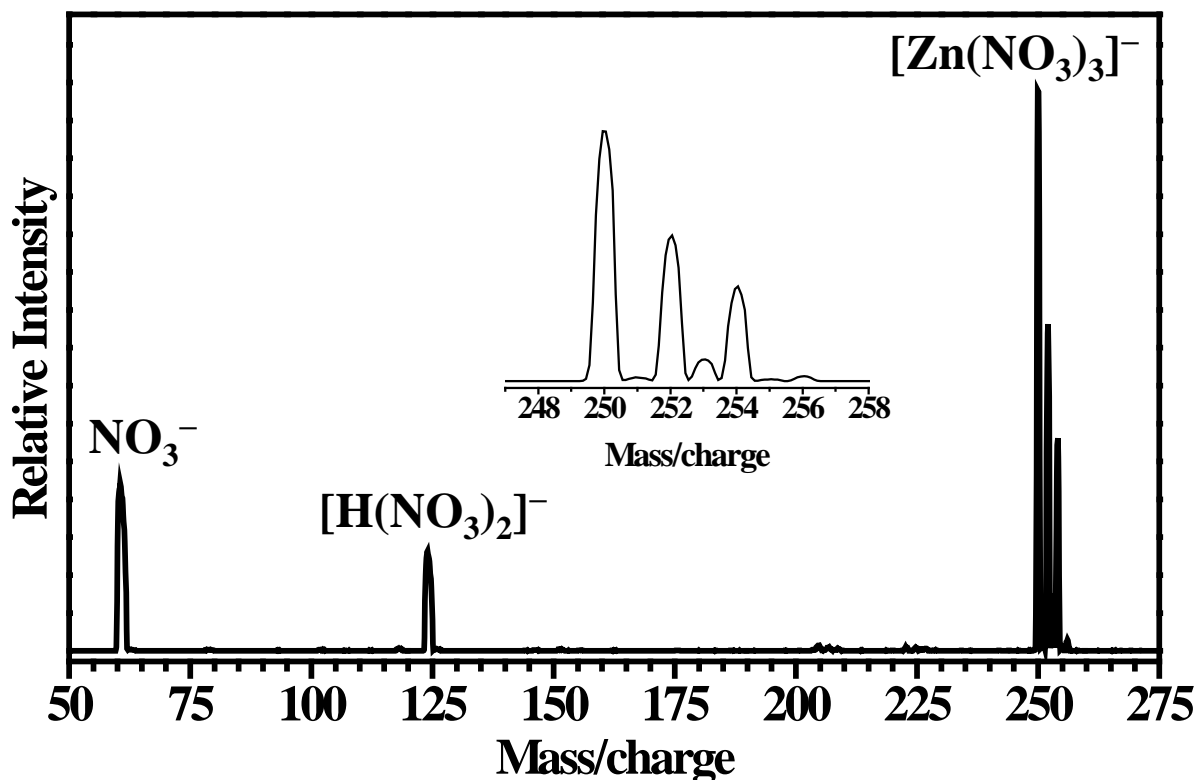


Figure 4.1 Representative Q1MS spectrum for the zinc nitrate solution. The inset shows an enlarged portion of the spectrum containing  $[\text{Zn}(\text{NO}_3)_3]^-$  to highlight the isotope pattern for Zn.

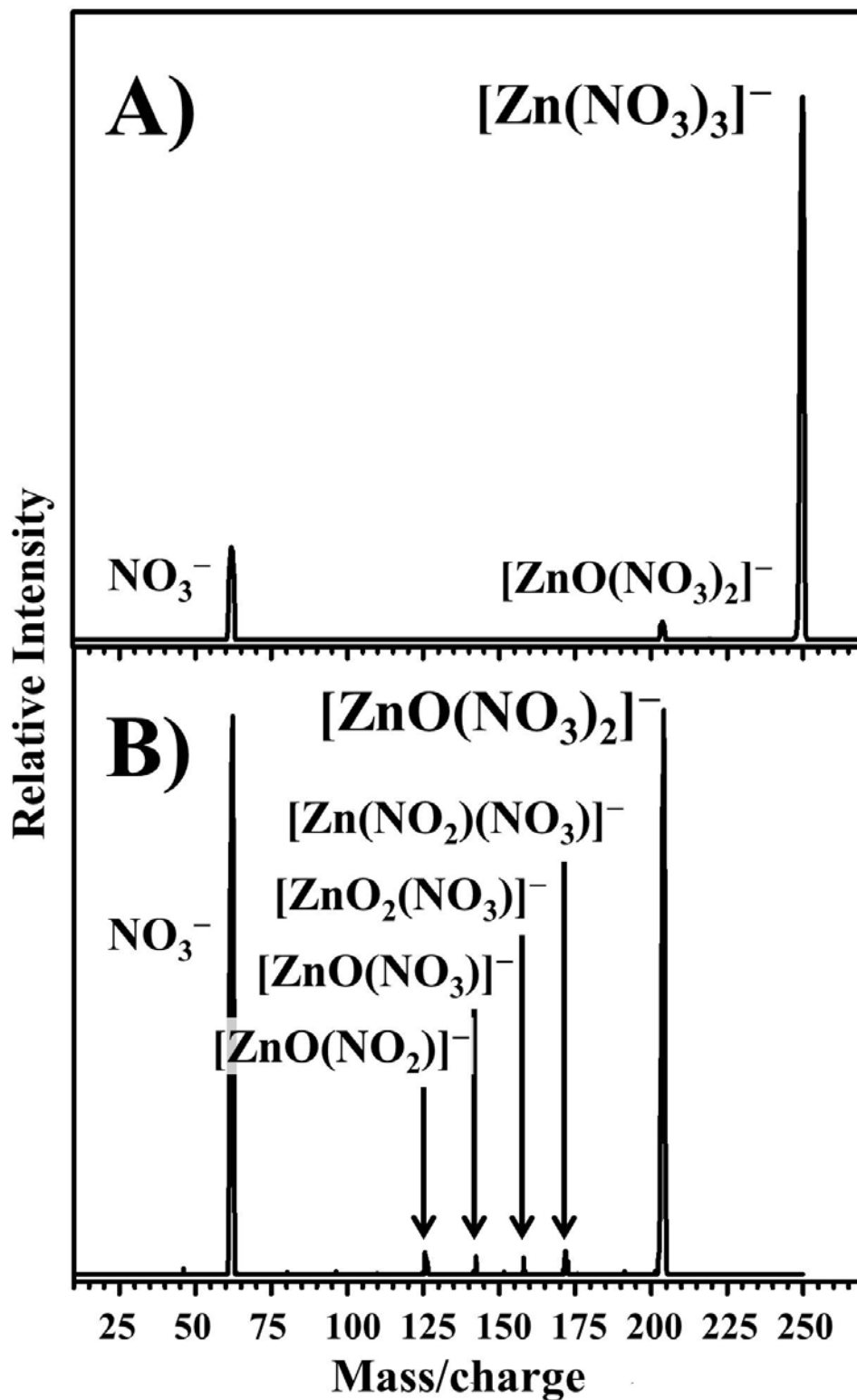


Figure 4.2 Representative CID spectra for (A)  $[\text{Zn}(\text{NO}_3)_3]^-$  and (B)  $[\text{ZnO}(\text{NO}_3)_2]^-$  at 30 eV<sub>lab</sub> collision energy with 0.50 mTorr Ar collision gas.

Figure 4.2B shows five observed fragments from the dissociation of  $[\text{ZnO}(\text{NO}_3)_2]^-$ . This ion was generated using the in-source fragmentation method discussed in Chapter 2. The  $\text{NO}_3^-$  fragment has the highest relative intensity, but is of less interest because it does not contain the metal. The primary fragments labeled as  $[\text{Zn}(\text{NO}_2)(\text{NO}_3)]^-$ ,  $[\text{ZnO}_2(\text{NO}_3)]^-$ , and  $[\text{ZnO}(\text{NO}_3)]^-$  correspond to losses of  $\text{O}_2$ ,  $\text{NO}_2^\bullet$ ,  $\text{NO}_3^\bullet$ , respectively. A secondary fragment, corresponding to loss of  $\text{O}_2$  from the  $[\text{ZnO}(\text{NO}_3)_2]^-$  intermediate, was also observed. The four equally intense zinc-containing fragments were not reported in previous studies on zinc nitrate dissociation due to their low yield from the  $[\text{ZnO}(\text{NO}_3)_2]^-$  intermediate.<sup>11,12</sup>

An energy-dependent CID spectrum, Figure 4.3, was recorded for the precursor ion,  $[\text{Zn}(\text{NO}_3)_3]^-$ . The formation of  $\text{NO}_3^-$  occurs with an onset around 1.2 eV, whereas the onset for  $\text{NO}_2^\bullet$  elimination is slightly higher at 1.4 eV. The intensity for  $\text{NO}_3^-$  is higher over the entire collision energy range. Energy-dependent spectra were not obtained for the  $[\text{ZnO}(\text{NO}_3)_2]^-$  ion due to low absolute intensity.

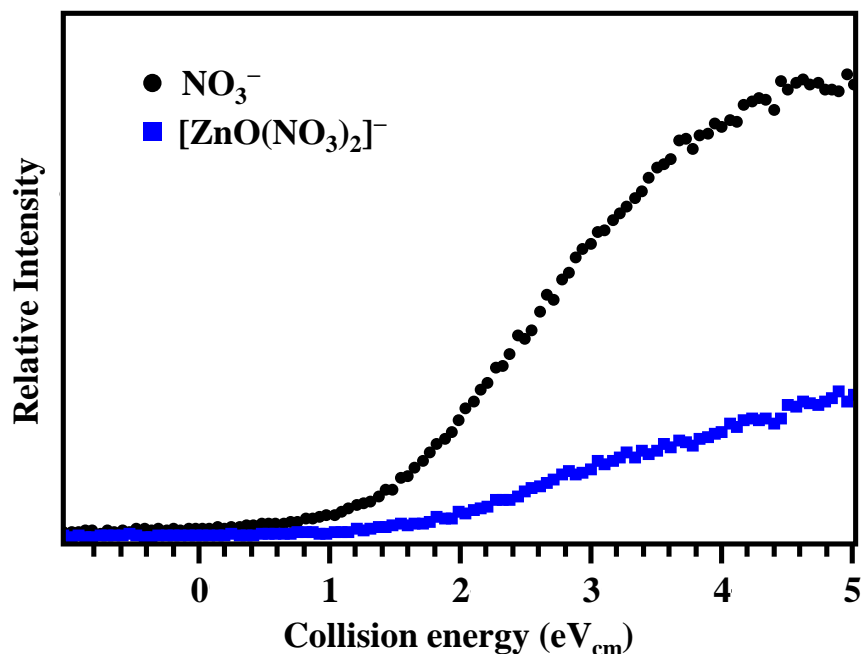


Figure 4.3 ERMS spectrum for the dissociation of  $[\text{Zn}(\text{NO}_3)_3]^-$ .

#### 4.4 Theoretical Results

Calculations were performed on the precursor ion and all observed dissociation products. Optimized structures of the zinc-containing ions are shown in Figures 4.4-4.6. Selected bond distances are given for unique Zn-O and O-O bonds. Figure 4.4 shows the  $[\text{Zn}(\text{NO}_3)_3]^-$  precursor has  $D_3$  symmetry with three nitrate ligands coordinated to the metal via two oxygen atoms. The relative electronic energy of reactants and products for the elimination of  $\text{NO}_3^-$  was calculated at 2.75 eV, slightly higher than the 2.47 eV calculated for  $\text{NO}_2^\bullet$  elimination. The theoretical energy difference between these two processes is similar to the experimental difference in ERMS appearance energies. The optimized  $C_2$ -symmetric structure of  $[\text{ZnO}(\text{NO}_3)_2]^-$  is similar to the precursor structure. Two nitrate ligands remain coordinated in a bidentate manner to the metal, with the oxygen atom occupying the original position of a nitrate ligand in the precursor. The calculated Zn-O bond distance for the metal oxide core is 1.88 Å.

Subsequent loss of  $\text{NO}_3^\bullet$  from the  $[\text{ZnO}(\text{NO}_3)_2]^-$  ion yields  $[\text{ZnO}(\text{NO}_3)]^-$  at 3.13 eV. The  $[\text{ZnO}(\text{NO}_3)]^-$  ion was calculated to have  $C_s$  symmetry, with the nitrate ligand coordinating to a neutral ZnO core via one oxygen atom. The Zn-O bond distance of 1.71 Å is shorter than for the precursor,  $[\text{ZnO}(\text{NO}_3)_2]^-$ .

Elimination of  $\text{NO}_2^\bullet$  from  $[\text{ZnO}(\text{NO}_3)_2]^-$  via  $\text{O}^{\bullet-}$  abstraction occurs at 2.76 eV. The abstraction of  $\text{O}^{\bullet-}$  is calculated to occur with slightly higher in energy than the first  $\text{O}^{\bullet-}$  abstraction. The  $[\text{ZnO}_2(\text{NO}_3)]^-$  product has  $C_{2v}$  symmetry. The neutral  $\text{ZnO}_2$  core has an O-Zn-O angle of 131.1°.

Figure 4.5 shows that  $\text{O}_2$  elimination from  $[\text{ZnO}(\text{NO}_3)_2]^-$  occurs via isomerization of a nitrate ligand. The nitrate ligand transfers an O atom to the  $\text{O}^{\bullet-}$  ligand over a low energy, 1.92 eV, transition state barrier to form the  $[\text{Zn}(\text{O}_2)(\text{NO}_2)(\text{NO}_3)]^-$  intermediate. Elimination of

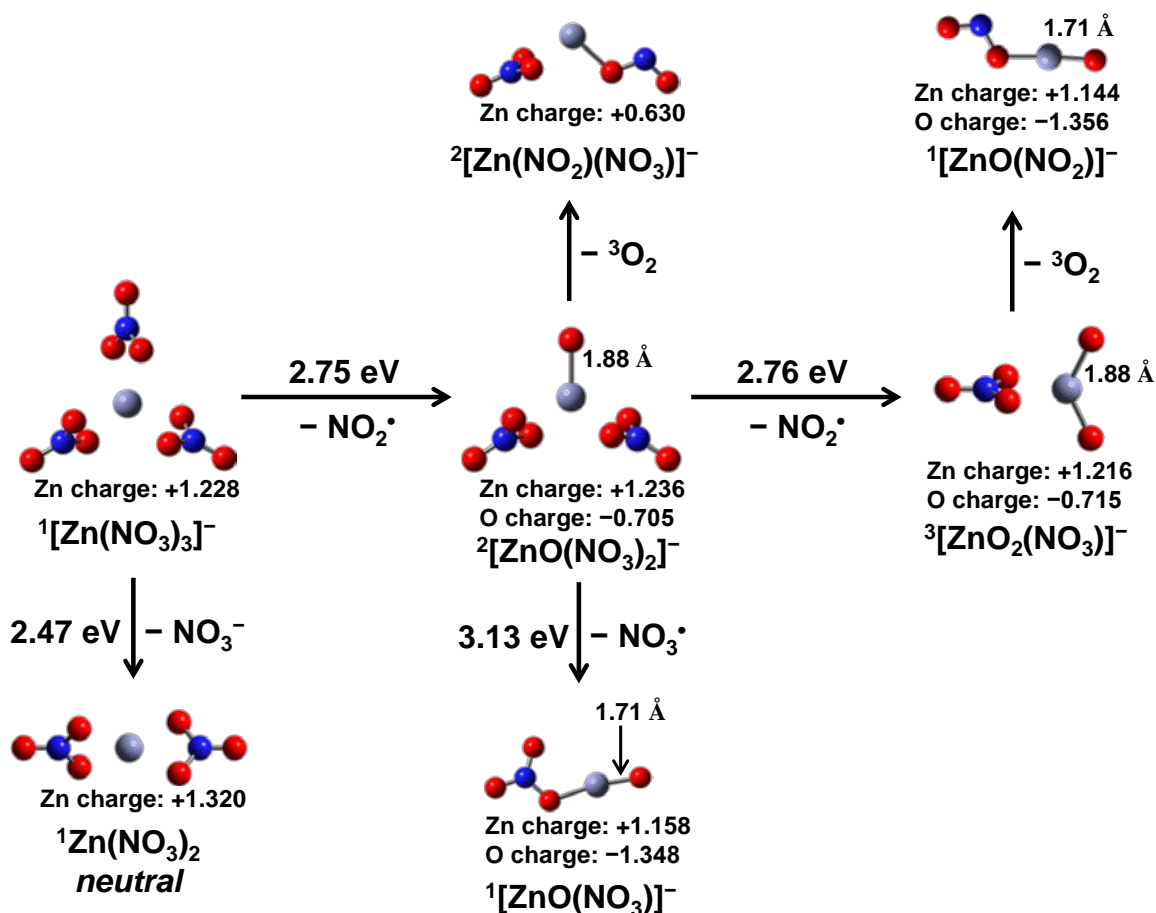


Figure 4.4 Calculated relative energy differences for the decomposition of  $[\text{Zn}(\text{NO}_3)_3]^-$  at the (U)B3LYP/6-311+G(df) level of theory. All energies include zero-point corrections. Select bond lengths and charges for the metal and unique oxygen atoms are indicated. Atom colors: gray for zinc, blue for nitrogen, and red for oxygen.

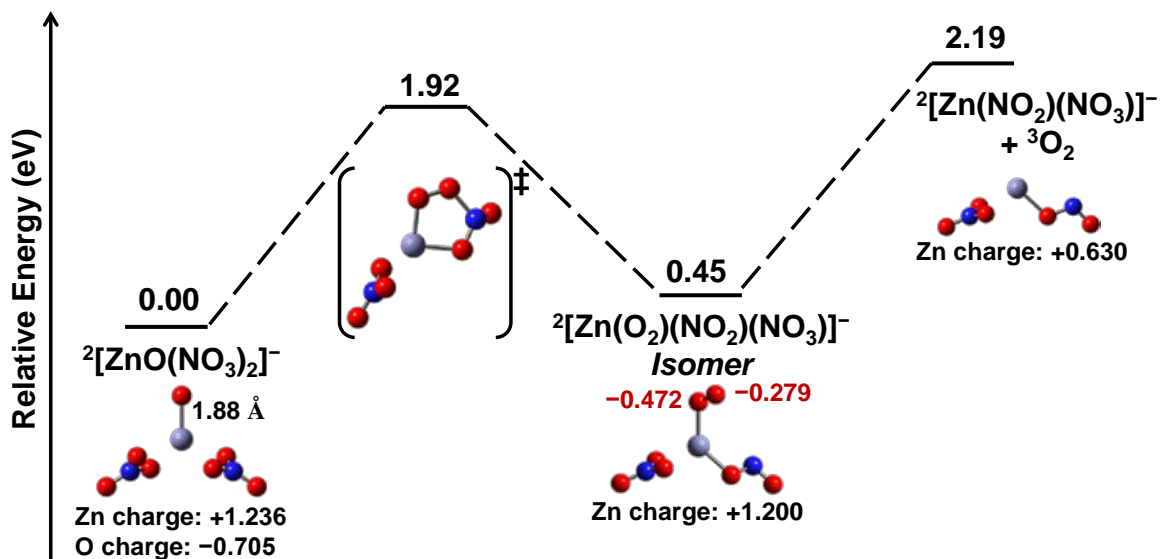


Figure 4.5 Potential energy diagram for  $^3\text{O}_2$  elimination from  $[\text{ZnO}(\text{NO}_3)_2]^-$ . All energies include zero-point corrections. Select bond lengths and NPA charges are indicated.

O<sub>2</sub> yields the [Zn(NO<sub>2</sub>)(NO<sub>3</sub>)]<sup>-</sup> product. The O<sub>2</sub> loss pathway is the lowest energy dissociation route for [ZnO(NO<sub>3</sub>)<sub>2</sub>]<sup>-</sup>, proceeding with an energy input of only 2.19 eV.

Sequential fragmentation of [ZnO<sub>2</sub>(NO<sub>3</sub>)]<sup>-</sup> occurs via elimination of O<sub>2</sub>, shown in Figure 4.6. The potential energy diagram shows two pathways that occur with similar overall energies. The direct elimination of O<sub>2</sub> involves the formation of an O-O bond over a 1.94 eV transition state barrier. The intermediate, [Zn(O<sub>2</sub>)(NO<sub>3</sub>)]<sup>-</sup>, contains a superoxide ligand that reduces the metal upon neutral O<sub>2</sub> loss to yield [Zn(NO<sub>3</sub>)]<sup>-</sup>. The structure of [Zn(NO<sub>3</sub>)]<sup>-</sup> has C<sub>s</sub> symmetry with an optimized structure, similar to that for [ZnO(NO<sub>3</sub>)]<sup>-</sup>. The entire direct elimination process results in double metal reduction, Zn<sup>2+</sup> → Zn, via electron transfer from the two O<sup>-</sup> ligands and elimination of neutral O<sub>2</sub>.

A lower energy route for O<sub>2</sub> loss proceeds over a 1.81 eV barrier via oxygen atom transfer from the nitrate ligand to one of the O<sup>-</sup> ligands, Figure 4.6. The intermediate, [ZnO(O<sub>2</sub>)(NO<sub>2</sub>)]<sup>-</sup> contains one O<sup>-</sup> ligand from the precursor structure and the newly formed O<sub>2</sub><sup>-</sup> ligand. Elimination of O<sub>2</sub> occurs via electron transfer from the superoxide ligand to the O<sup>-</sup> ligand, generating an O<sup>2-</sup> ligand in the [ZnO(NO<sub>2</sub>)]<sup>-</sup> product. The two pathways have similar transition state energies and neither pathway can be excluded from consideration under the experimental conditions.

#### 4.5 Zinc-Oxygen Bonding

Calculated electron configurations for the metal atom in these metal nitrate complexes can yield valuable information about the oxidation states of the metal and oxygen atoms. The nature of the metal oxide bonds that are generated by O<sup>-</sup> abstraction is analyzed using NPA calculations. Table 4.1 lists the electron configurations for the zinc atom and the orbital occupancies of unique

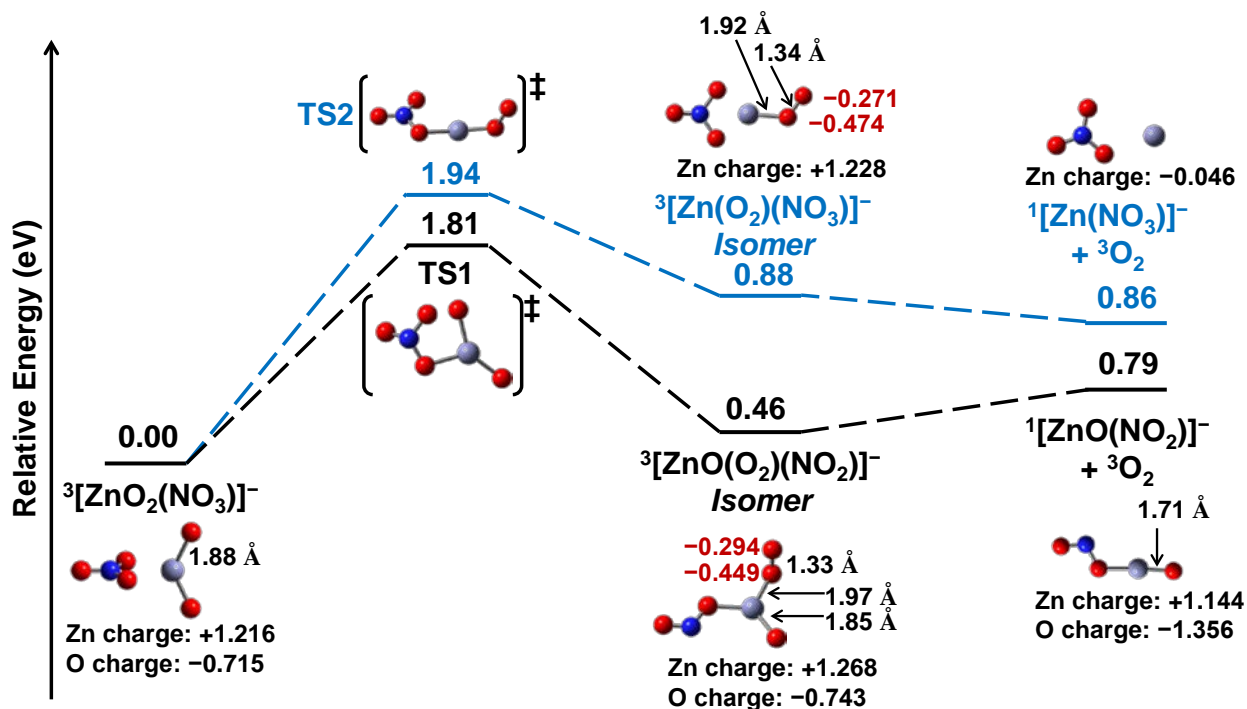


Figure 4.6 Potential energy diagram for  ${}^3\text{O}_2$  elimination from  $[\text{ZnO}_2(\text{NO}_3)]^-$ . Select bond lengths and NPA charges are indicated. Black lines indicate isomerization over the transition state barrier, TS1, via O atom transfer from the nitrate ligand to the reactive  $\text{O}^-$  ligand. Blue lines indicate isomerization over TS2 via O-O bond formation to yield an  $\text{O}_2^{\cdot-}$  ligand.

Table 4.1 Calculated electron configurations for zinc atom and orbital occupancies for unique oxygen atoms from a natural population analysis at the (U)B3LYP/6-311+G(df) level of theory.

Complex	Zinc electron configuration	Oxygen electron configuration
$[\text{Zn}(\text{NO}_3)_3]^-$	$4s^{0.35} 3d^{9.99} 4p^{0.41}$	
$[\text{ZnO}(\text{NO}_3)_2]^-$	$4s^{0.38} 3d^{9.97} 4p^{0.40}$	$2s^{1.93} 2p^{4.77}$
$[\text{ZnO}_2(\text{NO}_3)]^-$	$4s^{0.41} 3d^{9.95} 4p^{0.42}$	$2s^{1.93} 2p^{4.77}$
$[\text{ZnO}(\text{NO}_3)]^-$	$4s^{0.57} 3d^{9.92} 4p^{0.34}$	$2s^{1.92} 2p^{5.42}$
$[\text{Zn}(\text{NO}_2)(\text{NO}_3)]^-$	$4s^{0.99} 3d^{9.99} 4p^{0.38}$	
$[\text{Zn}(\text{NO}_3)]^-$	$4s^{1.95} 3d^{10.00} 4p^{0.09}$	
$[\text{ZnO}(\text{NO}_2)]^-$	$4s^{0.58} 3d^{9.92} 4p^{0.35}$	$2s^{1.92} 2p^{5.43}$

oxygen atoms for the various complexes. The precursor ion,  $[\text{Zn}(\text{NO}_3)_3]^-$ , was calculated with an electron configuration of  $4s^{0.35} 3d^{9.99} 4p^{0.41}$  and a charge of +1.228 for zinc. The calculated charge is lower than the expected +2 oxidation state due to donation of electron density from the three nitrate ligands. The zinc ion in this complex is assigned a  $3d^{10}$  electron configuration.

The zinc oxide bond of  $[\text{ZnO}(\text{NO}_3)_2]^-$  is produced via  $\text{O}^{\bullet-}$  abstraction. The metal has an electron configuration of  $4s^{0.38} 3d^{9.97} 4p^{0.40}$ , virtually unchanged from that of the precursor. These results indicate no reduction or oxidation of the metal occurs upon  $\text{O}^{\bullet-}$  abstraction. The oxygen electron configuration of  $2s^{1.93} 2p^{4.77}$  also supports the absence of a redox event upon  $\text{O}^{\bullet-}$  abstraction. The configuration is nearly identical to the expected  $2s^2 2p^5$  of a pure  $\text{O}^{\bullet-}$  ligand. The NPA charge of +1.236 for the zinc atom is not significantly different from that of the  $\text{Zn}^{2+}$  precursor, and the oxygen atom of -0.705 corresponds to an  $\text{O}^{\bullet-}$  ligand. The charge ratio, -1.75, is close to the expected oxidation state ratio of -2 ratio for the  $\text{Zn}^{2+}[\text{O}^{\bullet-}]$  ion contact pair. The unpaired electron in the doublet  $[\text{ZnO}(\text{NO}_3)_2]^-$  complex is located on the  $\text{O}^{\bullet-}$  ligand, and the zinc atom has a  $3d^{10}$  electron configuration.

Elimination of  $\text{O}_2$  from  $[\text{ZnO}(\text{NO}_3)_2]^-$  proceeds via nitrate isomerization. The  $[\text{Zn}(\text{O}_2)(\text{NO}_2)(\text{NO}_3)]^-$  isomer contains a zinc atom with +1.200 charge and an  $\text{O}_2^{\bullet-}$  ligand with an overall -0.751 charge. The  $\text{O}_2^{\bullet-}$  ligand has an O-O bond length of 1.34 Å, consistent with that of the experimentally determined distance for superoxide.<sup>17-20</sup> The  $[\text{Zn}(\text{O}_2)(\text{NO}_2)(\text{NO}_3)]^-$  intermediate eliminates  $\text{O}_2$  via electron transfer from the superoxide ligand to the metal to yield  $[\text{Zn}(\text{NO}_2)(\text{NO}_3)]^-$ . This product contains a zinc atom with the reduced charge of +0.630 and an electron configuration of  $4s^{0.99} 3d^{9.99} 4p^{0.38}$ . Both of these values indicate an increase of electron density on the zinc atom in the  $4s$  orbital. The  $\text{Zn}^+$  cation of this complex is assigned an electron configuration of  $4s^1 3d^{10}$ .

Elimination of  $\text{NO}_3^\bullet$  from the  $[\text{ZnO}(\text{NO}_3)_2]^-$  complex occurs via electron transfer from a nitrate ligand to the zinc oxide core. The product,  $[\text{ZnO}(\text{NO}_3)]^-$ , contains a zinc atom with an electron configuration of  $4s^{0.57} 3d^{9.92} 4p^{0.34}$  and +1.158 charge. The oxygen ligand has a highly reduced NPA charge of  $-1.348$  and a calculated electron configuration of  $2s^{1.92} 2p^{5.42}$ . These values indicate the oxygen atom is an  $\text{O}^{2-}$  ligand bonded to a  $\text{Zn}^{2+}$  in the neutral ZnO core of  $[\text{ZnO}(\text{NO}_3)]^-$ . The slight increase in electron density for the  $\text{Zn}(4s)$  orbital and the lower metal charge are attributed to the additional delocalization of electron density onto the metal by the highly charged  $\text{O}^{2-}$  ligand. The Zn-O bond distance is shorter, at  $1.71 \text{ \AA}$ , relative to the precursor due to the increased electrostatic attraction for the  $\text{Zn}^{2+}[\text{O}^{2-}]$  ion contact pair.

The  $[\text{ZnO}_2(\text{NO}_3)]^-$  ion is produced via  $\text{O}^{\bullet-}$  abstraction upon  $\text{NO}_2^\bullet$  loss from  $[\text{ZnO}(\text{NO}_3)_2]^-$ . The neutral  $\text{ZnO}_2$  core contains a zinc atom with an electron configuration of  $4s^{0.41} 3d^{9.95} 4p^{0.42}$  and +1.216 charge. The values are not significantly different from those of the precursor. The large O-Zn-O angle suggests the oxygen ligands contain the two unpaired electrons yielding the triplet spin ground state. The two oxygen ligands have identical occupancies of  $2s^{1.93} 2p^{4.77}$  and  $-0.715$  charges, consistent with the  $-1$  oxidation state. The core of this complex can be best described as the  $\text{Zn}^{2+}[\text{O}^{\bullet-}]_2$  neutral.

Figure 4.6 shows  $[\text{ZnO}_2(\text{NO}_3)]^-$  dissociates via  $\text{O}_2$  loss. Direct elimination of  $\text{O}_2$  requires O-O bond formation, yielding the  $[\text{Zn}(\text{O}_2)(\text{NO}_3)]^-$  isomer that contains a zinc atom with +1.228 charge. The superoxide ligand has a cumulative  $-0.745$  charge. The  $[\text{Zn}(\text{NO}_3)]^-$  ion is generated via electron transfer from the superoxide ligand to the zinc atom upon  $\text{O}_2$  loss. Table 4.1 shows the calculated electron configuration for the zinc atom in  $[\text{Zn}(\text{NO}_3)]^-$  is  $4s^{1.95} 3d^{10.00} 4p^{0.09}$ . The assignment of  $4s^2 3d^{10}$  for the electron configuration of zinc in

$[\text{Zn}(\text{NO}_3)]^-$  is expected for the neutral zinc atom of that complex. The slightly negative NPA charge for zinc of  $-0.046$  is due to minor electron density delocalization from the nitrate ligand.

A lower energy pathway for  $\text{O}_2$  loss in Figure 4.6 occurs via nitrate isomerization. The  $[\text{ZnO}(\text{O}_2)(\text{NO}_2)]^-$  intermediate contains a zinc atom with a charge of  $+1.268$  and two oxygen ligands,  $\text{O}_2^{2-}$  and  $\text{O}^-$ , with an identical  $-0.743$  charge. The zinc atom of the product ion,  $[\text{ZnO}(\text{NO}_2)]^-$ , has a calculated electron configuration of  $4s^{0.58} 3d^{9.92} 4p^{0.35}$ . The  $+1.144$  charge of zinc is slightly decreased from that of the precursor, whereas the charge of  $-1.356$  on the oxygen ligand is highly reduced. The calculated electron configuration of  $2s^{1.92} 2p^{5.43}$  for the oxygen ligand shows similar electron density as observed for the  $\text{O}^{2-}$  ligand in  $[\text{ZnO}(\text{NO}_3)]^-$ . The neutral ZnO core of  $[\text{ZnO}(\text{NO}_2)]^-$  can be described as a  $\text{Zn}^{2+}[\text{O}^{2-}]$  ion contact pair.

The MO depiction of the  $[\text{ZnO}]^+$  core in Figure 4.7 can be used to relay the electronic nature of three fragment ions in the zinc nitrate system. The first metal oxide core,  $[\text{ZnO}]^+$ , is formed via loss of  $\text{NO}_2^\bullet$  to yield  $[\text{ZnO}(\text{NO}_3)_2]^-$ . Addition of an electron via loss of  $\text{NO}_3^\bullet$  from  $[\text{ZnO}(\text{NO}_3)_2]^-$  yields the neutral ZnO core in the product,  $[\text{ZnO}(\text{NO}_3)]^-$ , with a completely filled

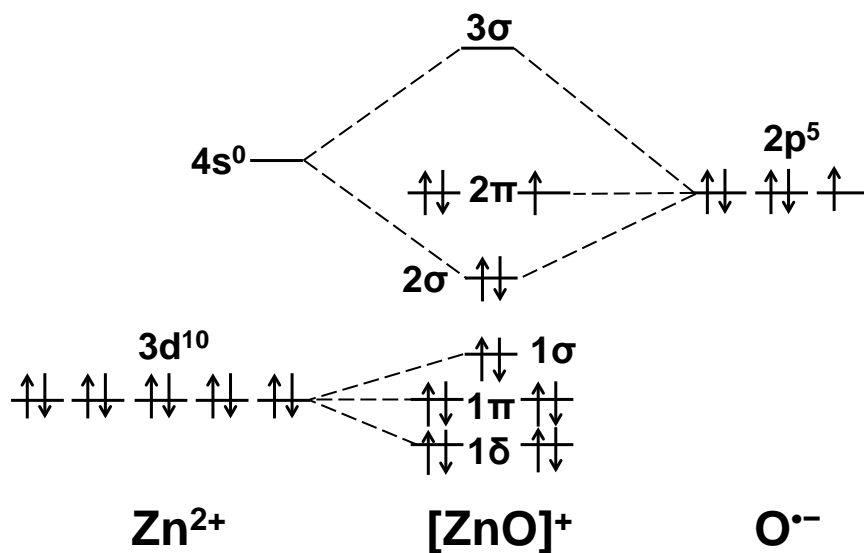


Figure 4.7 Hypothetical molecular orbital diagram for the formation of  $[\text{ZnO}]^+$  from  $\text{Zn}^{2+}$  and  $\text{O}^-$ . The relative orbital energies suggest the zinc atom is neither oxidized nor reduced upon bond formation with oxygen and the unpaired electron remains on the oxygen atom.

set of  $\pi^*$  orbitals. This neutral ZnO core can also be formed through the isomerization pathway for  $[\text{ZnO}_2(\text{NO}_3)]^-$ , shown in Figure 4.6, where elimination of  $\text{O}_2$  via electron transfer from the superoxide ligand yields  $[\text{ZnO}(\text{NO}_2)]^-$ . The singlet spin multiplicity of neutral ZnO indicates the core is closed-shell, containing no unpaired electrons. The calculated orbital occupancies show the zinc atom of the neutral ZnO core has a completely filled  $3d$  subshell and an empty  $4s$  subshell, giving zinc a  $3d^{10}$  electron configuration in these complexes. The relative energy of the  $\text{O}(2p)$  orbital of the  $\text{O}^{\bullet-}$  ligand is lower than the  $4s$  orbital of  $\text{Zn}^{2+}$ , leading to formation of the  $\text{O}^{2-}$  ligand upon elimination of  $\text{NO}_3^{\bullet}$  or  $\text{O}_2$ . The  $4s$  orbital of  $\text{Zn}^{2+}$  is not reduced upon elimination of  $\text{NO}_3^{\bullet}$  or  $\text{O}_2$  due to the presence of a lower energy electron-accepting orbital on the  $\text{O}^{\bullet-}$  ligand. The  $2p$  orbital of  $\text{O}^{\bullet-}$  is reduced to the  $-2$  oxidation state in the neutral ZnO core.

#### 4.6 Conclusions

The observed fragmentation for the zinc nitrate system is defined by the low-lying  $3d$  subshell of  $\text{Zn}^{2+}$ . Sequential  $\text{O}^{\bullet-}$  abstraction generates metal oxide cores,  $[\text{ZnO}]^+$  and neutral  $\text{ZnO}_2$ , that contain reactive oxygen radical ligands. Due to the completely filled  $3d$  subshell of the zinc atom in these cores, the lowest lying vacancies are in the  $2p$  level of the  $\text{O}^{\bullet-}$  ligands. These reactive ligands drive the observed dissociation. Reduction of the  $[\text{ZnO}]^+$  core involves electron transfer from a nitrate ligand upon  $\text{NO}_3^{\bullet}$  loss. The transferred electron spin-pairs with the radical on the  $\text{O}^{\bullet-}$  ligand, forming an  $\text{O}^{2-}$  ligand in the neutral ZnO core. The  $\text{O}^{\bullet-}$  ligand can also induce nitrate isomerization in the zinc nitrate complexes. An oxygen atom of the nitrate ligand transfers to the radical oxygen ligand, forming an  $\text{O}_2^{\bullet-}$  ligand. This radical ligand is eliminated as neutral  $\text{O}_2$  via electron transfer. The zinc nitrate system behaves similarly to those of the main group metals, aluminum and gallium.<sup>15</sup> The  $2p$  orbitals of the  $\text{O}^{\bullet-}$  ligands have the

lowest orbital vacancy in the metal oxide systems, driving ligand reduction and nitrate isomerization pathways. The zinc system does not show typical transition metal reactivity, as the *3d* subshell remains completely filled throughout all dissociation routes.

#### 4.7 References

- [1] Hester, T.H.; Goebbert, D.J. Experimental and Theoretical Study of the Decomposition of  $[\text{Zn}(\text{NO}_3)_3]^-$ . *Chem. Phys. Lett.* **2016**, In Press.
- [2] Flores-Sanchez, L.A.; Quintana-Melgoza, J.M.; Olivas, A.; Avalos-Borja, M. Reduction of Nitric Oxide by Carbon Monoxide over NiO, CuO, and ZnO Catalysts. *Reac. Kinet. Mech. and Catal.* **2015**, *114* (2), 597-609.
- [3] Anshiz, A.G.; Sokolovskii, V.D.; Borekov, G.K.; Boronin, A.I. Participation of Molecular Oxygen in the Formation of Complete Oxidation Products Via a Concerted Mechanism. *Reac. Kinet. and Catal. Lett.* **1977**, *7* (1), 87-92.
- [4] Lunkenbein, T.; Schumann, J.; Behrens, M.; Schlögl, R.; Willinger, M.G. Formation of a ZnO Overlayer in Industrial Cu/ZnO/Al<sub>2</sub>O<sub>3</sub> Catalysts Induced by Strong Metal–Support Interactions. *Angew. Chem. Int. Ed.* **2015**, *54* (15), 4544-4548.
- [5] Senanayake, S.D.; Ramírez, P.J.; Waluyo, I.; Kundu, S.; Mudiyansele, K.; Liu, Z.; Liu, Z.; Axnanda, S.; Stacchiola, D.J.; Evans, J.; *et al.* Hydrogenation of CO<sub>2</sub> to Methanol on CeO<sub>x</sub>/Cu(111) and ZnO/Cu(111) Catalysts: Role of the Metal–Oxide Interface and Importance of Ce<sup>3+</sup> Sites. *J. Phys. Chem. C.* **2016**, *120* (3), 1778-1784.
- [6] Bisio, C.; Carniato, F.; Palumbo, C.; Safronyuk, S.L.; Starodub, M.F.; Katsev, A.M.; Marchese, L.; Guidotti, M. Nanosized Inorganic Metal Oxides as Heterogeneous Catalysts for the Degradation of Chemical Warfare Agents. *Catal. Today.* **2016**, DOI: 10.1016/j.cattod.2015.12.023.
- [7] Houšková, V.; Štengl, V.; Bakardjieva, S.; Murafa, N.; Kalendová, A.; Opluštil, F. Zinc Oxide Prepared by Homogeneous Hydrolysis with Thioacetamide, Its Destruction of Warfare Agents, and Photocatalytic Activity. *J. Phys. Chem. A.* **2007**, *111* (20), 4215-4221.
- [8] Liu, B.-H.; McBriarty, M.E.; Bedzyk, M.J.; Shaikhutdinov, S.; Freund, H.-J. Structural Transformations of Zinc Oxide Layers on Pt(111). *J. Phys. Chem. C.* **2014**, *118* (49), 28725-28729.
- [9] Bridgeman, A.J.; Rothery, J. Periodic Trends in the Diatomic Monoxides and Monosulfides of the *3d* Transition Metals. *Dalton Transact.* **2000**, (2), 211-218.
- [10] Gong, Y.; Zhou, M.; Andrews, L. Spectroscopic and Theoretical Studies of Transition Metal Oxides and Dioxxygen Complexes. *Chem. Rev.* **2009**, *109* (12), 6765-6808.

- [11] Frański, R.; Sobieszczuk, K.; Gierczyk, B. Mass Spectrometric Decomposition of  $[M^{n+}(\text{NO}_3^-)_{n+1}]^-$  Anions Originating from Metal Nitrates  $M(\text{NO}_3)_n$ . *Int. J. Mass Spectrom.* **2014**, *369*, 98-104.
- [12] Li, F.; Byers, M.A.; Houk, R.S. Tandem Mass Spectrometry of Metal Nitrate Negative Ions Produced by Electrospray Ionization. *J. Am. Soc. Mass Spectrom.* **2003**, *14* (6), 671-679.
- [13] Pruitt, C.J.M.; Goebbert, D.J. Experimental and Theoretical Study of the Decomposition of Copper Nitrate Cluster Anions. *J. Phys. Chem. A.* **2015**, *119* (20), 4755-4762.
- [14] Hester, T.H.; Albury, R.M.; Pruitt, C.J.M.; Goebbert, D.J. Fragmentation of  $[\text{Ni}(\text{NO}_3)_3]^-$ : A Study of Nickel-Oxygen Bonding and Oxidation States in Nickel Oxide Fragments. *Inorg. Chem.* **2016**, *55* (13), 6634-6642.
- [15] Lightcap, J.; Hester, T.H.; Kamena, K.; Albury, R.M.; Pruitt, C.J.M.; Goebbert, D.J. Gas-Phase Fragmentation of Aluminum Oxide Nitrate Anions Driven by Reactive Oxygen Radical Ligands. *J. Phys. Chem. A.* **2016**, *120* (9), 1501-1507.
- [16] Schlöder, T.; Riedel, S., *Comprehensive Inorganic Chemistry II (Second Edition)*. Elsevier, Amsterdam, 2013, p. 227-243.
- [17] Hersleth, H.-P.; Hsiao, Y.-W.; Ryde, U.; Görbitz, C.H.; Andersson, K.K. The Crystal Structure of Peroxymyoglobin Generated through Cryoradiolytic Reduction of Myoglobin Compound III During Data Collection. *Biochem. J.* **2008**, *412* (2), 257-264.
- [18] Pedio, M.; Wu, Z.Y.; Benfatto, M.; Mascaraque, A.; Michel, E.; Ottaviani, C.; Crotti, C.; Peloi, M.; Zacchigna, M.; Comincioli, C. NEXAFS Experiment and Multiple Scattering Calculations on  $\text{KO}_2$ : Effects on the  $\pi$  Resonance in the Solid Phase. *Phys. Rev. B.* **2002**, *66* (14), 144109/144101-144109/144104.
- [19] Sawyer, D.T.; Valentine, J.S. How Super Is Superoxide? *Acc. Chem. Res.* **1981**, *14* (12), 393-400.
- [20] Unno, M.; Chen, H.; Kusama, S.; Shaik, S.; Ikeda-Saito, M. Structural Characterization of the Fleeting Ferric Peroxo Species in Myoglobin: Experiment and Theory. *J. Am. Chem. Soc.* **2007**, *129* (44), 13394-13395.

## CHAPTER 5

### NICKEL NITRATE ANION COMPLEXES

Studies of nickel nitrate anion complexes were performed and revealed a unique character in the nickel oxide bonds formed via dissociation. The nickel system was the first in our studies of metal nitrate dissociation to show the presence of a partially neutral oxygen atom within the metal oxide core. Two resonance structures for each metal oxide core,  $[\text{NiO}]^+$  and neutral NiO, captures the partial character of the oxidation states for the metal and oxygen atoms. The findings were published as a research article in 2016 in the journal *Inorganic Chemistry*.<sup>1</sup>

#### 5.1 Introduction

The  $\text{Ni}^{2+}$  cation at the core of  $[\text{Ni}(\text{NO}_3)_3]^-$  is interesting because it has triplet ground state with a  $3d^8$  configuration, and the relative  $4s$ - $3d$  splitting and energies should be similar to that of copper. The two partially filled, low energy  $3d$  orbitals of this late transition metal cation could accommodate electrons upon reduction and elimination of  $\text{NO}_3^\bullet$  similar to the reaction observed for the previously studied  $[\text{Cu}(\text{NO}_3)_3]^-$  ion.<sup>2</sup> Another metal nitrate study showed dissociation of an early transition metal nitrate complex,  $[\text{Cr}(\text{NO}_3)_4]^-$ , results in metal oxidation from +3 to +4 upon sequential  $\text{O}^\bullet$  abstraction.<sup>3</sup> Oxidation of the metal yields relatively inert  $\text{O}^{2-}$  ligands bound to the metal. The nickel system may show similarities to either of these other metal nitrate systems since it has an intermediate +2 charge along with multiple  $3d$  vacancies.

Two different nickel-oxygen bonding schemes are possible for the previously reported elimination of  $\text{NO}_2^\bullet$ .<sup>4</sup> The first involves bond formation by pairing two unpaired electrons on the

metal and oxygen radical anion, similar to the bonding in  $[\text{CrO}(\text{NO}_3)_3]^-$ .<sup>3</sup> The hypothetical  $[\text{NiO}(\text{NO}_3)_2]^-$  product would have a doublet ground state. The second bonding scheme involves mixing the O(2*p*) orbitals and empty metal 4*s* orbital, similar to the bonding in the  $[\text{CuO}(\text{NO}_3)]^-$  ion.<sup>2</sup> In this scenario, the radical of the oxygen ligand and two unpaired electrons from the metal would occupy nearly degenerate orbitals, yielding a quartet ground state in the  $[\text{NiO}(\text{NO}_3)_2]^-$  complex. As for the previous systems, the sequential dissociation, reactivity, and properties of  $[\text{NiO}(\text{NO}_3)_2]^-$  are expected to depend greatly on the electronic structure of the metal oxide core. Theoretical calculations are compared with experimental energy measurements to better understand the metal-oxygen bonding within  $[\text{NiO}(\text{NO}_3)_2]^-$  and its fragments.

## 5.2 Methods

A solution with 1 mM concentration was prepared by dissolving a sample of nickel nitrate hexahydrate (0.029 g, 98%, Alfa Aesar), purchased from VWR International (Randor, PA, USA), in a mixture of HPLC grade solvents, methanol (50 mL) and acetonitrile (50 mL). The TSQ-7000 tandem mass spectrometer (Finnigan MAT, San Jose, CA) was used to perform CID and ERMS experiments. Authentic product ions were generated using in-source fragmentation for in-depth dissociation studies.

Density functional calculations were performed using the (U)B3LYP functional and the 6-311G+(3df) basis set. The lowest energy structures, with correct spin-states, were determined using a standard approach involving geometry optimization, followed by determination of the lowest energy structures for the product ions. Natural population analysis, NPA, calculations were performed on the optimized structures to determine the electron configurations, spin densities, and atomic charges of the metal and oxygen ligands.

### 5.3 Experimental Results

Electrospray ionization, ESI, was used to generate gas-phase nickel nitrate anion complexes.

Figure 5.1 shows a Q1MS spectrum with an isotopic distribution of peaks for  $[\text{Ni}(\text{NO}_3)_3]^-$ , a set of peaks for  $[\text{NiO}(\text{NO}_3)_2]^-$ , and peaks for  $[\text{H}(\text{NO}_3)_2]^-$  and  $\text{NO}_3^-$ . The  $[\text{Ni}(\text{NO}_3)_3]^-$  complex at  $m/z$  244 was chosen as the precursor due to the higher relative abundance of the  $^{58}\text{Ni}$  isotope. This complex was subjected to CID and yielded the fragments shown in Figure 5.2A. Peaks corresponding to the sequential loss of  $\text{NO}_2^\bullet$  were observed, along with other low intensity peaks. The spectrum in Figure 5.2A agrees with a previously published study using a Q-TOF mass spectrometer, with slight variation in relative peak intensity for the different instrumental setups and dissociation energies.<sup>4</sup>

Figure 5.2B shows the CID spectrum for  $[\text{NiO}(\text{NO}_3)_2]^-$ . This intermediate was generated via in-source fragmentation, detailed in Chapter 2. All of the nickel-containing fragments in

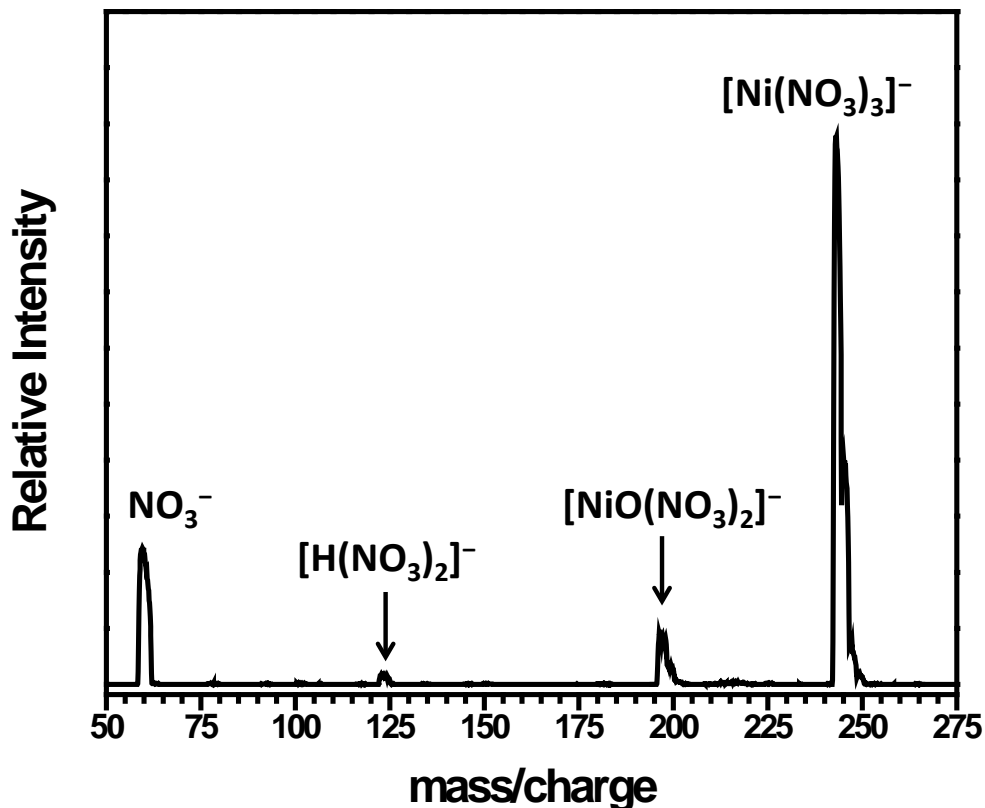


Figure 5.1 Representative Q1MS spectrum of nickel nitrate solution.

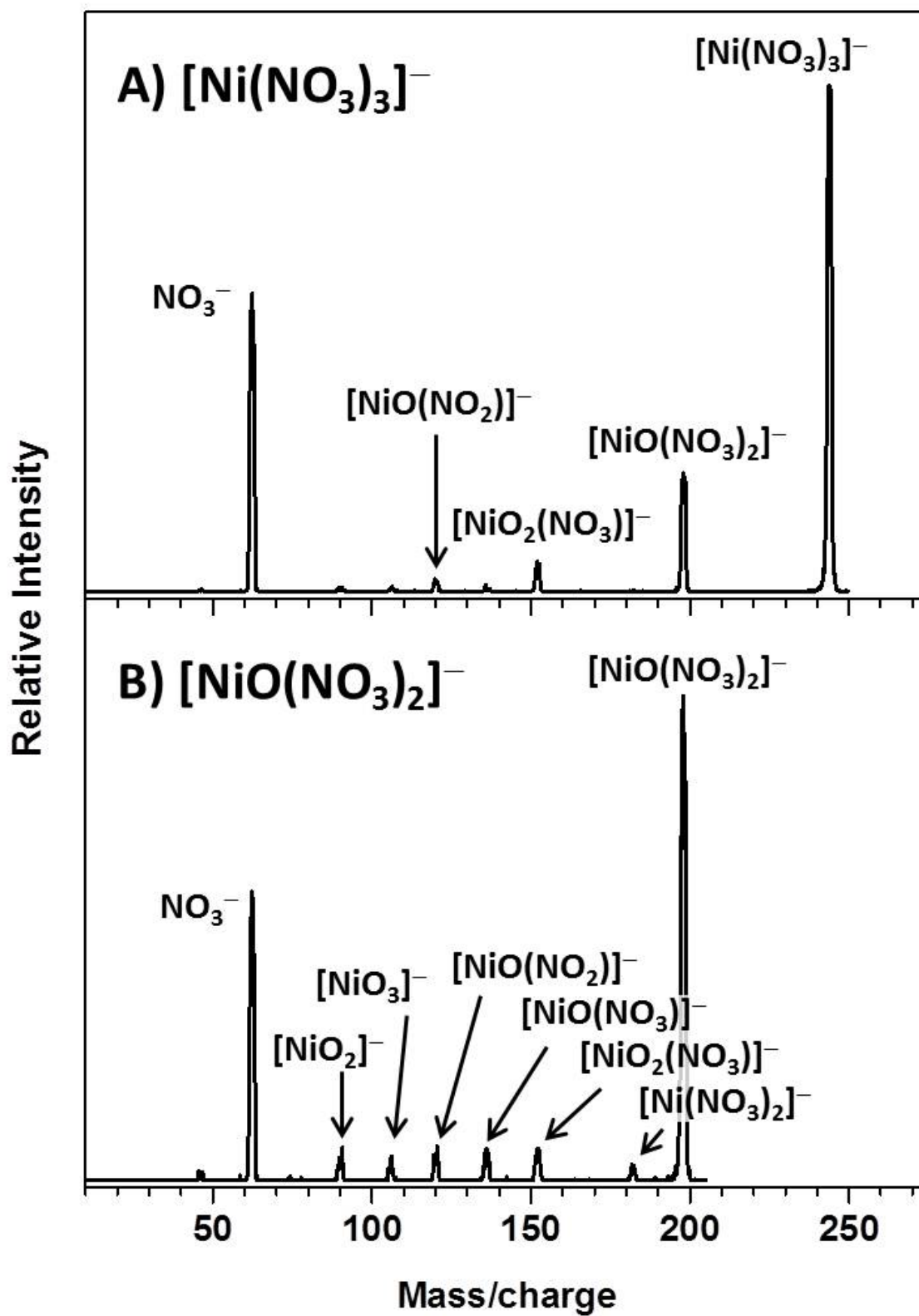


Figure 5.2 CID mass spectra of (A)  $[\text{Ni}(\text{NO}_3)_3]^-$  and (B)  $[\text{NiO}(\text{NO}_3)_2]^-$  recorded at 40 eV<sub>lab</sub> with 0.50 mTorr of Ar collision gas.

Figure 5.2A are sequential dissociation products of the  $[\text{NiO}(\text{NO}_3)_2]^-$  intermediate. Figure 5.2B contains peaks corresponding to the elimination of  $\text{NO}_2^\bullet$  and  $\text{NO}_3^\bullet$  from  $[\text{NiO}(\text{NO}_3)_2]^-$ , respectively labeled as  $[\text{NiO}_2(\text{NO}_3)]^-$  and  $[\text{NiO}(\text{NO}_3)]^-$ . A very low intensity fragment,  $[\text{Ni}(\text{NO}_3)_2]^-$ , corresponds to O atom loss from  $[\text{NiO}(\text{NO}_3)_2]^-$ . The products labeled as  $[\text{NiO}(\text{NO}_2)]^-$ ,  $[\text{NiO}_3]^-$ , and  $[\text{NiO}_2]^-$  are sequential products from  $[\text{NiO}_2(\text{NO}_3)]^-$  via  $\text{O}_2$ ,  $\text{NO}_2^\bullet$ , and  $\text{NO}_3^\bullet$  elimination respectively. The irregular formula for the  $\text{O}_2$  loss product ion,  $[\text{NiO}(\text{NO}_2)]^-$ , will be discussed in the next section.

Energy-dependent CID spectra were recorded for the two precursors in this study,  $[\text{Ni}(\text{NO}_3)_3]^-$  and  $[\text{NiO}(\text{NO}_3)_2]^-$ . The relative intensities of all fragments are plotted as a function of the center-of-mass collision energy. Figure 5.3A shows a representative ERMS spectrum for the product ions of  $[\text{Ni}(\text{NO}_3)_3]^-$ . Elimination of  $\text{NO}_2^\bullet$  and loss of nitrate anion occur with an onset around 1.5 eV in Figure 5.3A, indicating the dissociation reactions for these processes should have similar energies. The high relative intensity of the  $[\text{NiO}(\text{NO}_3)_2]^-$  fragment in Figure 5.3A at low collision voltages and pressures suggests the intense  $\text{NO}_3^-$  signal in the CID spectrum of  $[\text{Ni}(\text{NO}_3)_3]^-$  is primarily due to nitrate loss from secondary products. The other ions in the ERMS spectrum have higher energy onsets, at about 2.5 and 3 eV, and are secondary products of  $[\text{NiO}(\text{NO}_3)_2]^-$  dissociation, as shown in Figure 5.2B and Figure 5.3B.

The ERMS spectrum for  $[\text{NiO}(\text{NO}_3)_2]^-$  dissociation is shown in Figure 5.3B. Elimination of  $\text{NO}_2^\bullet$  occurs with a low onset, at around 1 eV. The intensity profile of the product,  $[\text{NiO}_2(\text{NO}_3)]^-$ , shows sequential dissociation behavior. A sharp increase in intensity is observed at around 1 eV as the ion is initially detected, followed by a gradual decrease from the maximum at around 4 eV as sequential fragmentation becomes dominant. Sequential loss of  $\text{O}_2$  from  $[\text{NiO}_2(\text{NO}_3)]^-$  occurs with a relatively low onset around 2 eV. This low energy onset means the

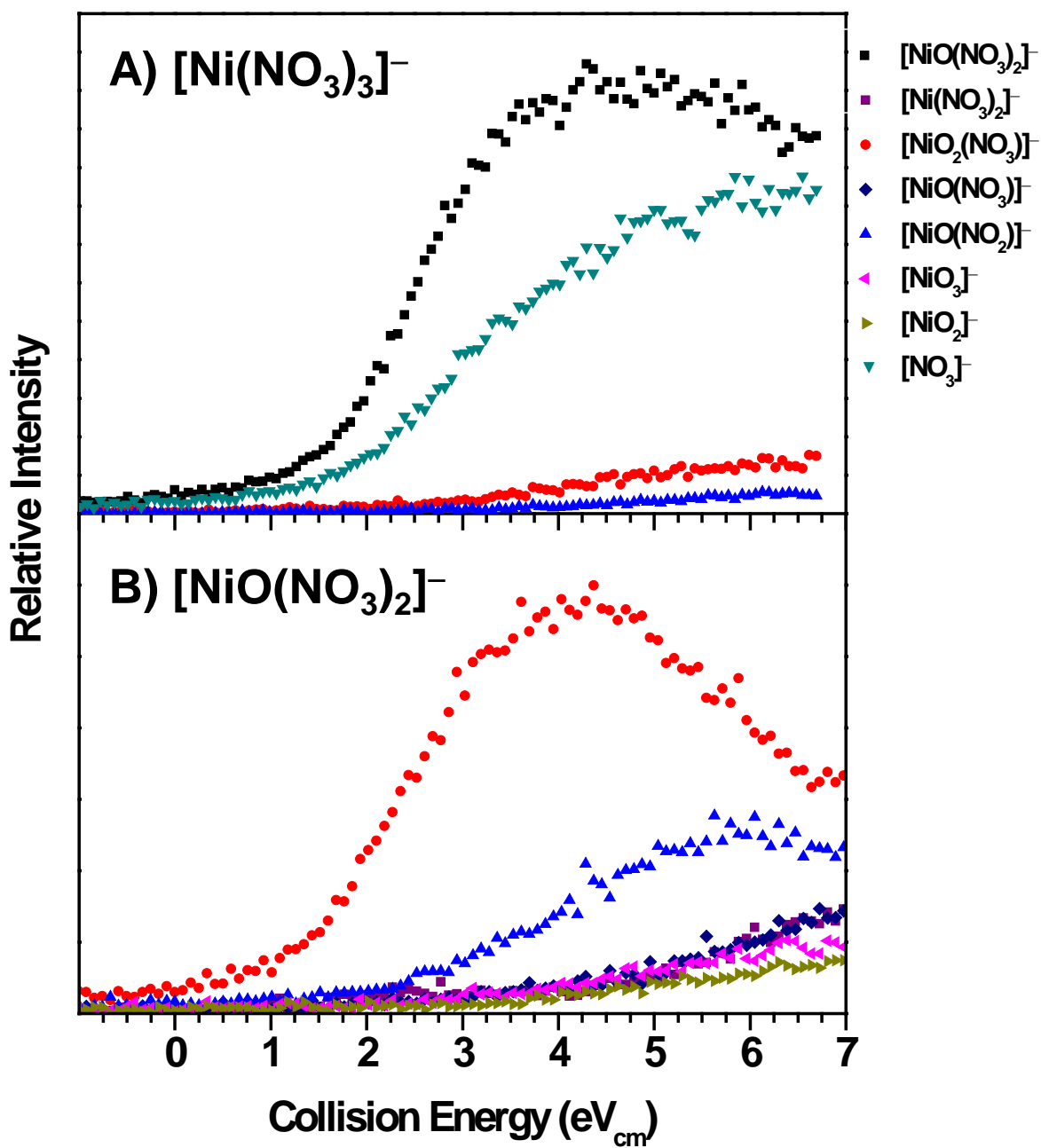


Figure 5.3 Energy-dependent fragmentation spectra of (A) [Ni(NO<sub>3</sub>)<sub>3</sub>]<sup>-</sup> and (B) [NiO(NO<sub>3</sub>)<sub>2</sub>]<sup>-</sup>.

pathway for elimination of  $\text{NO}_2^\bullet$ , followed by  $\text{O}_2$  loss, is lower in energy than the direct elimination of  $\text{NO}_3^\bullet$  from  $[\text{NiO}(\text{NO}_3)_2]^-$ . The primary dissociation routes for elimination of  $\text{NO}_3^\bullet$  and O atom have onsets between 3 and 4 eV and the ERMS curves are overlaid. The sequential losses of  $\text{O}_2$ ,  $\text{NO}_2^\bullet$ , and  $\text{NO}_3^\bullet$  from  $[\text{NiO}_2(\text{NO}_3)]^-$  also occur at higher energy, with onsets between 3 and 4 eV.

#### 5.4 Theoretical Results

Calculations were performed on the precursor ion and all observed products. Optimized structures of the nickel-containing ions are shown in the dissociation pathways, Figure 5.4 and Figure 5.5. Selected geometric parameters are provided for each structure, including distances for nitrate oxygen-metal coordination  $R_{\text{avg}}(\text{Ni-O})$  and for unique Ni-O and O-O bonds.

Figure 5.4 shows the  $[\text{Ni}(\text{NO}_3)_3]^-$  precursor contains a nickel cation surrounded by three nitrate ligands in a  $C_3$ -symmetric arrangement. The nitrate ligands are each coordinated to the metal through two oxygen atoms and are slightly rotated out of the plane defined by the nickel and nitrogen atoms. The  $\text{NO}_2^\bullet$  elimination reaction for  $[\text{Ni}(\text{NO}_3)_3]^-$  was calculated at 2.76 eV, similar to the 2.70 eV required for  $\text{NO}_3^-$  loss. These calculated energies coincide with the appearance energies for these processes, extrapolated at around 1.5 eV. The experimental energies are lower than the calculated energies due to excess internal energy of the ions, but the energy trends are strongly matched.

The  $[\text{NiO}(\text{NO}_3)_2]^-$  complex that forms via  $\text{O}^-$  abstraction has a structure similar to that of the precursor ion, with approximately  $C_2$  symmetry. The nickel atom is coordinated to each nitrate ligand in a bidentate manner. The nickel-oxygen bond distance was calculated at 1.74 Å.

Figure 5.4 shows the calculated energy for the second  $\text{NO}_2^\bullet$  loss is 2.49 eV, slightly lower than the first loss. The experimental appearance energies for  $\text{NO}_2^\bullet$  loss from  $[\text{Ni}(\text{NO}_3)_3]^-$  and  $[\text{NiO}(\text{NO}_3)_2]^-$  also showed lower energy for the second  $\text{NO}_2^\bullet$  loss. The structure of the product ion,  $[\text{NiO}_2(\text{NO}_3)]^-$ , shows a bidentate nitrate ligand coordinated to a core with two Ni-O bonds of equal distance, 1.70 Å.

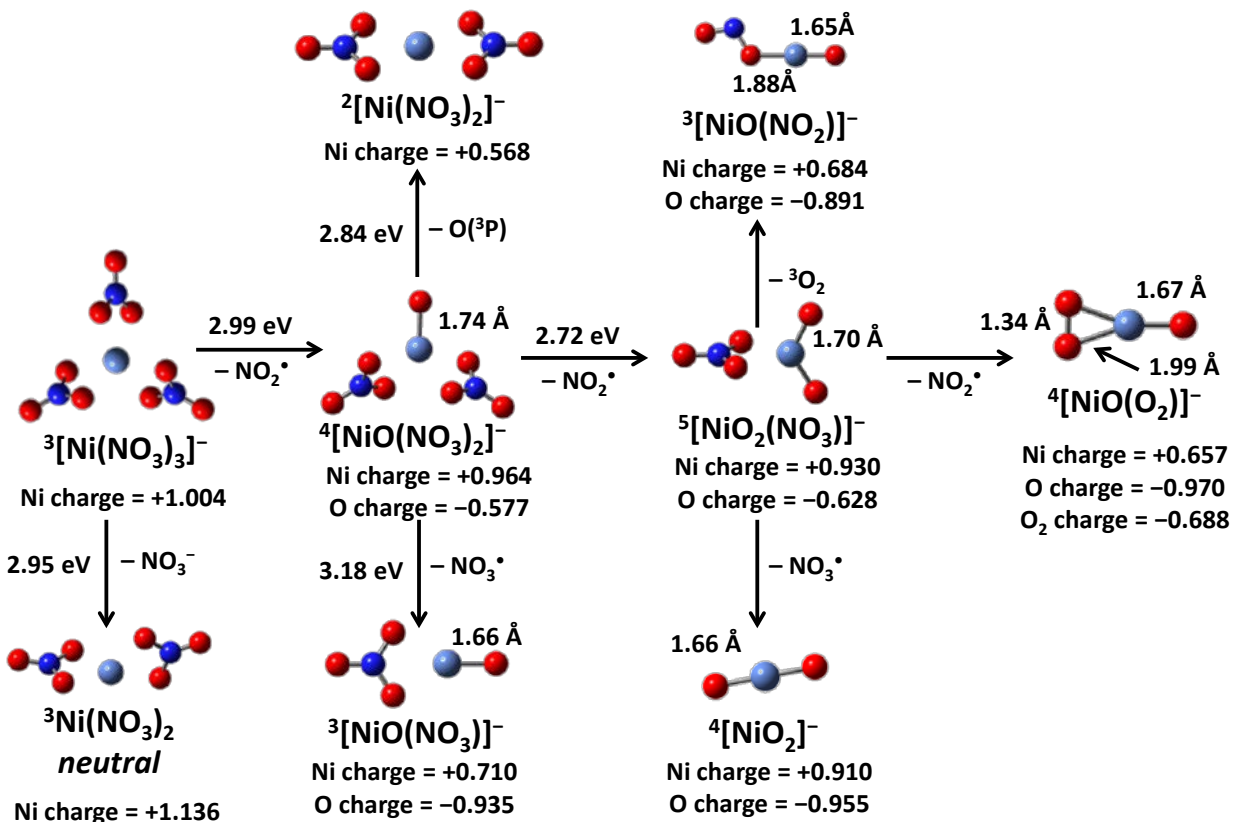


Figure 5.4 Calculated relative energy differences for the decomposition of  $[\text{Ni}(\text{NO}_3)_3]^-$  at the (U)B3LYP/6-311+G(3df) level of theory. All energies include zero-point corrections. Select bond lengths and charges for the metal and unique oxygen atoms are indicated. Atom colors: teal for nickel, blue for nitrogen, and red for oxygen.

The loss of  $\text{NO}_3^\bullet$  from  $[\text{NiO}(\text{NO}_3)_2]^-$  was calculated to occur at 2.84 eV, nearly identical to the 2.83 eV calculated for the elimination of O atom. The ERMS curves for these two processes were notably overlaid with an identical, high energy onset and similar intensities over the entire collision energy range. The  $[\text{NiO}(\text{NO}_3)]^-$  fragment has  $\text{C}_2$  symmetry with a bidentate nitrate ligand defining the mirror plane. The Ni-O bond distance of 1.66 Å is shorter than the

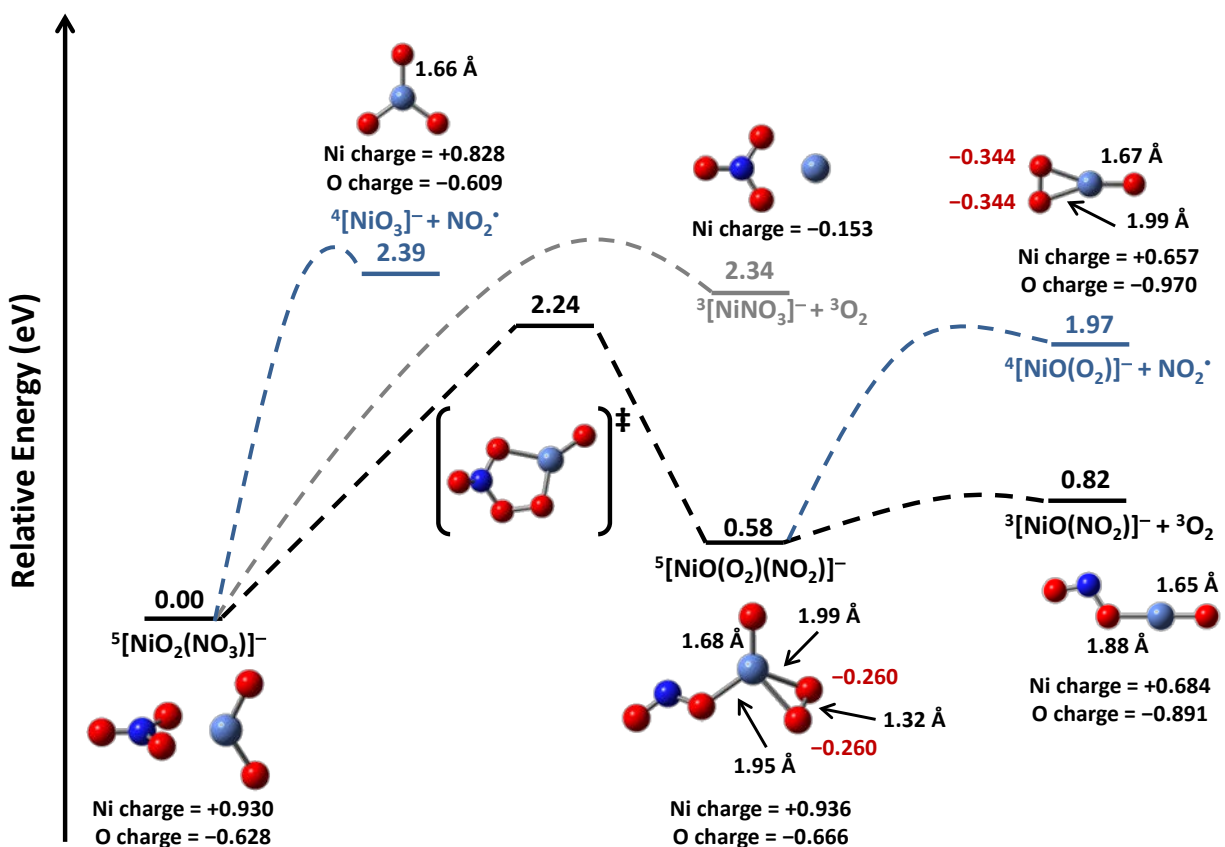


Figure 5.5 Potential energy diagram for decomposition of  $[\text{NiO}_2(\text{NO}_3)]^-$ . Color description: black and gray dashes = elimination of  $\text{O}_2$ ; blue dashes = elimination of  $\text{NO}_2^\bullet$ .

1.76 Å of the precursor. The shorter bond distance is attributed to lower electrostatic attraction in the metal oxide core due to the transfer of an electron upon elimination of  $\text{NO}_3^\bullet$ .

Figure 5.4 shows a third elimination reaction,  $[\text{NiO}(\text{NO}_3)_2]^- \rightarrow [\text{Ni}(\text{NO}_3)_2]^- + \text{O}$ , for the  $[\text{NiO}(\text{NO}_3)_2]^-$  ion. The product ion contains a nickel cation coordinated on opposite sides by two bidentate nitrate ligands. The nickel cation is necessarily reduced to  $\text{Ni}^+$  by electron transfer from the oxygen ligand upon O atom elimination.

Figure 5.5 follows the dissociation of  $[\text{NiO}_2(\text{NO}_3)]^-$  using a potential energy diagram. The products of direct  $\text{NO}_2^\bullet$  and  $\text{O}_2$  loss are shown with blue and gray lines at 2.39 and 2.34 eV, respectively. A ligand isomerization pathway, shown with black lines, can lead to lower energy losses of  $\text{NO}_2^\bullet$  and  $\text{O}_2$ . The nitrate ligand of  $[\text{NiO}_2(\text{NO}_3)]^-$  transfers an O atom to the radical

oxygen ligand over a 2.24 eV transition state barrier to form the  $[\text{NiO}(\text{O}_2)(\text{NO}_2)]^-$  intermediate. The transferred O atom partially oxidizes the  $\text{O}^{\bullet-}$  ligand to form the superoxide,  $\text{O}_2^{\bullet-}$ , ligand, confirmed by the calculated O-O bond distance of 1.32 Å that is close to that measured experimentally for superoxide.<sup>5-8</sup>

Figure 5.5 shows the  $[\text{NiO}(\text{O}_2)(\text{NO}_2)]^-$  isomer can eliminate  $\text{O}_2$  or  $\text{NO}_2^{\bullet}$  to yield the low energy products,  $[\text{NiO}(\text{NO}_2)]^-$  at 0.82 eV and  $[\text{ONi}(\text{O}_2)]^-$  at 1.97 eV, respectively. The low energy ERMS onsets for these fragments support the lower energy isomerization pathway at the bottom of Figure 5.5.

### 5.5 Nickel-Oxygen Bonding

The nature of the metal oxide bonds in the nickel complexes was analyzed using NPA calculations. Electron configurations for the nickel atom and the orbital occupancies of the metal and oxygen atoms were considered and are given in Table 5.1. The precursor ion,  $[\text{Ni}(\text{NO}_3)_3]^-$ , was calculated to have a charge of +1.004 and an electron configuration of  $4s^{0.27} 3d^{8.30} 4p^{0.41}$  for nickel. The metal in this complex is in the +2 oxidation state with an assigned  $3d^8$  electron configuration. An alternate view of  $3d$  orbital occupancy can use the overall difference in  $\alpha$ - and  $\beta$ -electron spin, given as  $\text{net}(\alpha - \beta)$  in Table 5.2. This  $\text{net}(\alpha - \beta)$  value accounts for excess electron spin on the metal, in a similar way to the provided Mulliken spin value. These two measures of spin density complement one another in determining the placement of unpaired electrons. The nickel atom in  $[\text{Ni}(\text{NO}_3)_3]^-$ , was calculated to have a  $\text{net}(\alpha - \beta)$  of  $1.66\alpha$  and a Mulliken spin of  $1.70\alpha$  for Ni. These values indicate the metal has a  $3d^8$  electron configuration.

The nickel oxide bond of  $[\text{NiO}(\text{NO}_3)_2]^-$  is produced via  $\text{O}^{\bullet-}$  abstraction by the metal. The calculated electron configuration of  $4s^{0.29} 3d^{8.34} 4p^{0.40}$  corresponds to a  $3d^8$  Ni. The excess

Table 5.1 Calculated electron configurations for nickel from a natural population analysis at the (U)B3LYP/6-311+G(3df) level of theory.

Complex	Nickel electron configuration
$^3[\text{Ni}(\text{NO}_3)_3]^-$	$4s^{0.27} 3d^{8.30} 4p^{0.41}$
$^4[\text{NiO}(\text{NO}_3)_2]^-$	$4s^{0.29} 3d^{8.34} 4p^{0.40}$
$^2[\text{Ni}(\text{NO}_3)_2]^-$	$4s^{0.35} 3d^{8.91} 4p^{0.16}$
$^5[\text{NiO}_2(\text{NO}_3)]^-$	$4s^{0.29} 3d^{8.30} 4p^{0.47}$
$^5[\text{NiO}(\text{O}_2)(\text{NO}_2)]^-$	$4s^{0.29} 3d^{8.38} 4p^{0.37}$
$^3[\text{NiO}(\text{NO}_2)]^-$	$4s^{0.59} 3d^{8.55} 4p^{0.16}$
$^3[\text{NiO}(\text{NO}_3)]^-$	$4s^{0.48} 3d^{8.59} 4p^{0.20}$

electron spin was calculated as a net( $\alpha - \beta$ ) of  $1.60\alpha$  and a Mulliken spin of  $1.64\alpha$  for Ni. The metal electron configuration and excess spin values do not show noticeable reduction or oxidation of nickel upon  $\text{O}^{\bullet-}$  abstraction. A closer look at the oxygen Mulliken spin of  $1.17\alpha$  and the calculated O( $2p$ ) occupancy, with  $2.92 \alpha$ -density and  $1.74 \beta$ -density, shows a significant lack of electron density for the oxygen atom. An NPA calculation of the isolated  $[\text{NiO}]^+$  core was performed to exclude any contribution that electron donation from the ligands has on the electronic picture. These calculations show an O( $2p$ ) occupancy with  $2.92 \alpha$ -density and  $1.31 \beta$ -density, corresponding to an occupancy close to the  $2p^4$  occupancy of neutral O atom. The experimentally observed loss of O atom from this complex supports the description of the core as having  $\text{Ni}^+[\text{O}]$  character. The lowered NPA charge of  $+0.964$  for Ni reflects the partial  $+1$  character of nickel. The  $[\text{NiO}]^+$  core can be described primarily with the  $\text{Ni}^{2+}[\text{O}^{\bullet-}]$  resonance structure, with a smaller contribution of the  $\text{Ni}^+[\text{O}]$  resonance structure. An adequate description of the electronic nature of the atoms in the core includes both resonance structures, but assigned  $3d^8$  configuration for the nickel atom defines the main character of the metal in  $[\text{NiO}(\text{NO}_3)_2]^-$ .

Elimination of neutral O atom from  $[\text{NiO}(\text{NO}_3)_2]^-$  occurs via electron transfer to the  $3d$  subshell of nickel. Table 5.1 shows an extremely high  $3d$  occupancy in the electron

Table 5.2 Calculated nickel 3*d* spin density and atomic properties for nickel and oxygen from a natural population analysis at the (U)B3LYP/6-311+G(3df) level of theory.

Complex	Ni(3 <i>d</i> ) Net $\alpha$ - $\beta$	Mulliken spin		NPA charge		Occupancy	
		Ni	O	Ni	O	Assigned	Calculated
						Ni(3 <i>d</i> )	O(2 <i>p</i> )
<sup>3</sup> [Ni(NO <sub>3</sub> ) <sub>3</sub> ] <sup>-</sup>	1.66 $\alpha$	1.70 $\alpha$		+0.976		8	
<sup>4</sup> [NiO(NO <sub>3</sub> ) <sub>2</sub> ] <sup>-</sup>	1.60 $\alpha$	1.64 $\alpha$	1.17 $\alpha$	+0.964	-0.577	8	2.92 $\alpha$ , 1.74 $\beta$
<sup>4</sup> [NiO] <sup>+</sup>	1.31 $\alpha$	1.44 $\alpha$	1.56 $\alpha$	+1.227	-0.227	8	2.92 $\alpha$ , 1.31 $\beta$
<sup>5</sup> [NiO <sub>2</sub> (NO <sub>3</sub> )] <sup>-</sup>	1.63 $\alpha$	1.66 $\alpha$	1.11 $\alpha$	+0.930	-0.628	8	2.93 $\alpha$ , 1.79 $\beta$
<sup>3</sup> [NiO(NO <sub>2</sub> )] <sup>-</sup>	1.22 $\alpha$	1.22 $\alpha$	0.75 $\alpha$	+0.684	-0.891	8.5	2.87 $\alpha$ , 2.10 $\beta$
<sup>3</sup> [NiO(NO <sub>3</sub> )] <sup>-</sup>	1.25 $\alpha$	1.23 $\alpha$	0.72 $\alpha$	+0.710	-0.935	8.5	2.87 $\alpha$ , 2.14 $\beta$

configuration of nickel in the [Ni(NO<sub>3</sub>)<sub>2</sub>]<sup>-</sup> complex. The doublet multiplicity for the complex supports the assignment of 3*d*<sup>9</sup> for the electron configuration of nickel in [Ni(NO<sub>3</sub>)<sub>2</sub>]<sup>-</sup>. This assignment correlates with the reduced NPA charge of +0.568 for nickel Table 5.2.

The sequential loss of NO<sub>2</sub><sup>•</sup> produces a complex, [NiO<sub>2</sub>(NO<sub>3</sub>)]<sup>-</sup>, with a neutral NiO<sub>2</sub> core. This core contains a nickel atom with the 4s<sup>0.29</sup> 3d<sup>8.30</sup> 4p<sup>0.47</sup> configuration, a net( $\alpha - \beta$ ) of 1.63 $\alpha$ , and a value of 1.66 $\alpha$  for Mulliken spin. These values are virtually identical to those of the precursor, indicating no change in the metal oxidation state. The O Mulliken spins are both 1.11 $\alpha$  and the O(2*p*) occupancies show an identical 2.92  $\alpha$ -density and 1.79  $\beta$ -density. These O(2*p*) occupancies correspond to a slight donation of  $\beta$ -density to the metal. The oxygen ligands of the bare neutral NiO<sub>2</sub> core have O(2*p*) occupancies with 2.89  $\alpha$ -density and 1.67  $\beta$ -density, indicating the nitrate ligands donate very little electron density to the neutral core. The effect is not significant enough to alter the oxidation state assignment. The respective nickel and oxygen charges of +0.930 and -0.628 for the [NiO<sub>2</sub>(NO<sub>3</sub>)]<sup>-</sup> ion, the nickel electron configuration, and the excess electron spin values indicate Ni has the +2 oxidation state and a 3*d*<sup>8</sup> configuration.

The last two complexes listed in Table 5.1 contain neutral NiO cores. The moderately high 3*d* occupancy for these complexes shows increased electron density on the metal. The

$[\text{NiO}(\text{NO}_2)]^-$  complex is generated via  $\text{O}_2$  loss from the intermediate,  $[\text{NiO}(\text{O}_2)(\text{NO}_2)]^-$ . The  $[\text{NiO}(\text{NO}_3)]^-$  complex is generated via  $\text{NO}_3^\bullet$  loss from  $[\text{NiO}(\text{NO}_3)_2]^-$ . Both products form via electron transfer upon dissociation. The electron configuration for nickel in  $[\text{NiO}(\text{NO}_2)]^-$  is  $4s^{0.59} 3d^{8.55} 4p^{0.16}$ , with a net( $\alpha - \beta$ ) of  $1.22\alpha$  and a Mulliken spin of  $1.22\alpha$  for Ni. The values for  $[\text{NiO}(\text{NO}_3)]^-$  are very similar, with an electron configuration of  $4s^{0.48} 3d^{8.59} 4p^{0.20}$ , a net( $\alpha - \beta$ ) of  $1.25\alpha$  and a Mulliken spin of  $1.23\alpha$  for Ni. Both sets of metal occupancies and excess spin values show partial reduction of the nickel upon elimination of  $\text{O}_2$  or  $\text{NO}_3^\bullet$ .

The  $\text{O}(2p)$  occupancies for  $[\text{NiO}(\text{NO}_2)]^-$  and  $[\text{NiO}(\text{NO}_3)]^-$  are given in Table 5.2 and show more electron density on the oxygen ligands than in the complexes with  $\text{O}^\bullet$  ligands. The effect of additional electron density is shown on both atoms of the neutral NiO core, with NPA charges in  $[\text{NiO}(\text{NO}_2)]^-$  differing from that of the precursor by  $-0.252$  for the nickel atom and  $-0.225$  for the oxygen atom. These factors coincide with partial reduction of both atoms in the metal oxide core via electron transfer upon  $\text{O}_2$  loss from  $[\text{NiO}(\text{O}_2)(\text{NO}_2)]^-$ . An analogous reduction event occurs for the elimination of  $\text{NO}_3^\bullet$  from  $[\text{NiO}(\text{NO}_3)_2]^-$  to form the neutral NiO core. The electron transfer from a nitrate ligand to the core leads to partial reduction of both atoms of the core. The calculated NPA charges in  $[\text{NiO}(\text{NO}_3)]^-$  differ from those of the precursor by  $-0.254$  for the nickel atom and  $-0.358$  for the oxygen atom. The calculated electron configuration, orbital occupancies, excess spin accounting, and atomic charges indicate the nickel atom should be assigned a  $3d^{8.5}$  electron configuration for both complexes,  $[\text{NiO}(\text{NO}_2)]^-$  and  $[\text{NiO}(\text{NO}_3)]^-$ . The metal and oxygen atoms are considered to have non-integer oxidation states of  $+1.5$  and  $-1.5$ , respectively. The two major resonance structures that contribute to the overall picture of the neutral metal oxide core are  $\text{Ni}^{2+}[\text{O}^{2-}]$  and  $\text{Ni}^+[\text{O}^\bullet]$ . The

first resonance structure explicitly accounts for the calculated high excess spin on the metal, whereas the second accounts for the high electron density on the oxygen.

The nickel oxide bond can be further analyzed using a simple MO diagram for the interaction of the  $3d^8$   $\text{Ni}^{2+}$  and  $\text{O}^{\cdot-}$  ion pair, Figure 5.6. The Ni-O bond of the  $[\text{NiO}]^+$  core in  $[\text{NiO}(\text{NO}_3)_2]^-$  is formed by atomic orbital mixing as depicted. The result is a quartet  $[\text{NiO}]^+$  core with 2 unpaired electrons in the  $\pi^*$  (labeled as  $2\pi$ ) orbitals and 1 unpaired electron in the  $\sigma^*$  (labeled as  $2\sigma$ ) orbital. The  $\text{Ni}^{2+}$  and  $\text{O}^{\cdot-}$  atomic orbital levels are shown as similar in energy for the high spin core. The  $3d$  orbitals are placed slightly lower in energy to reflect the partial donation of electron density from the higher energy  $\text{O}^{\cdot-}$  orbitals to the metal, given the minor influence of the  $\text{Ni}^+[\text{O}]$  resonance structure.

This MO depiction can be used for three different fragment ions in the nickel nitrate system. The first use has been shown for the metal oxide core of  $[\text{NiO}(\text{NO}_3)_2]^-$ . No modifications of the diagram in Figure 5.6 are necessary to represent this core. Addition of an electron via loss of  $\text{NO}_3^{\cdot}$  from  $[\text{NiO}(\text{NO}_3)_2]^-$  yields the neutral NiO core in the product,  $[\text{NiO}(\text{NO}_3)]^-$ . The same neutral NiO core can be formed upon elimination of  $\text{O}_2$  via electron

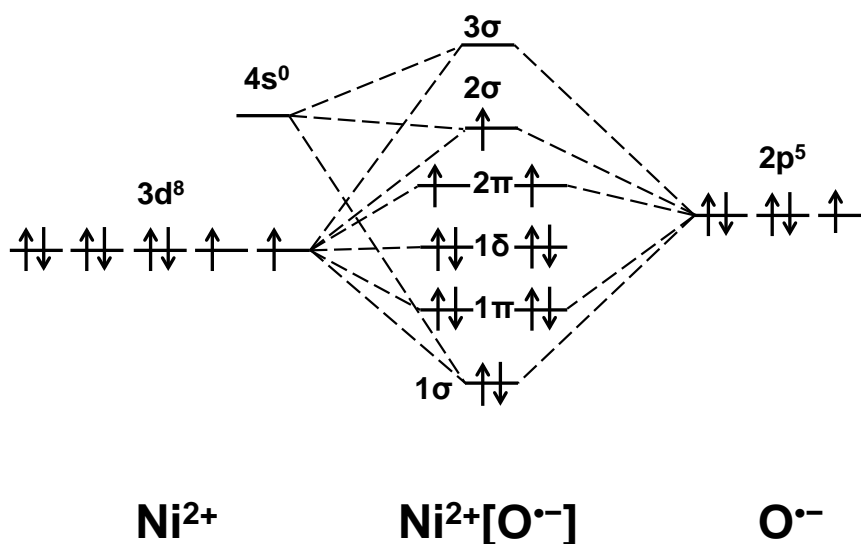


Figure 5.6 Hypothetical zero-order orbital interaction diagram illustrating the formation of  $[\text{NiO}]^+$  from  $\text{Ni}^{2+}$  and  $\text{O}^{\cdot-}$ .

transfer from the superoxide ligand in the  $[\text{NiO}(\text{O}_2)(\text{NO}_2)]^-$  isomer to yield  $[\text{NiO}(\text{NO}_2)]^-$ . This core has triplet multiplicity and contains an unpaired electron in the  $\pi^*$  orbital and another in the  $\sigma^*$  orbital. The calculated orbital occupancies and excess electron spin values show the neutral NiO core has an equally shared electron, between the nickel and oxygen atoms, that gives nickel a  $3d^{8.5}$  electron configuration in these complexes.

### 5.6 Conclusions

The dissociation characteristics of nickel oxide nitrate anions are determined by the  $3d$  energy level of the nickel cation and the  $2p$  level of the oxygen ligand. Large differences in valence orbital energies lead to the integer assignment of metal oxidation state upon dissociation, whereas smaller relative energy differences result in non-integer metal oxidation states due to electron delocalization in the metal oxide bond. The  $[\text{NiO}]^+$  core is formed by the mixing of atomic valence orbitals with comparable energy levels. The result is slight delocalization of oxygen electron density to the metal in the  $[\text{NiO}]^+$  core. The nearly degenerate levels also lead to the emergence of highly covalent character for the extra electron in the neutral NiO core.

Nickel oxide nitrate complexes undergo nitrate isomerization to eliminate  $\text{O}_2$  and  $\text{NO}_2^\bullet$  via oxygen atom transfer from a nitrate to a reactive  $\text{O}^\bullet$  ligand. The experimental appearance energies indicate  $[\text{NiO}_2(\text{NO}_3)]^-$  undergoes  $\text{O}_2$  loss along a low energy nitrate isomerization surface, whereas  $\text{NO}_3^\bullet$  and O atom loss are expected to occur at much higher energies. The relatively high appearance energy for elimination of  $\text{NO}_2^\bullet$  from  $[\text{NiO}_2(\text{NO}_3)]^-$  suggests the loss along the isomerization pathway cannot compete efficiently with  $\text{O}_2$  loss. The relative low intensity for the peak corresponding to O atom loss in the CID spectrum of  $[\text{NiO}(\text{NO}_3)_2]^-$  is a result of the minor neutral character on oxygen in the  $[\text{NiO}]^+$  core.

## 5.7 References

- [1] Hester, T.H.; Albury, R.M.; Pruitt, C.J.M.; Goebbert, D.J. Fragmentation of  $[\text{Ni}(\text{NO}_3)_3]^-$ : A Study of Nickel-Oxygen Bonding and Oxidation States in Nickel Oxide Fragments. *Inorg. Chem.* **2016**, *55* (13), 6634-6642.
- [2] Pruitt, C.J.M.; Goebbert, D.J. Experimental and Theoretical Study of the Decomposition of Copper Nitrate Cluster Anions. *J. Phys. Chem. A.* **2015**, *119* (20), 4755-4762.
- [3] Albury, R.M.; Pruitt, C.J.M.; Hester, T.H.; Goebbert, D.J. Fragmentation of  $\text{Cr}(\text{NO}_3)_4^-$ : Metal Oxidation upon  $\text{O}^{\bullet-}$  Abstraction. *J. Phys. Chem. A.* **2015**, *119* (47), 11471-11478.
- [4] Frański, R.; Sobieszczuk, K.; Gierczyk, B. Mass Spectrometric Decomposition of  $[\text{M}^{n+}(\text{NO}_3^-)_{n+1}]^-$  Anions Originating from Metal Nitrates  $\text{M}(\text{NO}_3)_n$ . *Int. J. Mass Spectrom.* **2014**, *369*, 98-104.
- [5] Hersleth, H.-P.; Hsiao, Y.-W.; Ryde, U.; Görbitz, C.H.; Andersson, K.K. The Crystal Structure of Peroxymyoglobin Generated through Cryoradiolytic Reduction of Myoglobin Compound III During Data Collection. *Biochem. J.* **2008**, *412* (2), 257-264.
- [6] Pedio, M.; Wu, Z.Y.; Benfatto, M.; Mascaraque, A.; Michel, E.; Ottaviani, C.; Crotti, C.; Peloi, M.; Zacchigna, M.; Comicioli, C. NEXAFS Experiment and Multiple Scattering Calculations on  $\text{KO}_2$ : Effects on the  $\pi$  Resonance in the Solid Phase. *Phys. Rev. B.* **2002**, *66* (14), 144109/144101-144109/144104.
- [7] Sawyer, D.T.; Valentine, J.S. How Super Is Superoxide? *Acc. Chem. Res.* **1981**, *14* (12), 393-400.
- [8] Unno, M.; Chen, H.; Kusama, S.; Shaik, S.; Ikeda-Saito, M. Structural Characterization of the Fleeting Ferric Peroxo Species in Myoglobin: Experiment and Theory. *J. Am. Chem. Soc.* **2007**, *129* (44), 13394-13395.

## CHAPTER 6

### COBALT NITRATE ANION COMPLEXES

Studies on cobalt nitrate anion complexes were performed and reveal metal oxide character similar to that of the chromium nitrate system. The cobalt oxide cores that form upon sequential elimination of  $\text{NO}_2^\bullet$  contain increasingly oxidized metal atoms. Each  $\text{O}^\bullet$  abstraction results in metal oxidation, and corresponding oxygen reduction to form  $\text{O}^{2-}$  ligands. Elimination of atomic oxygen occurs via double electron transfer from a single  $\text{O}^{2-}$  ligand to the metal. Elimination of molecular oxygen occurs via double electron transfer from two  $\text{O}^{2-}$  ligands to the metal to form an  $\text{O}_2$  product. The findings will be published in a peer-reviewed journal in 2016.

#### 6.1 Introduction

Previous studies have shown the impact of orbital vacancy on the fragmentation reactions of metal nitrate complexes and the redox chemistry of the core atoms. Metals such as aluminum,<sup>1</sup> gallium (Chapter 3), and zinc<sup>2</sup> produced sets of fragments, whose oxidation states were readily assignable. The reactions were primarily controlled by the radical nature, or conversely the partial vacancy, of the unique oxygen ligands of the core. Copper was the first metal studied in the series with a vacancy in the  $3d$  subshell, but the oxide of a metal with  $3d$  vacancies could not be studied since the +2 ion reduces readily to form the  $3d^{10}$  configuration.<sup>3</sup>

Studies using nickel nitrate,<sup>4</sup> with a  $3d^8$   $\text{Ni}^{2+}$  cation, showed rich redox chemistry. The nickel nitrate complexes decomposed via sequential  $\text{NO}_2^\bullet$  loss with instances of  $\text{NO}_3^\bullet$ , O atom, and  $\text{O}_2$  elimination. These losses typically resulted in partial or complete reduction of the nickel

cation. Chromium nitrate dissociation showed metal oxidation upon  $O^{\cdot-}$  abstraction, leading to an increase in oxidation state from +3 to +6.<sup>5</sup> Cobalt is expected to produce fragmentation patterns and have redox behavior similar to those observed for nickel or chromium nitrate since all three metals have multiple vacancies in the  $3d$  subshell.

## 6.2 Methods

A solution with 1 mM concentration was prepared by dissolving a sample of cobalt nitrate hexahydrate (0.030 g, 98%, Alfa Aesar), purchased from VWR International (Randor, PA, USA), in a mixture of HPLC grade solvents, methanol (50 mL) and acetonitrile (50 mL). The TSQ-7000 tandem mass spectrometer (Finnigan MAT, San Jose, CA) was used to perform CID and ERMS experiments. Authentic product ions were generated using in-source fragmentation for in-depth dissociation studies.

Density functional calculations were performed using the (U)B3LYP functional and the 6-311G+(3df) basis set. The lowest energy structures, with correct spin-states, were determined using a standard approach involving geometry optimization, followed by determination of the lowest energy structures for the product ions. Natural population analysis, NPA, calculations were performed on the optimized structures to determine the electron configurations, spin densities, and atomic charges of the metal and oxygen ligands.

## 6.3 Experimental Results

The Q1MS spectrum in Figure 6.1 shows the major ions:  $[Co(NO_3)_3]^-$ ,  $[CoO(NO_3)_2]^-$ ,  $[H(NO_3)_2]^-$ , and  $NO_3^-$ . The peaks at  $m/z$  80, 94, and 103 are likely nitrate anions coordinated to water, methanol, and acetonitrile respectively. The formation of  $[CoO(NO_3)_2]^-$  under the gentle

source conditions used for Q1MS data acquisition shows dissociation efficiency is high for the cobalt nitrate system.

The  $[\text{Co}(\text{NO}_3)_3]^-$  complex at  $m/z$  245 was chosen for CID studies and yields the fragments shown in Figure 6.2A. A high-intensity peak corresponding to the loss of  $\text{NO}_2^\bullet$  and lower intensity peaks for sequential loss of  $\text{NO}_2^\bullet$  and  $\text{NO}_3^-$  were observed. The spectrum agrees well with previously reported fragments<sup>6</sup> and a spectrum recorded on a Q-TOF instrument.<sup>7</sup>

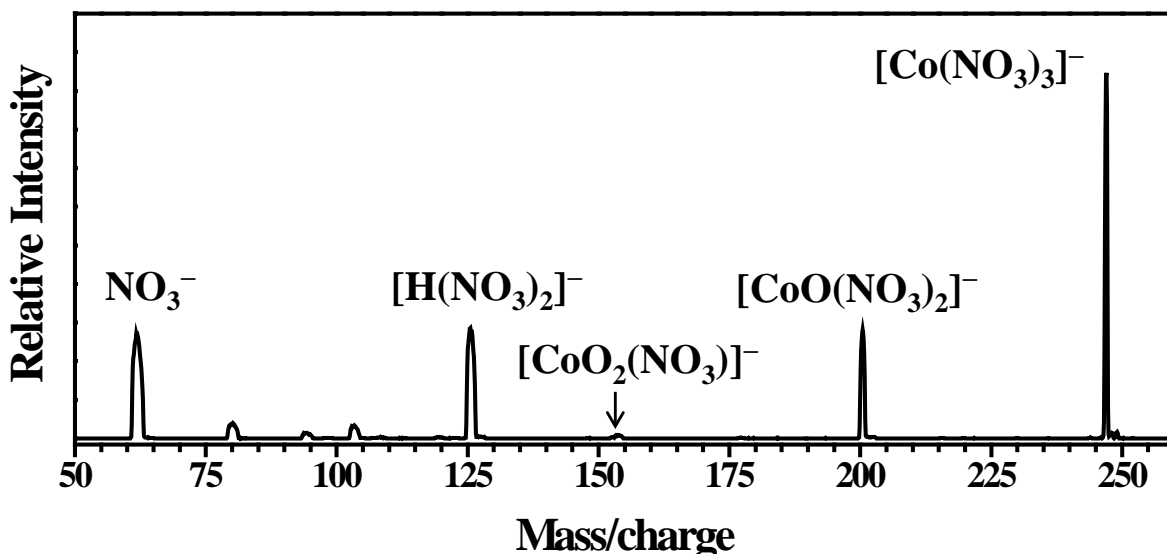


Figure 6.1 Representative Q1MS spectrum for the cobalt nitrate solution.

In-source fragmentation, detailed in Chapter 2, was used to optimize the intensity of  $[\text{CoO}(\text{NO}_3)_2]^-$  and other fragment ions for additional CID experiments. Figure 6.2B shows the  $[\text{CoO}(\text{NO}_3)_2]^-$  ion produces  $\text{NO}_3^-$  and undergoes consecutive elimination of  $\text{NO}_2^\bullet$  to yield  $[\text{CoO}_2(\text{NO}_3)]^-$  and  $[\text{CoO}_3]^-$ . The primary product ion,  $[\text{CoO}_2(\text{NO}_3)]^-$ , is shown in Figure 6.2C to undergo losses of  $\text{NO}_2^\bullet$  and  $\text{NO}_3^-$ . Three other fragments are shown in the spectrum, corresponding to  $[\text{CoO}(\text{NO}_3)]^-$ ,  $[\text{CoO}_2]^-$ , and  $[\text{CoO}]^-$ . The  $[\text{CoO}(\text{NO}_3)]^-$  fragment is formed via O atom elimination, whereas the other fragments are produced via sequential dissociation of the intermediate,  $[\text{CoO}_3]^-$ , as shown in Figure 6.2D. The  $[\text{CoO}_3]^-$  ion eliminates atomic oxygen and molecular oxygen to yield  $[\text{CoO}_2]^-$  and  $[\text{CoO}]^-$  respectively.

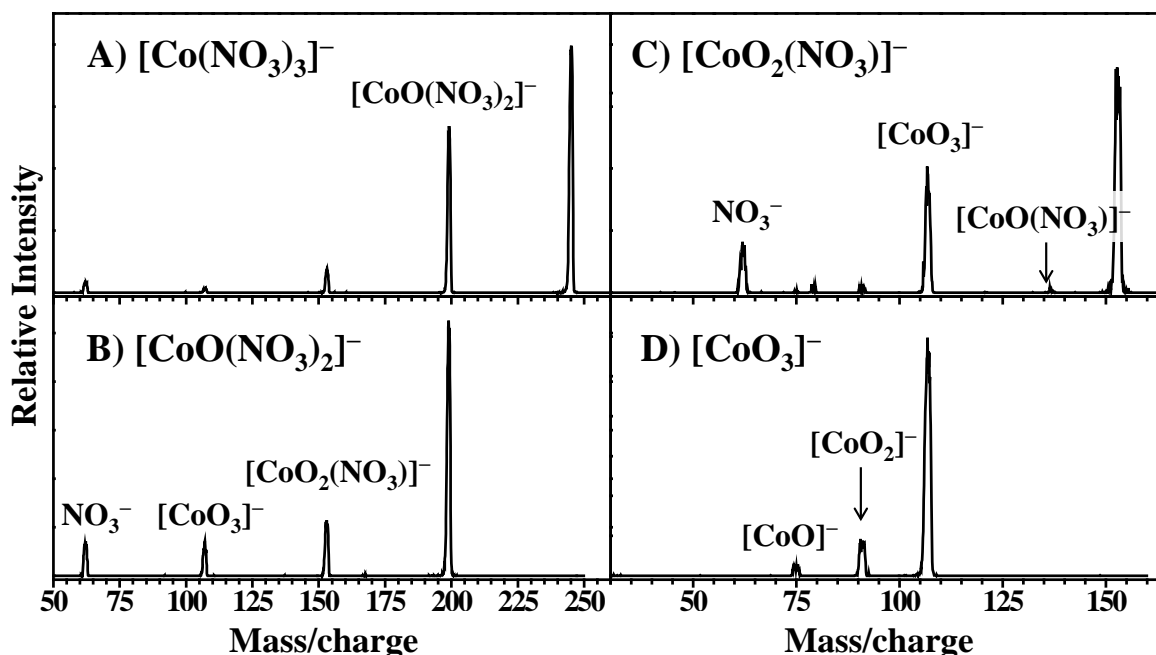


Figure 6.2 Representative CID spectra for (A)  $[\text{Co}(\text{NO}_3)_3]^-$ , (B)  $[\text{CoO}(\text{NO}_3)_2]^-$ , (C)  $[\text{CoO}_2(\text{NO}_3)]^-$ , and (D)  $[\text{CoO}_3]^-$  at 30 eV<sub>lab</sub> collision energy with 0.50 mTorr Ar collision gas.

Energy-dependent CID spectra, Figure 6.3, were recorded for the four ions studied by CID. Figure 6.3A shows the ERMS curves for  $[\text{Co}(\text{NO}_3)_3]^-$  dissociation. The intensity for the  $[\text{CoO}(\text{NO}_3)_2]^-$  fragment has an onset around 1.2 eV, reaches a maximum around 3.6 eV, and remains high over the entire collision energy range. The curve shape indicates this ion undergoes sequential fragmentation. The sequential fragments,  $[\text{CoO}_2(\text{NO}_3)]^-$  and  $[\text{CoO}_3]^-$ , are shown with onsets around 2 and 3 eV respectively. The  $\text{NO}_3^-$  fragment appears around 2 eV with similar intensity to the sequential fragments.

Figure 6.3B shows the primary and secondary elimination of  $\text{NO}_2^\bullet$  via the dissociation reactions,  $[\text{CoO}(\text{NO}_3)_2]^- \rightarrow [\text{CoO}_2(\text{NO}_3)]^- + \text{NO}_2^\bullet$  and  $[\text{CoO}_2(\text{NO}_3)_2]^- \rightarrow [\text{CoO}_3]^- + \text{NO}_2^\bullet$ , occur with virtually identical onsets to those observed in Figure 6.3A for  $[\text{Co}(\text{NO}_3)_3]^- \rightarrow [\text{CoO}(\text{NO}_3)_2]^- + \text{NO}_2^\bullet$  and  $[\text{CoO}(\text{NO}_3)_2]^- \rightarrow [\text{CoO}_2(\text{NO}_3)]^- + \text{NO}_2^\bullet$ , respectively. The intensity of the  $[\text{CoO}_2(\text{NO}_3)]^-$  fragment has an appearance energy onset around 1.2 eV, reaches a

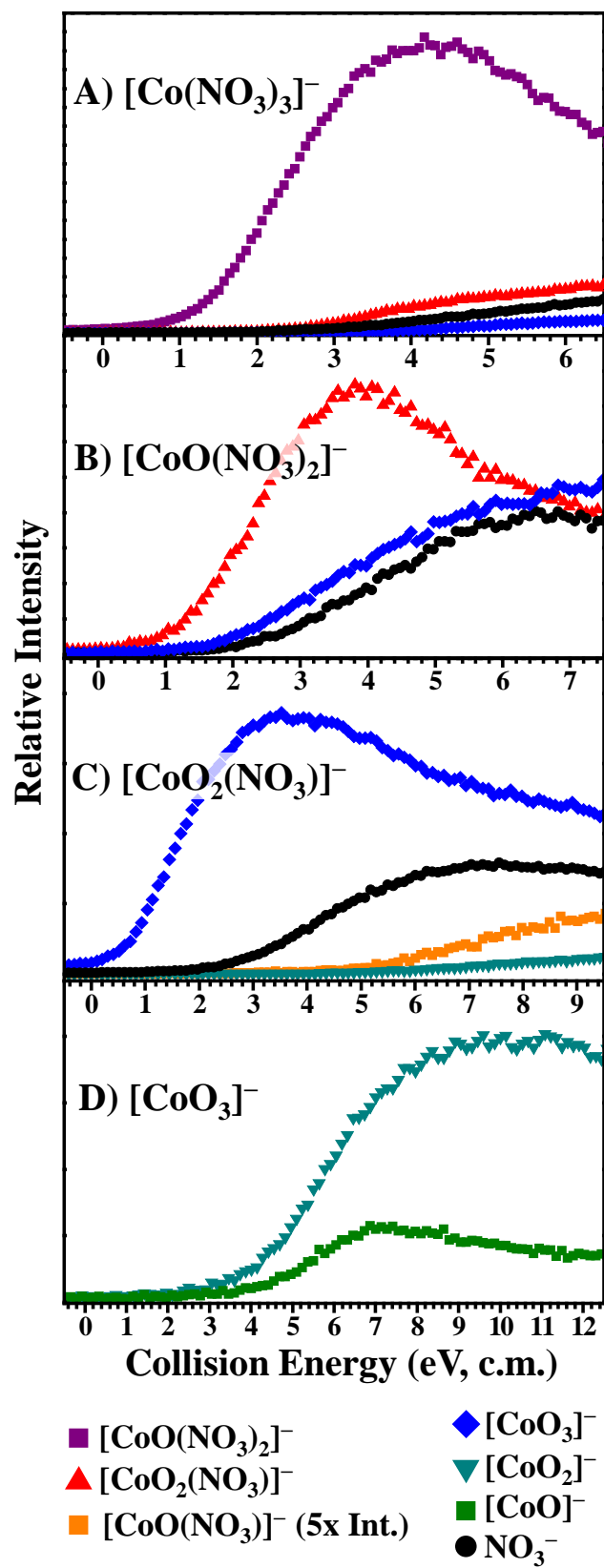


Figure 6.3 ERMS spectra for the dissociation of (A)  $[\text{Co}(\text{NO}_3)_3]^-$ , (B)  $[\text{CoO}(\text{NO}_3)_2]^-$ , (C)  $[\text{CoO}_2(\text{NO}_3)]^-$ , and (D)  $[\text{CoO}_3]^-$ .

maximum around 3.6 eV, and gradually decreases to match the intensity of the other two fragments. The secondary fragment,  $[\text{CoO}_3]^-$ , has a relatively low energy onset, around 2 eV, and moderate intensity over the collision energy range. The onset and curve shape for  $\text{NO}_3^-$  are nearly identical to those observed for the  $[\text{CoO}_3]^-$  ion. Figure 6.3C shows the energy-dependent dissociation curves for  $[\text{CoO}_2(\text{NO}_3)]^-$ . Elimination of  $\text{NO}_2^\bullet$  to yield  $[\text{CoO}_3]^-$  occurs with an onset at 0.5 eV. This very low energy onset can be attributed to excess internal energy deposited into the ions during in-source generation. The additional internal energy effectively lowers the amount of collision energy needed to induce fragmentation, and can shift the observed onset to lower energy. The  $[\text{CoO}_3]^-$  curve shape suggests sequential dissociation behavior, with an intensity maximum around 3 eV, followed by a gradual decrease. The high energy onset for  $[\text{CoO}_2]^-$  is consistent with sequential dissociation of  $[\text{CoO}_3]^-$  via loss of O atom. The  $\text{NO}_3^-$  curve shows an onset around 2.4 eV with the second highest intensity in the ERMS spectrum. The curves for  $[\text{CoO}(\text{NO}_3)]^-$  and  $[\text{CoO}_2]^-$  were initially overlaid, so the intensity scale of the  $[\text{CoO}(\text{NO}_3)]^-$  fragment was adjusted 5-fold for better visibility. The  $[\text{CoO}(\text{NO}_3)]^-$  fragment, corresponding to loss of O atom, has a very high energy onset around 5 eV. The onset for formation of  $[\text{CoO}(\text{NO}_3)]^-$  shows the elimination of O atom from  $[\text{CoO}_2(\text{NO}_3)]^-$  is a very high energy process.

Figure 6.3D shows two fragments,  $[\text{CoO}_2]^-$  and  $[\text{CoO}]^-$ , are produced upon dissociation of  $[\text{CoO}_3]^-$ . Elimination of O atom occurs with an onset of 3.8 eV, slightly lower than the 4.0 eV onset for  $\text{O}_2$  elimination. The intensity of both curves increases sharply at low energy and levels off at higher energies. The  $[\text{CoO}_2]^-$  ion has dominant intensity over the entire collision energy range. Any minor decrease in intensity for these ions at high collision energy is likely due to the decreased efficiency of ion transmission through the high voltage octopole.

## 6.4 Theoretical Results

Calculations were performed on the precursor ion and all of its observed dissociation products. The optimized structures and select Co-O bond distances for the cobalt complexes will be discussed in the order of their formation from experiment, as shown in the dissociation pathways from Figure 6.4 and Figure 6.5. The  $[\text{Co}(\text{NO}_3)_3]^-$  precursor has  $D_3$  symmetry with three nitrate ligands coordinated to the metal via two oxygen atoms. Elimination of  $\text{NO}_3^-$  was calculated to occur at 2.45 eV, slightly higher than the 2.00 eV for  $[\text{CoO}(\text{NO}_3)_2]^-$  formation via  $\text{NO}_2^\bullet$  elimination. The ERMS curves for these processes agree with theoretical calculations, showing a lower energy onset for the  $\text{NO}_2^\bullet$  elimination process.

The optimized  $C_2$ -symmetric structure of the  $[\text{CoO}(\text{NO}_3)_2]^-$  product appears similar to the lowest energy structure of the precursor. Two nitrate ligands remain coordinated in a bidentate manner to the metal. The oxygen ligand occupies the coordination site of the former, third nitrate ligand of the precursor. The Co-O bond distance is 1.66 Å.

Subsequent loss of  $\text{NO}_2^\bullet$  from  $[\text{CoO}(\text{NO}_3)_2]^-$  yields  $[\text{CoO}_2(\text{NO}_3)]^-$ , with a calculated energy of 2.41 eV. The  $[\text{CoO}_2(\text{NO}_3)]^-$  product ion was calculated to have  $C_{2v}$  symmetry, with

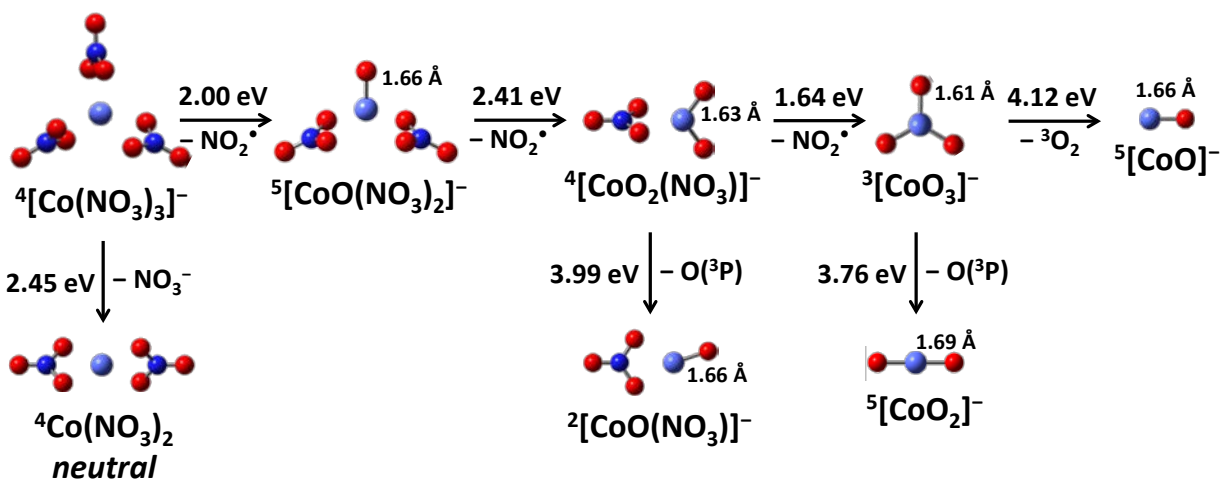


Figure 6.4 Calculated relative energy differences for the decomposition of  $[\text{Co}(\text{NO}_3)_3]^-$  at the (U)B3LYP/6-311+G(3df) level of theory. All energies include zero-point corrections. Select bond lengths are indicated. Atom colors: gray for cobalt, blue for nitrogen, and red for oxygen.

two oxygen ligands at an O-Co-O angle of 114.1°. The equivalent Co-O bond distance of 1.63 Å for the unique oxygen atoms is slightly shorter than the calculated Co-O bond distance for  $[\text{CoO}(\text{NO}_3)_2]^-$ . The calculated energy for the second  $\text{NO}_2^\bullet$  loss is slightly higher than for the first loss. The experimental appearance energies from Figure 6.3A and Figure 6.3B show similar energies for both losses presumably due to minor excess internal energy of  $[\text{CoO}(\text{NO}_3)_2]^-$ .

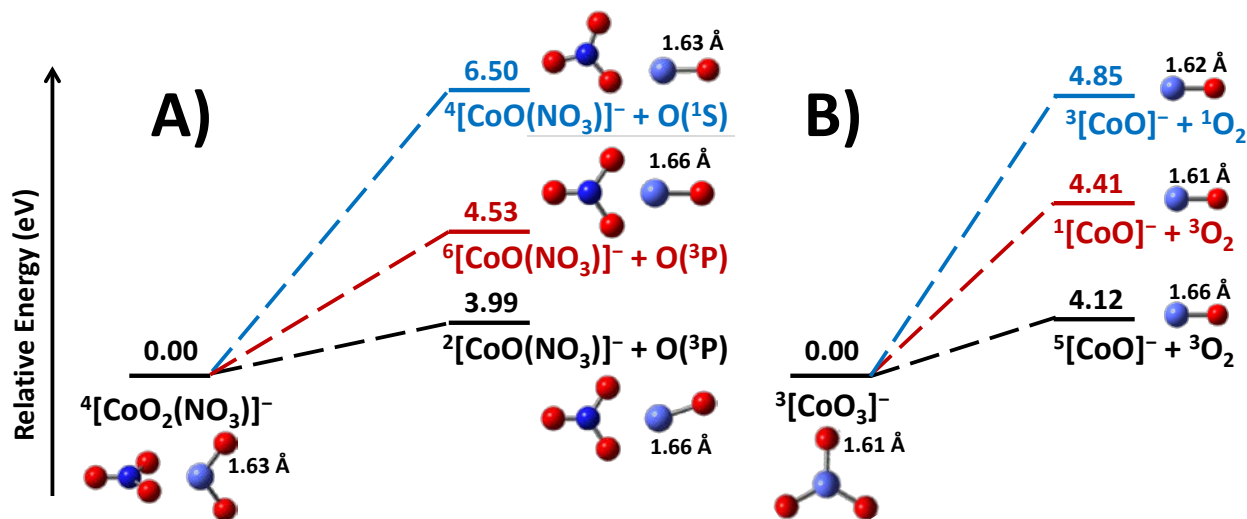


Figure 6.5 Potential energy diagram for (A) oxygen atom elimination from  $[\text{CoO}_2(\text{NO}_3)]^-$  and (B)  $\text{O}_2$  elimination from  $[\text{CoO}_3]^-$ . Select bond lengths are indicated. Black lines indicate the lowest elimination route, red lines indicate the intermediate energy pathway, and blue lines indicate the highest energy pathway.

Elimination of O atom from  $[\text{CoO}_2(\text{NO}_3)]^-$  yields  $[\text{CoO}(\text{NO}_3)]^-$ . Figure 6.4 and Figure 6.5A show the ground state structure of  $[\text{CoO}(\text{NO}_3)]^-$  contains a bidentate nitrate ligand coordinated to a neutral CoO core. The Co-O bond distance of 1.66 Å is slightly elongated relative to the bond distances in  $[\text{CoO}_2(\text{NO}_3)]^-$ . Figure 6.5A shows a potential energy diagram for three pathways leading to  $[\text{CoO}(\text{NO}_3)]^-$  formation. These pathways are presented together to emphasize the uncommonly low energy spin-splitting, within a 1 eV range, for the product complexes. The energy ordering of the cobalt complexes shows the quartet complex is lowest, followed by the doublet complex at 0.23 eV higher and the sextet complex at 0.78 eV. However, the stability of the O atom fragment ultimately determines the thermodynamic product for this

dissociation route. The black pathway shows  $O(^3P)$  can be eliminated to yield the doublet complex at 3.99 eV. The intermediate energy pathway in red yields the sextet complex at 4.53 eV. The highest energy pathway in blue yields the quartet complex at the unfavorable energy of 6.50 eV.

Fragmentation studies show  $NO_2^\bullet$  elimination from  $[CoO_2(NO_3)]^-$  yields  $[CoO_3]^-$ . The calculated energy for this loss is 1.64 eV. This process is shown as the lowest energy route for  $[CoO_2(NO_3)]^-$  fragmentation by experiment and theory. The  $[CoO_3]^-$  product is shown in Figure 6.4 with a high-symmetry trigonal planar geometry. The Co-O bond distance for all three Co-O bonds is 1.61 Å, the shortest calculated value for the cobalt system.

Elimination of O atom from  $[CoO_3]^-$  yields  $[CoO_2]^-$  at 3.76 eV, slightly lower in energy than the competitive pathway that yields  $[CoO]^-$  via  $O_2$  loss at 4.12 eV. The high energy onsets from the ERMS curves agree with the high calculated energies for these losses. The elimination of atomic oxygen has a slightly lower onset than  $O_2$  loss, consistent with theory. Both  $[CoO_2]^-$  and  $[CoO]^-$  are linear complexes with Co-O bond distances of 1.69 Å and 1.66 Å respectively.

The potential energy diagram in Figure 6.5B explicitly shows the loss of  $O_2$  from  $[CoO_3]^-$ . The fragmentation pathways for the three lowest energy spin-states of the product are shown due to the low energy spin-splitting of the product complexes. The splitting for three lowest energy spin-states of  $[CoO]^-$  shows the triplet complex is lowest in energy, followed by the quintet complex at 0.24 eV and the singlet complex at 0.52 eV. This set of potential energy diagrams emphasizes how important it is to consider the spin-state energies for the fragment complex and neutral fragment. The spin state of  $O_2$  ultimately determines the thermodynamic set of products for  $O_2$  loss from  $[CoO_3]^-$ . The lowest energy pathway in black shows the quintet-spin  $[CoO]^-$  complex is produced at 4.12 eV via  $^3O_2$  loss. The pathway in red shows the

formation of the higher energy singlet complex via  $^3\text{O}_2$  loss at 4.41 eV. The highest energy pathway in blue shows the formation of the triplet complex via elimination of  $^1\text{O}_2$  at 4.85 eV. The estimated energy for  $^1\text{O}_2$  was determined using the theoretical energy for  $^3\text{O}_2$  with a correction factor from the experimental triplet-singlet splitting, 0.98 eV.<sup>8</sup>

### 6.5 Cobalt-Oxygen Bonding

The nature of the metal oxide bonds in the cobalt complexes was investigated using orbital occupancy and atomic charge calculations. A simple picture of orbital mixing is provided in Figure 6.6 to illustrate metal-oxygen bond formation. The cobalt valence atomic orbitals are slightly higher in energy than the oxygen valence atomic orbitals. Sequential  $\text{O}^{\cdot-}$  abstraction produces relatively high spin complexes because of fairly degenerate molecular orbitals. Many problems were encountered when using the traditional analysis methods for the cobalt oxides due to competing metal-ligand  $\sigma$ - and  $\pi$ -donation. Calculations on the chromium oxide nitrate complexes required similar consideration during analysis. The calculated occupancies for the

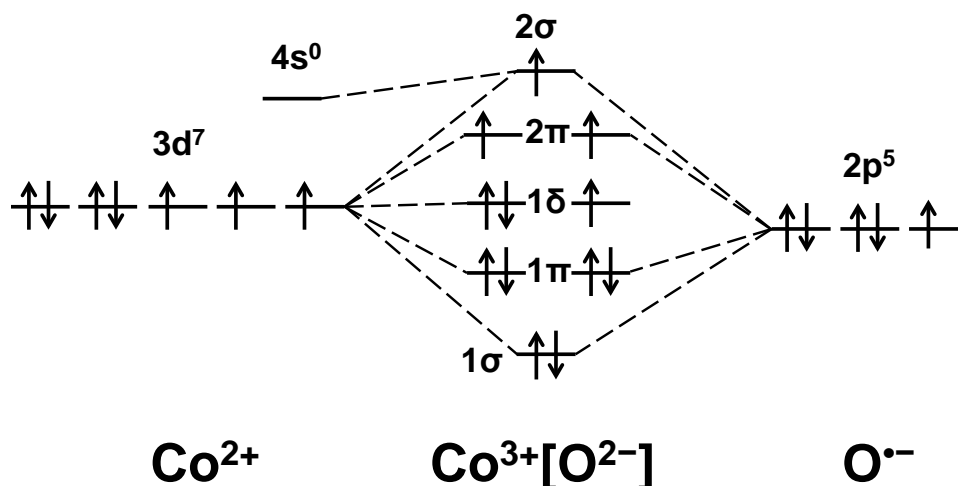


Figure 6.6 Hypothetical molecular orbital diagram for the formation of  $[\text{CoO}]^+$  from  $\text{Co}^{2+}$  and  $\text{O}^{\cdot-}$ . The relative orbital energies suggest cobalt is oxidized upon bond formation with oxygen.

Co( $3d$ ) and O( $2p$ ) subshells were found to provide the most detail on the redox properties of the metal oxides, whereas the calculated Co electron configuration, atomic charges, and excess spin values were found to be less informative.

Table 6.1 lists the  $3d$  occupancies for the cobalt atom in each complex. Seven electrons are assigned in the Co( $3d$ ) orbitals for  $[\text{Co}(\text{NO}_3)_3]^-$ , indicated by bold font. The excess electron spin values of  $2.67\alpha$  for  $\text{net}(\alpha - \beta)$  and  $2.76\alpha$  for Mulliken spin correspond to the excess spin of three  $\alpha$  electrons for the  $3d^7 \text{Co}^{2+}$  ion. Table 6.2 lists the electron configurations for the cobalt atom of each complex. The precursor ion,  $[\text{Co}(\text{NO}_3)_3]^-$ , was calculated to have an electron configuration of  $4s^{0.26} 3d^{7.26} 4p^{0.28}$ . Table 6.1 provides atomic charges and assigned electron configurations and oxidation states. The calculated NPA charge of +1.073 for Co is lower than the expected +2 oxidation state due to donation of electron density from the three nitrate ligands. The cobalt atom of this complex is assigned as having a  $3d^7$  electron configuration.

The cobalt oxide bond in  $[\text{CoO}(\text{NO}_3)_2]^-$  is formed upon  $\text{O}^{\cdot-}$  abstraction from a nitrate ligand. Table 6.1 shows the metal has six electrons assigned in the Co( $3d$ ) orbitals with partial  $\beta$ -densities. Table 6.3 shows the oxygen ligand has moderate  $\beta$ -occupancy in the  $2p$  subshell. These calculated occupancies for the cobalt and oxygen valence orbitals indicate electron transfer occurs from the metal to the oxygen atom through a  $\sigma$ -bond, and a corresponding degree of electron donation from the oxygen ligand to the metal atom occurs through a  $\pi$ -bond. The result is an oxidized cobalt atom,  $\text{Co}^{3+}$  with a  $3d^6$  assigned electron configuration, bonded to an  $\text{O}^{2-}$  ligand. This redox process is favored by the large magnitude of the charge product for the electrostatic interaction between the two ions. The short bond distance of 1.66 Å indicates relatively strong electrostatic attraction.

Table 6.1 Calculated atomic charges, excess spin values, and  $3d$  orbital occupancies for cobalt atom from a natural population analysis at the (U)B3LYP/6-311+G(3df) level of theory.

$3d$ orbital	Complex													
	$^4[\text{Co}(\text{NO}_3)_3]^-$		$^5[\text{CoO}(\text{NO}_3)_2]^-$		$^4[\text{CoO}_2(\text{NO}_3)]^-$		$^2[\text{CoO}(\text{NO}_3)]^-$		$^3[\text{CoO}_3]^-$		$^5[\text{CoO}_2]^-$		$^5[\text{CoO}]^-$	
	$\alpha$	$\beta$	$\alpha$	$\beta$	$\alpha$	$\beta$	$\alpha$	$\beta$	$\alpha$	$\beta$	$\alpha$	$\beta$	$\alpha$	$\beta$
$xy$	<b>0.99</b>	0.08	<b>0.99</b>	0.45	0.66	0.48	0.45	0.26	<b>0.99</b>	0.52	<b>1.00</b>	0.00	<b>1.00</b>	<b>1.00</b>
$xz$	<b>1.00</b>	0.10	<b>0.99</b>	0.11	<b>0.99</b>	0.26	<b>0.98</b>	0.33	<b>0.99</b>	0.52	<b>0.99</b>	0.51	<b>0.99</b>	0.23
$yz$	<b>1.00</b>	0.20	<b>0.99</b>	0.41	<b>0.99</b>	0.49	<b>1.00</b>	<b>0.88</b>	0.65	0.57	<b>0.99</b>	0.51	<b>0.99</b>	0.23
$x^2-y^2$	<b>0.99</b>	<b>0.93</b>	<b>0.98</b>	0.46	<b>0.99</b>	0.50	<b>0.95</b>	<b>0.94</b>	<b>0.89</b>	<b>0.86</b>	<b>1.00</b>	<b>1.00</b>	<b>1.00</b>	<b>1.00</b>
$z^2$	<b>1.00</b>	<b>0.98</b>	<b>0.99</b>	<b>0.88</b>	<b>0.98</b>	<b>0.92</b>	<b>0.93</b>	<b>0.95</b>	0.73	0.67	<b>0.91</b>	0.31	<b>0.97</b>	0.26
Net ( $\alpha - \beta$ )	$2.67\alpha$		$2.64\alpha$		$1.96\alpha$		$0.95\alpha$		$1.11\alpha$		$2.56\alpha$		$2.23\alpha$	
Mulliken spin	$2.76\alpha$		$2.78\alpha$		$2.08\alpha$		$1.01\alpha$		$1.16\alpha$		$2.88\alpha$		$3.35\alpha$	
NPA charge	+1.073		+1.054		+0.978		+0.593		+0.740		+1.064		+0.092	
Metal charge	+2		+3		+4		+2		+5		+3		+1	
Assigned config.	$3d^7$		$3d^6$		$3d^5$		$3d^7$		$3d^4$		$3d^6$		$4s^1 3d^7$	

Table 6.2 Calculated electron configurations for cobalt atom from a natural population analysis at the (U)B3LYP/6-311+G(3df) level of theory.

Complex	Cobalt electron configuration
$^4[\text{Co}(\text{NO}_3)_3]^-$	$4s^{0.26} 3d^{7.26} 4p^{0.28}$
$^5[\text{CoO}(\text{NO}_3)_2]^-$	$4s^{0.25} 3d^{7.26} 4p^{0.42}$
$^4[\text{CoO}_2(\text{NO}_3)]^-$	$4s^{0.28} 3d^{7.29} 4p^{0.45}$
$^2[\text{CoO}(\text{NO}_3)]^-$	$4s^{0.49} 3d^{7.67} 4p^{0.23}$
$^3[\text{CoO}_3]^-$	$4s^{0.33} 3d^{7.40} 4p^{0.51}$
$^5[\text{CoO}_2]^-$	$4s^{0.32} 3d^{7.23} 4p^{0.37}$
$^5[\text{CoO}]^-$	$4s^{0.83} 3d^{7.67} 4p^{0.37}$

The low magnitude of the calculated atomic charges in  $[\text{CoO}(\text{NO}_3)_2]^-$  do not correspond to those of a pure  $\text{Co}^{3+}[\text{O}^{2-}]$  ion contact pair. Rather, the NPA charges of +1.054 for cobalt and -0.678 for oxygen reflect the competing donation and back-donation of electron density across the Co-O bond. The calculated electron configuration of  $4s^{0.25} 3d^{7.26} 4p^{0.42}$  for  $[\text{CoO}(\text{NO}_3)_2]^-$  is virtually unchanged from that of the precursor. The increased Co( $4p$ ) density for  $[\text{CoO}(\text{NO}_3)_2]^-$  is a valid indicator of  $\pi$ -donation from the  $\text{O}^{2-}$  ligand. The loss of  $\beta$ -electron density from the metal to the oxygen ligand and corresponding gain of  $\beta$ -electron density from the oxygen ligand yields excess electron spin values that are nearly unchanged from those of the precursor. The cobalt atom of  $[\text{CoO}(\text{NO}_3)_2]^-$  is assigned as  $\text{Co}^{3+}$  with a  $3d^6$  configuration. The  $[\text{CoO}]^+$  core of  $[\text{CoO}(\text{NO}_3)_2]^-$  is best described as a  $\text{Co}^{3+}[\text{O}^{2-}]$  ion contact pair.

Elimination of  $\text{NO}_2^\bullet$  from  $[\text{CoO}(\text{NO}_3)_2]^-$  yields  $[\text{CoO}_2(\text{NO}_3)]^-$ . The quartet-spin product has a cobalt atom with five electrons assigned in the  $3d$  orbitals and many orbitals with partial occupancy. The  $\alpha$ -occupancy for the Co( $3d_{xy}$ ) orbital of  $[\text{CoO}_2(\text{NO}_3)]^-$  is noticeably lower than that for  $[\text{CoO}(\text{NO}_3)_2]^-$ , indicating metal oxidation upon  $\text{O}^{\bullet-}$  abstraction. The  $\beta$ -densities in the Co( $3d$ ) subshell are noticeably higher than that for  $[\text{CoO}(\text{NO}_3)_2]^-$ , indicating  $\pi$ -donation by the oxygen ligands of  $[\text{CoO}_2(\text{NO}_3)]^-$ . The cobalt atom is assigned an electron configuration of  $3d^5$ ,

and the oxygen ligands are both assigned as O<sup>2-</sup> ligands. The low excess electron spin values for the cobalt and oxygen atoms are the result of decreased  $\alpha$ -occupancy by  $\sigma$ -donation and increased  $\beta$ -occupancy by  $\pi$ -donation. The electrostatic charge product of this metal oxide is quite high, and the decreased bond distances of 1.63 Å reflect the increased attraction between the cobalt and oxygen atoms.

Table 6.3 Calculated atomic charges, excess spin values, and 2*p* orbital occupancies for unique oxygen atoms from a natural population analysis at the (U)B3LYP/6-311+G(3df) level of theory.

	Complex											
	<sup>5</sup> [CoO(NO <sub>3</sub> ) <sub>2</sub> ] <sup>-</sup>		<sup>4</sup> [CoO <sub>2</sub> (NO <sub>3</sub> )] <sup>-</sup>		<sup>2</sup> [CoO(NO <sub>3</sub> )] <sup>-</sup>		<sup>3</sup> [CoO <sub>3</sub> ] <sup>-</sup>		<sup>5</sup> [CoO <sub>2</sub> ] <sup>-</sup>		<sup>5</sup> [CoO] <sup>-</sup>	
<i>orbital</i>	$\alpha$	$\beta$	$\alpha$	$\beta$	$\alpha$	$\beta$	$\alpha$	$\beta$	$\alpha$	$\beta$	$\alpha$	$\beta$
2 <i>p<sub>x</sub></i>	0.98	0.56	0.97	0.78	0.82	0.87	0.98	0.62	0.98	0.70	0.97	0.75
2 <i>p<sub>y</sub></i>	0.96	0.70	0.65	0.75	0.70	0.84	0.74	0.78	0.98	0.70	0.97	0.75
2 <i>p<sub>z</sub></i>	0.98	0.60	0.98	0.63	0.96	0.78	0.78	0.80	0.91	0.84	0.96	0.74
Net ( $\alpha - \beta$ )	1.06 $\alpha$		0.44 $\alpha$		0.01 $\beta$		0.30 $\alpha$		0.63 $\alpha$		0.66 $\alpha$	
Mull. spin	1.04 $\alpha$		0.42 $\alpha$		0.00		0.28 $\alpha$		0.56 $\alpha$		0.65 $\alpha$	
NPA charge	-0.678		-0.646		-0.887		-0.580		-1.032		-1.092	

The calculated electron configuration of 4s<sup>0.28</sup> 3d<sup>7.29</sup> 4p<sup>0.45</sup> for the cobalt atom of [CoO<sub>2</sub>(NO<sub>3</sub>)]<sup>-</sup> is not significantly different from that of [CoO(NO<sub>3</sub>)<sub>2</sub>]<sup>-</sup>. The relatively high Co(4*p*) occupancy corresponds to a high degree of  $\pi$ -donation from each O<sup>2-</sup> ligand. The comparison of cobalt NPA charges between the precursor and the lower value of +0.978 for [CoO<sub>2</sub>(NO<sub>3</sub>)]<sup>-</sup> reveals a trend similar to that found for chromium nitrate. Metal oxidation occurs upon O<sup>-</sup> abstraction, resulting in  $\pi$ -donation from the O<sup>2-</sup> ligands that causes the metal charge to be lower than expected. The oxygen ligands in [CoO<sub>2</sub>(NO<sub>3</sub>)]<sup>-</sup> have identical 2*p* occupancies with low  $\alpha$ -density and moderate  $\beta$ -density, leading to low excess spin values for the O(2*p*) subshell. The low magnitude NPA charge of -0.646 for each unique oxygen atom indicates the

extent to which ligand-to-metal  $\pi$ -donation causes the atomic charges to deviate from the expected value of  $-2$ . The neutral  $\text{CoO}_2$  core of  $[\text{CoO}_2(\text{NO}_3)]^-$  is best described as  $\text{Co}^{4+}[\text{O}^{2-}]_2$ .

An unusual elimination of O atom occurs from  $[\text{CoO}_2(\text{NO}_3)]^-$  to yield  $[\text{CoO}(\text{NO}_3)]^-$ . Table 6.1 shows seven electrons for the cobalt  $3d$  subshell are assigned. Two electrons from an  $\text{O}^{2-}$  ligand in  $[\text{CoO}_2(\text{NO}_3)]^-$  are transferred to the  $3d^5$  metal upon O atom loss. The  $3d^7$  cobalt cation of  $[\text{CoO}(\text{NO}_3)]^-$  has a calculated electron configuration of  $4s^{0.49} 3d^{7.67} 4p^{0.23}$ , with considerably higher occupancy in the  $4s$  and  $3d$  orbitals than the  $4s^{0.26} 3d^{7.26} 4p^{0.28}$  configuration of the other  $3d^7$  complex,  $[\text{Co}(\text{NO}_3)_3]^-$ . The calculated atomic charge of  $+0.593$  for cobalt and increased Co-O bond distance of  $1.66 \text{ \AA}$  indicate a reduced cobalt atom. The O( $2p$ ) occupancy of the unique oxygen atom shows moderate  $\alpha$ -density and high  $\beta$ -density, for an overall zero excess spin value. The ligand is assigned the  $-2$  oxidation state. The neutral CoO core of  $[\text{CoO}(\text{NO}_3)]^-$  is best described as the  $\text{Co}^{2+}[\text{O}^{2-}]$  ion contact pair.

Elimination of  $\text{NO}_2^\bullet$  from  $[\text{CoO}_2(\text{NO}_3)]^-$  yields  $[\text{CoO}_3]^-$ . The Co( $3d$ ) orbitals for  $[\text{CoO}_3]^-$  show four electrons are assigned, with low  $\alpha$ -density in two orbitals and moderate  $\beta$ -density in many orbitals. The nearly uniform, moderate  $\beta$ -occupancy of the orbitals reflects a similar degree of electron donation from the oxygen ligands into those Co( $3d$ ) orbitals. The cobalt atom has an assigned oxidation state of  $+5$  for the  $3d^4$  configuration. The short Co-O bond distances of  $1.61 \text{ \AA}$  reflect the high oxidation states of the cobalt and oxygen atoms. The O( $2p$ ) occupancy shows moderate  $\alpha$ - and  $\beta$ -electron density, yielding a low excess spin value for the three identical oxygen atoms. The  $\pi$ -donation from the ligands causes the NPA charges for cobalt and oxygen to have low magnitudes,  $+0.740$  and  $-0.580$  respectively. The inverse trend in magnitude for oxidation state and nominal charge is maintained in the cobalt system, as for the chromium system. The  $4s^{0.33} 3d^{7.40} 4p^{0.51}$  calculated electron configuration for cobalt shows high  $4p$

occupancy, indicating a high degree of electron donation by the ligands to the metal. The  $[\text{CoO}_3]^-$  ion is best described as  $\text{Co}^{5+}[\text{O}^{2-}]_3$ .

The  $[\text{CoO}_3]^-$  ion loses O atom to yield  $[\text{CoO}_2]^-$ . Table 6.1 shows six Co( $3d$ ) electrons are assigned. An  $\text{O}^{2-}$  ligand from  $[\text{CoO}_3]^-$  transfers two electrons upon O atom loss to yield a  $3d^6$  cobalt atom in  $[\text{CoO}_2]^-$ . There are three Co( $3d$ ) orbitals with partial  $\beta$ -occupancy and one with low occupancy, similar to those observed for the other  $3d^6$  complex,  $[\text{CoO}(\text{NO}_3)_2]^-$ . The spin density values and Co-O bond distance of 1.66 Å are similar to those of  $[\text{CoO}(\text{NO}_3)_2]^-$ . The O( $2p$ ) occupancy shows moderate  $\beta$ -density, consistent with electron donation from the ligands to the metal. The low magnitude of the NPA charges for cobalt and the oxygen atoms are also consistent with ligand-to-metal donation. The calculated electron configuration of  $4s^{0.32} 3d^{7.23} 4p^{0.37}$  for cobalt is similar to the  $4s^{0.25} 3d^{7.26} 4p^{0.42}$  configuration for  $[\text{CoO}(\text{NO}_3)_2]^-$ . The  $[\text{CoO}_2]^-$  ion is best described as  $\text{Co}^{3+}[\text{O}^{2-}]_2$ .

The  $[\text{CoO}]^-$  ion is formed by elimination of  $\text{O}_2$  from  $[\text{CoO}_3]^-$ . The  $\text{Co}^{5+}$  ion of  $[\text{CoO}_3]^-$  undergoes double electron transfer from two separate  $\text{O}^{2-}$  ligands to yield a  $\text{Co}^+$  ion in the  $[\text{CoO}]^-$  product. The  $3d$  occupancy given in Table 6.1 shows seven electrons assigned for Co, but does not show the single electron in the  $4s$  subshell that is also present. The cobalt atom is assigned an electron configuration of  $4s^1 3d^7$ . The excess spin values differ due to the discrepancy in which orbitals are included in the spin calculation. Mulliken spin includes all of the cobalt  $4s$ ,  $4p$ , and  $3d$  orbitals, whereas  $\text{net}(\alpha - \beta)$  uses solely the  $3d$  orbital. The O( $2p$ ) occupancy value and  $\text{net}(\alpha - \beta)$  value for the unique oxygen atom are similar to those of  $[\text{CoO}_2]^-$ , indicating a similar degree of electron donation from the oxygen ligand to the metal. The calculated electron configuration of  $4s^{0.83} 3d^{7.67} 4p^{0.37}$  for cobalt in  $[\text{CoO}]^-$  shows considerable occupancy in the  $4s$  and  $3d$  orbitals, with moderate  $4p$  occupancy consistent with

ligand-to-metal donation. The near-zero NPA charge for cobalt reflects the highly reduced nature of the cobalt atom in  $[\text{CoO}]^-$ . The ion can be described as the  $\text{Co}^+[\text{O}^{2-}]$  ion contact pair.

## 6.6 Conclusions

A diverse set of reactions is observed for the fragmentation of cobalt nitrate. Several, consecutive losses of  $\text{NO}_2^\bullet$  generate cobalt oxide nitrate fragments, which can subsequently undergo losses of O and  $\text{O}_2$ . The  $3d$  orbitals of cobalt are slightly higher, but nearly equal in energy to the  $2p$  orbitals of oxygen. Calculations show high spin multiplicities for the first sets of fragments due to the orbital degeneracy. The smaller fragment complexes also tend to have a high spin multiplicity, but the individual values for excess electron spin on the core atoms are very much lower than expected because of competing electron transfer through a  $\sigma$ -bond and electron donation through a  $\pi$ -bond.

The dissociation pattern of cobalt nitrate appears similar to that of chromium nitrate. Sequential  $\text{NO}_2^\bullet$  loss leads to the formation of metal oxide cores containing numerous oxygen ligands. The smallest metal oxide anions eliminate O and  $\text{O}_2$ . The redox chemistry is nearly identical between the two systems. Chromium is consecutively oxidized with each  $\text{O}^\bullet$  abstraction, and the same trend is observed for cobalt.<sup>5</sup> Whereas the nickel system showed evidence of partial metal oxidation, cobalt was the latest transition metal in this dissertation to show full metal oxidation as a primary effect of dissociation.<sup>4</sup>

## 6.7 References

- [1] Lightcap, J.; Hester, T.H.; Kamena, K.; Albury, R.M.; Pruitt, C.J.M.; Goebbert, D.J. Gas-Phase Fragmentation of Aluminum Oxide Nitrate Anions Driven by Reactive Oxygen Radical Ligands. *J. Phys. Chem. A*. **2016**, *120* (9), 1501-1507.

- [2] Hester, T.H.; Goebbert, D.J. Experimental and Theoretical Study of the Decomposition of  $[\text{Zn}(\text{NO}_3)_3]^-$ . *Chem. Phys. Lett.* **2016**, In Press.
- [3] Pruitt, C.J.M.; Goebbert, D.J. Experimental and Theoretical Study of the Decomposition of Copper Nitrate Cluster Anions. *J. Phys. Chem. A.* **2015**, *119* (20), 4755-4762.
- [4] Hester, T.H.; Albury, R.M.; Pruitt, C.J.M.; Goebbert, D.J. Fragmentation of  $[\text{Ni}(\text{NO}_3)_3]^-$ : A Study of Nickel-Oxygen Bonding and Oxidation States in Nickel Oxide Fragments. *Inorg. Chem.* **2016**, *55* (13), 6634-6642.
- [5] Albury, R.M.; Pruitt, C.J.M.; Hester, T.H.; Goebbert, D.J. Fragmentation of  $\text{Cr}(\text{NO}_3)_4^-$ : Metal Oxidation upon  $\text{O}^-$  Abstraction. *J. Phys. Chem. A.* **2015**, *119* (47), 11471-11478.
- [6] Li, F.; Byers, M.A.; Houk, R.S. Tandem Mass Spectrometry of Metal Nitrate Negative Ions Produced by Electrospray Ionization. *J. Am. Soc. Mass Spectrom.* **2003**, *14* (6), 671-679.
- [7] Frański, R.; Sobieszczuk, K.; Gierczyk, B. Mass Spectrometric Decomposition of  $[\text{M}^{n+}(\text{NO}_3^-)_{n+1}]^-$  Anions Originating from Metal Nitrates  $\text{M}(\text{NO}_3)_n$ . *Int. J. Mass Spectrom.* **2014**, *369*, 98-104.
- [8] Ervin, K.M.; Anusiewicz, I.; Skurski, P.; Simons, J.; Lineberger, W.C. The Only Stable State of  $\text{O}_2^-$  Is the  $\text{X}^2\Pi_g$  Ground State and It (Still!) Has an Adiabatic Electron Detachment Energy of 0.45 eV. *J. Phys. Chem. A.* **2003**, *107* (41), 8521-8529.

## CHAPTER 7

### PROTONATED POLYETHYLENE GLYCOL

Studies were carried out on samples of polyethylene glycol, PEG and were the earliest in the author's research timeline. These studies became a cornerstone for how mass spectrometry data were collected and displayed, and what experimental and theoretical methods would be used to analyze future chemical systems. The findings were published as a research article in 2013 in the *Journal of Mass Spectrometry*.<sup>1</sup>

Early investigations by Lattimer and Hargiss<sup>2-4</sup> on protonated polyethylene glycol fragmentation suggest the dissociation mechanism includes both direct and sequential processes. Experiments designed to study the proposed mechanisms of sequential dissociation are absent from the literature. In order to obtain additional experimental details about the fragmentation reactions, the dissociation of protonated polyethylene glycol was studied by energy-dependent collision-induced dissociation, CID. Key fragment ions were separated by mass differences corresponding to the loss of single monomer units. Several fragment ions were also generated by in-source fragmentation and studied by CID. These experiments indicate the primary ions undergo sequential dissociation by the loss of either one or two monomer units. The results suggest that at least two different mechanisms must be considered to explain the sequential dissociation of protonated polyethylene glycols. The reaction involving the elimination of two subunits suggests the loss of a six-membered 1,4-dioxane product, whereas the elimination of a single subunit involves the loss of acetaldehyde by a 1,2-hydride shift rearrangement.

## 7.1 Introduction

Protonated polyethylene glycols,  $[\text{H}+\text{PEG}_n]^+$ , have been studied by mass spectrometry for several decades starting with the pioneering work of Lattimer and Hargiss.<sup>2-4</sup> In their early experiments, the fragmentation patterns at both low and high collision energies were reported, and possible dissociation mechanisms were put forward.<sup>2-4</sup> Since that time, several other studies of  $[\text{H}+\text{PEG}_n]^+$  have been published, but the accepted mechanism for dissociation has remained largely unchanged. Although  $[\text{H}+\text{PEG}_n]^+$  is a well-known species in mass spectrometry, further experiments have not been carried out to confirm the original dissociation mechanisms.

The protonated complexes belong to a broader class of cationized PEGs, including  $\text{Li}^+$ ,  $\text{Na}^+$ ,  $\text{K}^+$  and other metal ion complexes, that have been characterized by other experiments.<sup>2,5-19</sup> Even though protonated and metal ion complexes are both positively charged, their interactions with PEG are fundamentally different due to the much larger size of the metal cations. The most significant difference is that larger cation sizes allow for multiple interactions with the electronegative oxygen atoms from PEG. In contrast, the proton is much smaller and will localize on a single oxygen atom in PEG (disregarding for the moment the possibility of proton mobility). Due to the strong, localized binding of protons compared to alkali metal ions, the properties and fragmentation patterns of  $[\text{H}+\text{PEG}_n]^+$  are considerably different from their metal ion counterparts.<sup>2,14,15,19,20</sup> Although the proton in  $[\text{H}+\text{PEG}_n]^+$  is localized on a single oxygen atom in the complex, a large number of similar binding sites in PEG produces a mixture of isomers of  $[\text{H}+\text{PEG}_n]^+$  in any ion source. Hydrogen bonding interactions bring the proton into closer proximity to many oxygen atoms where proton transfer and scrambling is possible.

Fragmentation of  $[\text{H}+\text{PEG}_n]^+$  produces a series of regularly spaced peaks at  $m/z = 44(m) + 1$ , where  $m$  is an integer.<sup>2-4</sup> The relative spacing of the fragment masses reflects

the size of the ethylene oxide,  $-(C_2H_4O)-$ , monomer units. Early studies have already recognized that  $[H+PEG_n]^+$  undergoes both direct and sequential dissociation.<sup>2,3</sup> Although mechanisms for dissociation have been proposed based on fragmentation studies, advanced experimental or theoretical studies focusing on the fragmentation mechanism have not been carried out. A generalized example of the most common mechanism proposed from early experiments is summarized in Figure 7.1.<sup>2-4</sup> The protonated species undergo C–O bond cleavage at the protonation site yielding a short neutral PEG fragment and a complementary primary carbocation. It has been suggested that sequential dissociation involves cyclization and bond formation between the carbocation and an oxygen atom to yield a formally positively charged oxygen atom. The cyclic intermediate can subsequently fragment by C–O bond cleavage at the positively charged oxygen to form a secondary fragment carbocation and a neutral,  $3n$ -membered, cyclic fragment, such as 1,4-dioxane, ethylene oxide, etc. Although this mechanism can explain the experimental fragmentation spectrum of  $[H+PEG_n]^+$ , *it is not the only possibility*. An alternative explanation is based on the well-known chemistry of primary carbocations, which undergo rapid 1,2-hydride shift rearrangements.<sup>21-23</sup> If a hydride shift is considered in  $[H+PEG_n]^+$  dissociation, as shown in Figure 7.2, a different set of decomposition reactions are predicted, where the hydride shift forms an oxonium ion intermediate. The intermediate also has a formally positively charged oxygen atom, which decomposes sequentially by C–O bond cleavage resulting in the loss of acetaldehyde. Similar reactions have been shown to occur during the dissociation of  $[Li+PEG_n]^+$  and  $[Na+PEG_n]^+$ .<sup>12</sup> Without further evidence, both mechanisms are equally plausible based on CID mass spectrometry. Given the intriguing differences between these two possible mechanisms, we have carried out experiments on  $[H+PEG_n]^+$  in an attempt to study the decomposition process.

In this work, we investigated the fragmentation of size-selected  $[\text{H}+\text{PEG}_n]^+$  using two approaches. First, we studied the energy dependence of fragment formation of the ions to learn about the energetic trends and correlations between each fragment. Second, we carried out in-source fragmentation of  $[\text{H}+\text{PEG}_n]^+$  to generate primary fragments. The primary fragments were mass-selected and subjected to CID in order to see which secondary fragments are formed. Both of these experiments point toward a complex set of decomposition reactions upon CID of  $[\text{H}+\text{PEG}_n]^+$ . The goal of this work was to obtain additional experimental data on  $[\text{H}+\text{PEG}_n]^+$  dissociation that could be used to learn about the sequential dissociation mechanism.

## 7.2 Methods

A solution with 1 mM concentration was prepared by dissolving a sample of PEG-400 (0.040 g, average molecular weight of 392 g/mol, EMD Millipore) in HPLC grade methanol (100 mL). All experiments were performed on a Finnigan TSQ-7000 tandem mass spectrometer with an octopole collision cell, in a QoQ configuration, (Finnigan MAT, San Jose, CA) operating with the Excalibur software package.

In-source fragmentation experiments were carried out by increasing the tube lens voltage in the differentially pumped inlet region of the ion source until fragment ions were observed in the mass spectrum. The in-source fragments were mass-selected and studied by CID using collision energies ramped from 0 – 50 eV<sub>lab</sub>. These experiments were also carried out using low collision gas pressure to minimize effects from multiple collisions.

### 7.3 Results

The PEG solution was electrosprayed and peaks corresponding to a series of protonated PEG oligomers were detected, as shown in the Q1MS spectrum, Figure 7.1. Other low-intensity series of sodium and ammonium oligomer adducts were also observed due to solvent impurities. The coordination of ions to PEG is common due to the Lewis basic nature of the oxygen atoms in the backbone. Typically ions are large enough to coordinate to multiple oxygen atoms, such as coordination of sodium and potassium cations to crown ethers, cyclic analogs to PEG.<sup>2,8,18,19</sup> Protons localize on specific oxygen atoms, i.e. protonation sites, within the PEG structure.

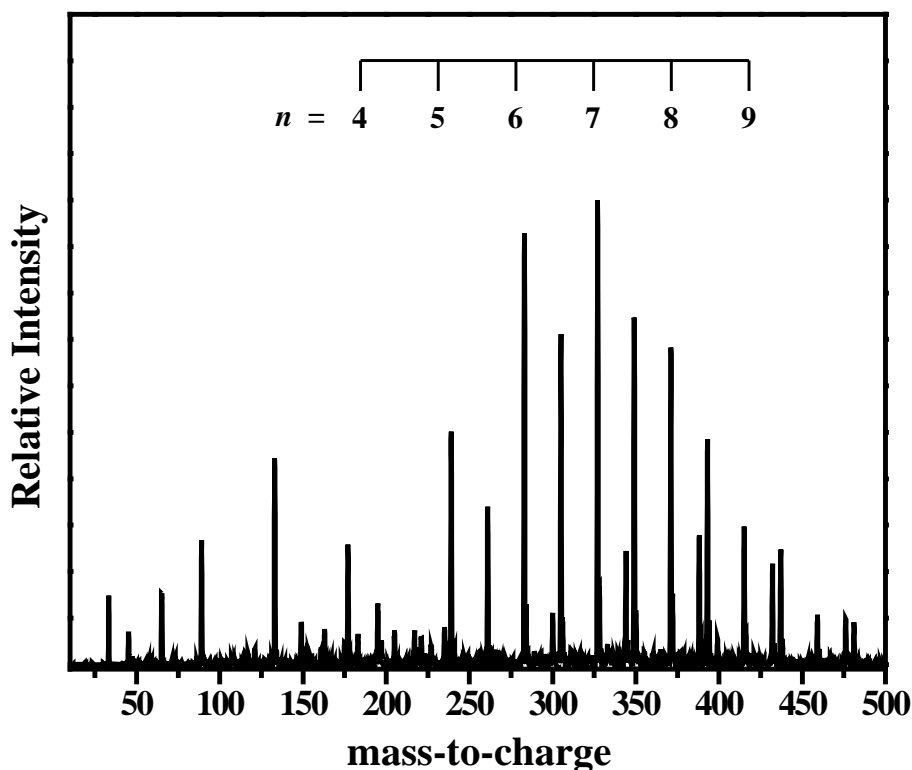


Figure 7.1 Representative Q1MS spectrum for a PEG<sub>n</sub> solution with peaks for  $n = 4 - 9$  labeled.

The general structure of  $[H+PEG_n]^+$  is shown in Figure 7.2. The repeating monomer unit, ethylene oxide, is given in parentheses as  $C_2H_4O$  with the subscript  $n$ . Previous studies have been performed on the dissociation of  $[H+PEG_n]^+$ .<sup>3-5</sup> Figure 7.2 shows the direct dissociation mechanism proposed by Lattimer and Hargiss, in which cleavage occurs at the C–O bond

adjacent to the protonation site. Figure 7.2 continues with a sequential dissociation mechanism, in which an oxygen atom lone pair bonds to the positive carbon atom in the resonance form to eliminate cyclized C<sub>2</sub>H<sub>4</sub>O units. Figure 7.3 shows another mechanism that could result in sequential monomer unit losses. This pathway is the 1,2 hydride shift rearrangement, a common isomerization process for carbocations.<sup>21-23</sup>

The [H+PEG<sub>n</sub>]<sup>+</sup> ions, *n* = 4 – 9, were studied using CID, Figure 7.4. The fragments are labeled using common polymer fragment ion notation, in which the fragments are given as

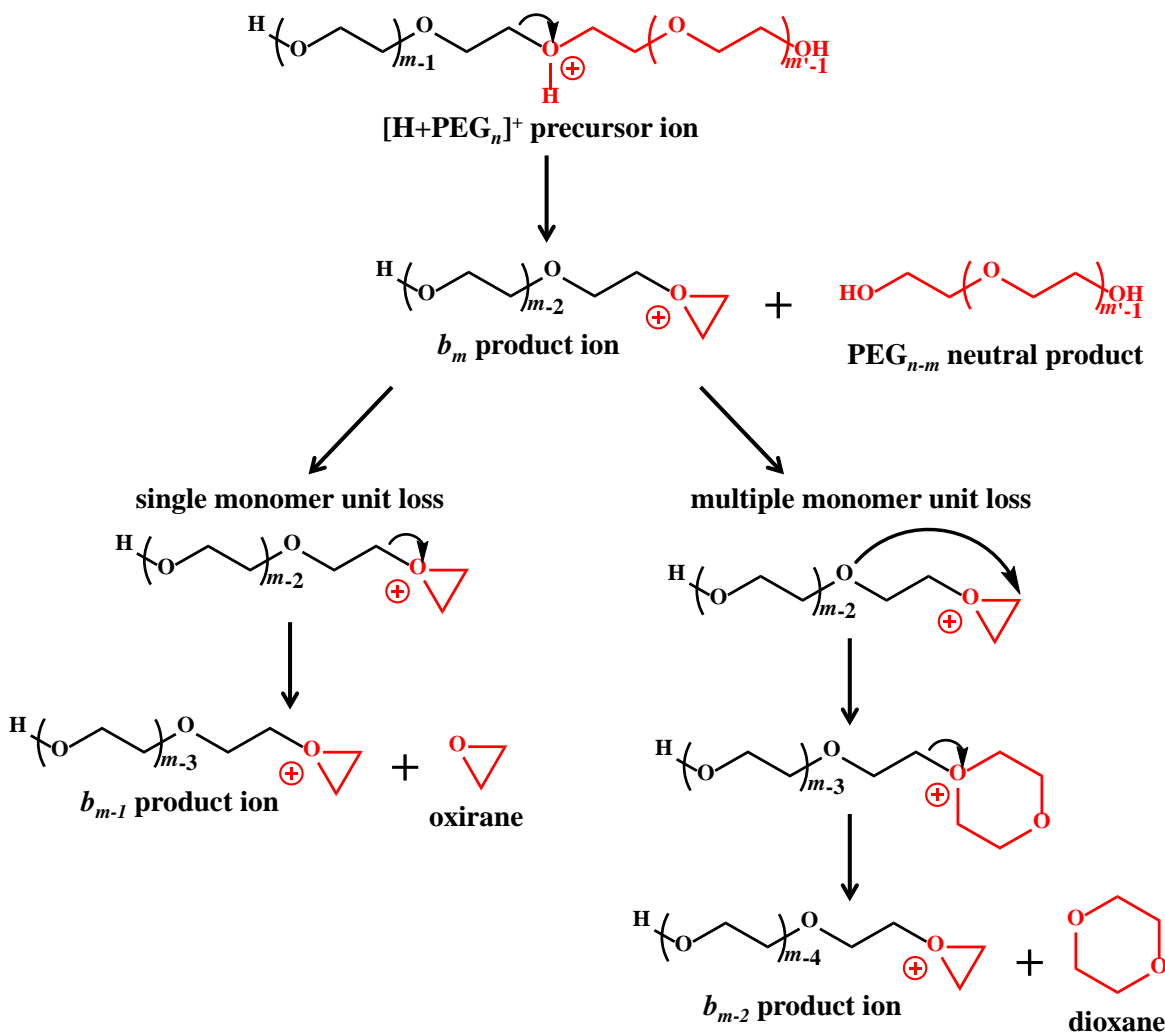


Figure 7.2 Schematic decomposition reactions for single and multiple monomer unit loss from [H+PEG<sub>n</sub>]<sup>+</sup> via the formation of cyclic intermediates. Bond cleavage adjacent to the positively charged oxygen atom yields a neutral cyclic ether and a smaller fragment ion. This reaction can repeat to yield multiple smaller fragments.

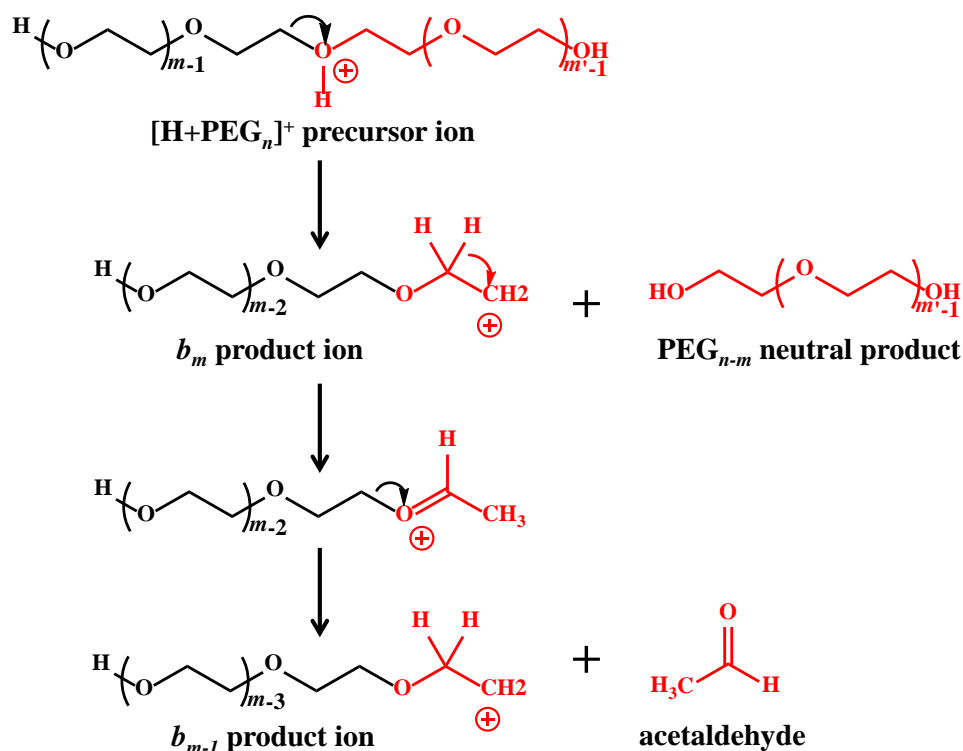


Figure 7.3 Alternative schematic decomposition reaction for single monomer unit loss from [H+PEG<sub>n</sub>]<sup>+</sup> via a 1,2-hydride shift. Bond cleavage adjacent to the positively charged oxygen atom yields neutral acetaldehyde and a smaller fragment ion.

*b*-type ions with a subscript *m*, where *m* is the number of monomeric units in the fragment ion.

Figure 7.4 shows favored formation of *b*<sub>1</sub> – *b*<sub>4</sub> ions with respective *m/z* of 45, 89, 133, and 177, according to the formula  $m/z = 44(m) + 1$ . The dissociation schemes in Figure 7.2 and Figure 7.3 show cleavage occurs adjacent to the charged site. Protonated precursor ions must undergo C–O bond cleavage to yield relatively short chain fragments. The formation of short chain fragment ions suggests the interior oxygen atoms along the backbone are preferentially protonated.

Sequential fragmentation proceeds either through ring formation followed by charge-adjacent cleavage, or through a hydride shift and C–O bond cleavage. Appearance energies for the dissociation reactions were obtained using ERMS, Figure 7.5. In-source fragmentation was carried out to confirm dissociation pathways, Figure 7.6.

### 7.3.1 Collision-Induced Dissociation

Representative CID spectra of  $[\text{H+PEG}_n]^+$  are shown in Figure 7.4. The spectra were recorded at a collision energy of 20 eV<sub>lab</sub>. All spectra show similar primary fragments at  $m/z$  45, 89, 133 and 177. The peaks are labeled by the number of remaining monomer units in the standard notation for polymers,<sup>12</sup>  $b_m$ , where the size of the fragment is indicated by the subscript according to the formula,  $m/z = 44(m) + 1$ . The fragments are primarily located at low mass, with little to no fragment intensity observed at masses near the precursor ion. This is especially noticeable for the  $n = 7 - 9$  spectra. The spectra are consistent with previously published CID spectra of  $[\text{H+PEG}_n]^+$ .<sup>2-4</sup> Because no high mass fragments are observed, the initial bond cleavage of  $[\text{H+PEG}_n]^+$  in either Figure 7.2 or 7.3 appears to favor the charge residing on the shorter fragment. This is somewhat unexpected, because the longer fragment will have a greater polarizability, which often helps stabilize excess charge. However, the same effect was observed in the earlier studies. Survey CID scans from 5 to 50 eV<sub>lab</sub> collision energy confirmed that high mass fragments are not generated under our experimental conditions.

### 7.3.2 Energy-Dependent Fragmentation

The primary fragments identified in Figure 7.4 were subsequently monitored as a function of collision energy. Representative scans for the  $b_1 - b_4$  fragments of  $[\text{H+PEG}_n]^+$ ,  $n = 4 - 9$ , are shown in Figure 7.5. All spectra were converted to the center-of-mass scale using the energy-transformation equation in Equation 2.1:  $E_{\text{cm}} = E_{\text{lab}} \times [\text{mass}_{\text{target}}/(\text{mass}_{\text{target}} + \text{mass}_{\text{ion}})]$ , where  $E_{\text{lab}}$  is the laboratory-frame collision energy in eV, corresponding to the applied collision cell voltage,  $\text{mass}_{\text{target}}$  is the mass of the argon collision gas, and  $\text{mass}_{\text{ion}}$  is the mass of the ion. The transformation to the center-of-mass scale allows a direct comparison of energetic trends for

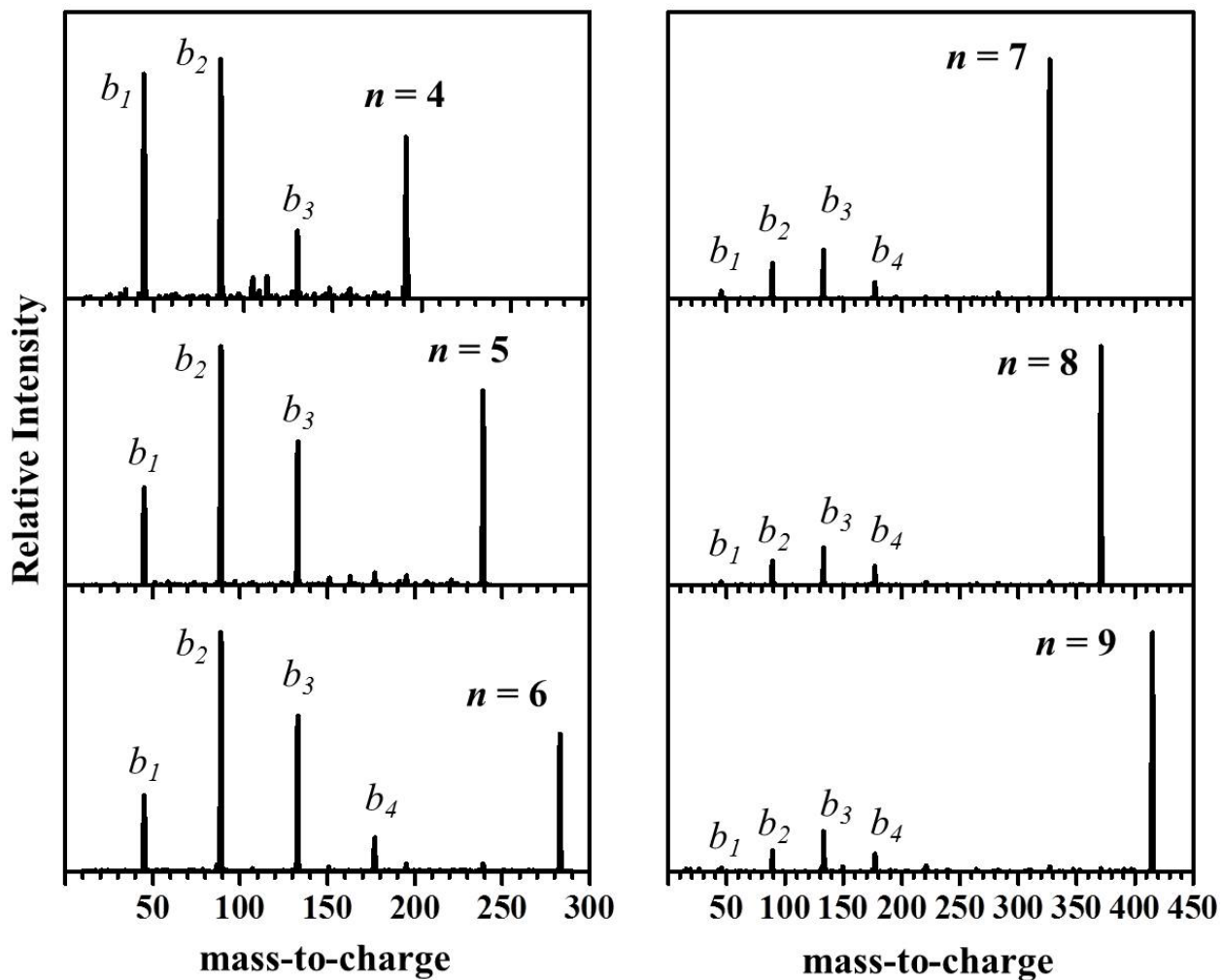


Figure 7.4 Representative CID spectra of  $[H+PEG_n]^+$ ,  $n = 4 - 9$ , at a collision energy of  $20 \text{ eV}_{\text{lab}}$ . The fragment ions, labeled as  $b_m$ , are located at regularly space intervals according to the equation  $m/z = m(44) + 1$ .

ions of different mass. In this experiment, we did not carry out a zero-kinetic energy adjustment of the lab-frame energy by a retarding potential analysis, so only relative differences of the energy dependence for each fragment can be made. However, the interesting information about sequential fragmentation dynamics lies in the relative energy differences and curve shapes as a function of collision energy. The threshold region is nominally related to the initial C–O bond dissociation energy, but for  $[\text{H+PEG}_n]^+$ , this is an average of the isomer population. Because the ions are mixtures of protonated isomers a quantitative threshold analysis of the data in Figure 7.5 is impossible, so that a retarding potential analysis, usually performed in these experiments, does not provide any new information.

The energy-dependent fragment intensities in Figure 7.5 show interesting behavior. For example, each fragment channel has approximately the same appearance energy and intensity maximum regardless of the size of the precursor ion. The shape of each curve for  $b_1 - b_4$  is also approximately the same regardless of the size of the precursor  $[\text{H+PEG}_n]^+$ . Only the comparison of relative intensities shows significant size-dependent trends. For example, the  $b_3$  curves, which have low relative intensity for  $n = 4$ , become more intense with increasing  $n$ . The source of the increased intensity is largely expected to arise from the increased statistical probability of forming large  $b_m$  fragments upon dissociation of a longer  $[\text{H+PEG}_n]^+$  precursor fragment. In contrast to the relative intensities, the characteristic curve energies do not change as the size of the ion increases. For example, the  $b_1$  fragment has an energy onset just below 2 eV for all  $[\text{H+PEG}_n]^+$ ,  $n = 4 - 9$ . The  $b_2$  fragment has an energy onset just above 1 eV and has a maximum between 3 and 3.5 eV, followed by a small loss of intensity. The higher mass fragments,  $b_3$  and  $b_4$ , both have the lowest energy onsets, around 1 eV, and a maximum between 2 and 3 eV. In

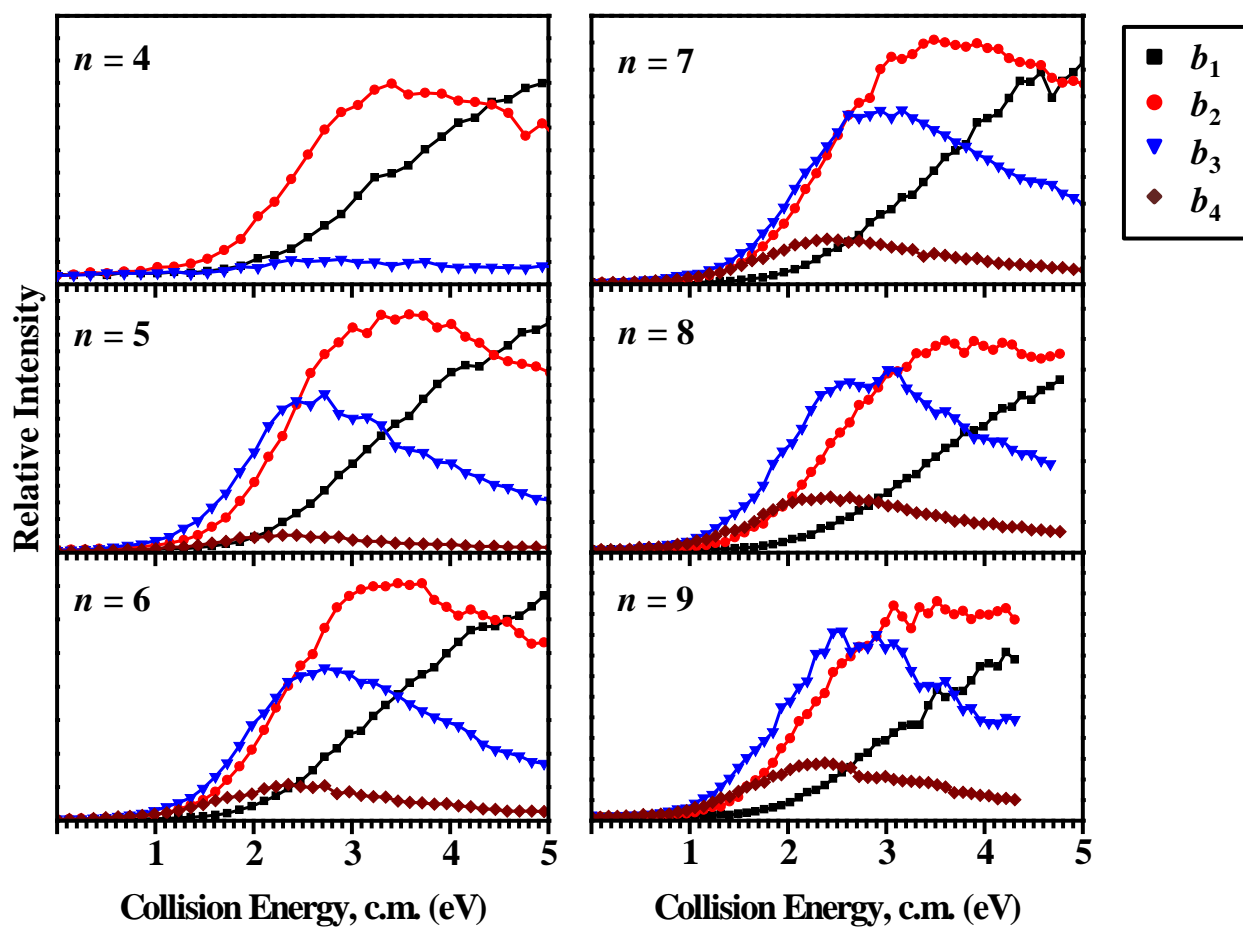


Figure 7.5 Representative ERMS studies of the fragments  $b_1$  to  $b_4$  from dissociation of  $[\text{H}+\text{PEG}_n]^+$ ,  $n = 4 - 9$ . The intensities reflect the relative intensities of each ion, and the collision energy scale is plotted in the center-of-mass frame.

general, higher mass fragments have onsets and curve maxima at the lowest energies. The loss of intensity with increasing collision energy indicates that sequential dissociation of larger fragments into lower mass channels becomes important.

### 7.3.3 In-Source Fragmentation

The data in Figure 7.5 confirm that fragments undergo sequential dissociation. However, the experiment does not reveal how many monomer units are lost in each sequential step. For example, sequential dissociation of the  $b_4$  fragment could yield  $b_3$ ,  $b_2$ ,  $b_1$ , or a mixture of all three, but we cannot identify how many dissociation steps a given fragment has experienced. This information is crucial evidence for the two different mechanisms in Figure 7.2 and Figure 7.3. In order to measure the mass difference in each sequential step, we carried out in-source fragmentation as detailed in Chapter 2 to generate the  $b_m$  fragments. This allows the selection of a direct fragment,  $b_m$ , before it undergoes sequential dissociation. Any fragments formed by CID of  $b_m$  are sequential, and there is no corresponding interference from a direct dissociation of the precursor  $[\text{H}+\text{PEG}_n]^+$  isomer. Unlike the CID spectra in Figure 7.4, where each  $b_m$  is formed through a complex series of direct and sequential reactions from a mixture of  $[\text{H}+\text{PEG}_n]^+$  isomers, in-source fragmentation removes the  $[\text{H}+\text{PEG}_n]^+$  isomers from the problem. Mass selection of the  $b_2 - b_5$  fragments, followed by CID, yields the spectra shown in Figure 7.6 at 10 eV<sub>lab</sub>. These experiments show small fragment ions,  $b_2$  and  $b_3$ , undergo the loss of a single monomer unit,  $\Delta b_m = -1$ , because the most intense fragment is 44  $m/z$  units less than the precursor mass. In contrast, fragmentation of  $b_4$  and  $b_5$  yielded low abundance fragments corresponding to the loss of a single monomer unit, but they do yield an intense fragment corresponding to the loss of two monomer units,  $\Delta b_m = -2$ .<sup>2</sup>

#### 7.4 Discussion

The CID spectra in **Figure 7.4** only provide general information about the possible mechanisms of dissociation of  $[\text{H}+\text{PEG}_n]^+$  and cannot yield detailed information due to several limitations. The limiting factor for all experiments utilizing  $[\text{H}+\text{PEG}_n]^+$  is the isomer mixture upon ionization. This mixture yields a distribution of initial carbocation fragments with different lengths. Each different fragment can subsequently dissociate sequentially to yield secondary fragments, but those are located at the same masses as the original direct fragments. The mixture should be a statistical representation of the total number of unique protonation sites, and because oxygen atoms at all positions are similar, the proton affinities at most sites should also be nearly identical. Both possible mechanisms, Figure 7.2 and Figure 7.3, begin with the C–O bond cleavage at a protonation site. The difference between the two possible reactions is the sequential decomposition step. However, if fragments are formed from both direct and sequential processes from a mixture of isomers, how does one learn anything about the dissociation mechanisms? Clearly, CID experiments carried out at one collision energy are insufficient to obtain any detailed mechanistic data. We used two approaches to gain more insight into the processes of  $[\text{H}+\text{PEG}_n]^+$  dissociation. The energy-dependent fragmentation experiment provides information about the relative energetics, but is blind to the fundamental unimolecular dissociation steps. Despite this limitation, which is also a problem in CID analysis, energy-dependent fragmentation spectra in Figure 7.5 are helpful. One of the most important outcomes from energy-dependent measurements is the relative trend in the average appearance energy of a  $b_m$  fragment and the maximum intensity of each  $b_m$  curve as a function of oligomer size. For the four different fragments that were monitored, the appearance energy is lowest for  $b_4$  and increases with decreasing size to  $b_1$ . This trend shows that larger fragments are formed in

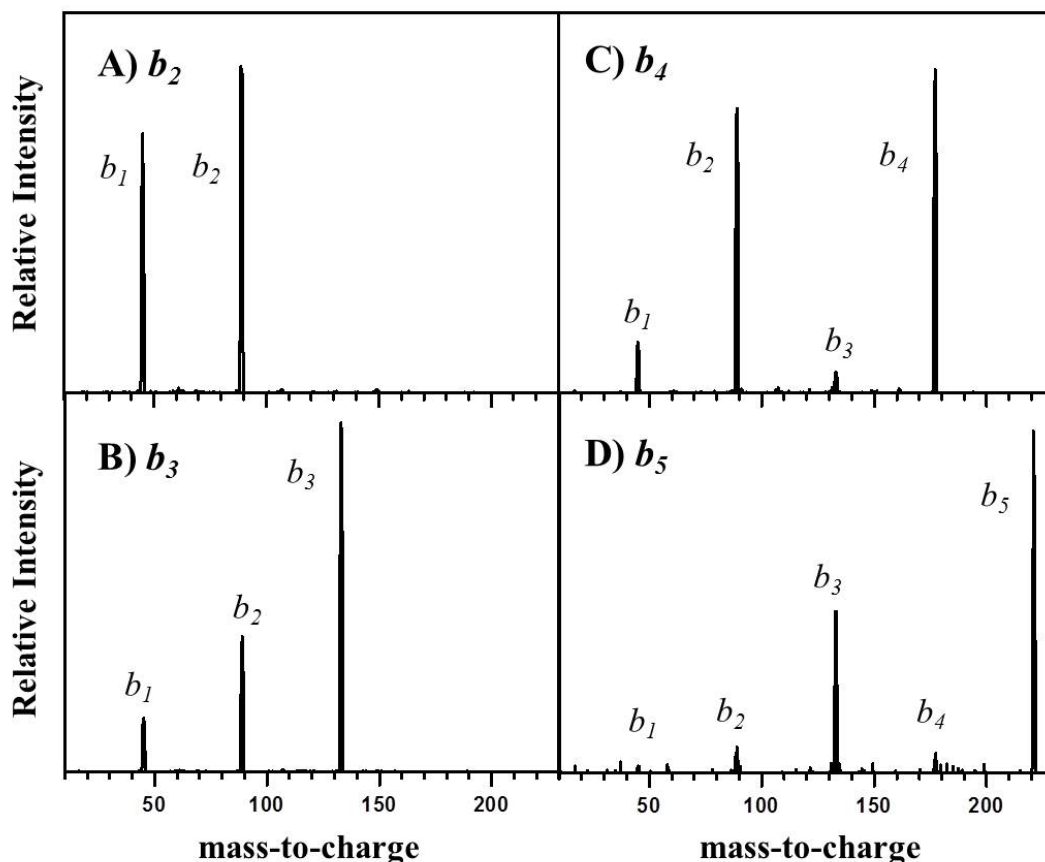


Figure 7.6 Representative CID spectra of the fragment ions,  $b_2 - b_5$  at  $10 \text{ eV}_{\text{lab}}$ . The ions were generated by in-source dissociation of  $[\text{H}+\text{PEG}_n]^+$ . The precursor ions A)  $b_2$ , B)  $b_3$ , C)  $b_4$ , and D)  $b_5$  and their fragment ions are labeled in each spectrum.

greater yield at low collision energy and then undergo sequential dissociation to yield smaller species. As the collision energy increases, the smaller fragments rapidly gain intensity both by direct dissociation of  $[\text{H}+\text{PEG}_n]^+$  and by sequential dissociation from a larger fragment. Even though the analysis of the spectra in Figure 7.5 is limited by the isomer distribution, some useful information can be extracted. For example, the  $b_3$  curve maximum is located at an energy where the  $b_2$  curve is undergoing a rapid increase in intensity, and the  $b_2$  curve has a maximum at an energy where the  $b_1$  curve also has its most rapid increase in intensity. This intensity profile suggests that each  $b_m$  decays sequentially by the loss of a single monomer unit. Of course, these are only crude correlations because the curves are very broad and do not prove that  $b_3$  decays into  $b_2$  and then into  $b_1$ , but the trends are suggestive of the dynamics.

The energy-dependent measurements also provide an indication of the relative rate at which sequential decomposition occurs. For example, if the sequential rates of dissociation are slow relative to direct dissociation on the time scale of the experiment, then most fragments should form via the direct process, and a rapid decrease in fragment intensities would not be observed. In Figure 7.5, the relatively rapid loss of intensity for the  $b_3$  and  $b_4$  fragments, even at low collision energy, indicates that sequential dissociation is a major process leading to the formation of  $b_1$  and  $b_2$ . Previous CID experiments were unable to determine the extent to which sequential dissociation is a factor in the final fragment intensities. The energy-dependent fragmentation experiments, however, have demonstrated that sequential dissociation is important at all collision energies. This implies that the rates for sequential dissociation are fast.

Although the energy-dependent experiment provides additional insight into the fragmentation dynamics of  $[\text{H}+\text{PEG}_n]^+$ , it was unable to identify the size change in sequential unimolecular decay. The size of the neutral loss in sequential dissociation is a key experimental factor needed to provide additional evidence for one of the mechanisms in Figure 7.2 and Figure 7.3. The in-source fragmentation study shows that smaller  $b_m$  fragments undergo sequential dissociation by the loss of a single monomer unit, Figure 7.6. This can only occur by the loss of ethylene oxide, or by the loss of acetaldehyde. Whereas the ethylene oxide product follows the same cyclization pathways of Figure 7.2, the high strain of the product and tight transition state should make this process slow, and a large energy barrier is expected on the potential energy surface. In contrast, the hydride shift followed by loss of acetaldehyde is not limited by a high energy transition state, strain, and is known to be a fast rearrangement for carbocations. The product from the hydride shift pathway, acetaldehyde, is less strained than ethylene oxide and is the thermodynamically favored product of the two possible  $\text{C}_2\text{H}_4\text{O}$

products. Therefore, of the two possible routes to the loss of  $C_2H_4O$  from  $b_m$ , the loss of acetaldehyde should dominate over the formation of ethylene oxide. However, as Figure 7.6 also shows, the unexpected finding of this study is that both mechanisms suggested in Figure 7.2 and Figure 7.3 must contribute to the sequential dissociation process. The larger fragments were observed to lose two monomer units ( $b_4 \rightarrow b_2$  and  $b_5 \rightarrow b_3$ ) with very little fragment intensity corresponding to the loss of one monomer unit. This is consistent with the original proposal of the loss of 1,4-dioxane in Figure 7.2. One reason for the change in fragmentation could be that larger fragments more easily form six-membered ring intermediate structures, such as those shown in Figure 7.2, due to the lower strain of the six-membered ring compared to the three-membered ring. Such an intermediate could be stabilized in the in-source fragmentation process. Unfortunately, a companion theoretical study of even a medium-sized oligomer is outside the scope of the current work due to the extremely large conformational space and multiple protonated isomers that must be calculated. Such an analysis would take us too far afield of the intentions of this current study, whose primary focus was to obtain additional experimental data on the sequential dissociation dynamics of  $[H+PEG_n]^+$ .

### 7.5 Conclusions

In this work, we carried out a series of studies on  $[H+PEG_n]^+$  dissociation to learn about the sequential fragmentation mechanisms. Energy-dependent fragmentation experiments showed that sequential fragmentation is a major process at all collision energies. We used in-source fragmentation to generate authentic fragment ions that are observed in CID of  $[H+PEG_n]^+$ . Dissociation of those ions indicated that sequential dissociation occurs by at least two different processes, including a hydride shift rearrangement. Thus, the previously accepted picture of

$[H+PEG_n]^+$  dissociation via cyclization reactions should be revised to account for the additional possibility of a 1,2-hydride shift and loss of acetaldehyde.

## 7.6 References

- [1] Hester, T.H.; McCraney, K.K.; Castillo, D.E.; Goebbert, D.J. The Sequential Dissociation of Protonated Polyethylene Glycols. *J. Mass Spectrom.* **2013**, *48* (4), 459-464.
- [2] Selby, T.L.; Wesdemiotis, C.; Lattimer, R.P. Dissociation Characteristics of  $[M + X]^+$  Ions (X = H, Li, Na, K) from Linear and Cyclic Polyglycols. *J. Am. Soc. Mass Spectrom.* **1994**, *5* (12), 1081-1092.
- [3] Lattimer, R.P. Tandem Mass Spectrometry of Poly(ethylene glycol) Proton- and Deuteron-attachment Ions. *Int. J. Mass Spectrom.* **1992**, *116* (1), 23-36.
- [4] Kalinoski, H.T.; Hargiss, L.O. Collision-induced Dissociation Mass Spectrometry of Nonionic Surfactants Following Direct Supercritical Fluid Injection. *J. Am. Soc. Mass Spectrom.* **1992**, *3* (2), 150-158.
- [5] Jackson, A.T.; Scrivens, J.H.; Williams, J.P.; Baker, E.S.; Gidden, J.; Bowers, M.T. Microstructural and Conformational Studies of Polyether Copolymers. *Int. J. Mass Spectrom.* **2004**, *238* (3), 287-297.
- [6] Gidden, J.; Wyttenbach, T.; Batka, J.J.; Weis, P.; Jackson, A.T.; Scrivens, J.H.; Bowers, M.T. Poly (Ethylene Terephthalate) Oligomers Cationized by Alkali Ions: Structures, Energetics, and Their Effect on Mass Spectra and the Matrix-Assisted Laser Desorption/Ionization Process. *J. Am. Soc. Mass Spectrom.* **1999**, *10* (9), 883-895.
- [7] Gidden, J.; Wyttenbach, T.; Jackson, A.T.; Scrivens, J.H.; Bowers, M.T. Gas-Phase Conformations of Synthetic Polymers: Poly(ethylene glycol), Poly(propylene glycol), and Poly(tetramethylene glycol). *J. Am. Chem. Soc.* **2000**, *122* (19), 4692-4699.
- [8] Wyttenbach, T.; von Helden, G.; Bowers, M.T. Conformations of Alkali Ion Cationized Polyethers in the Gas Phase: Polyethylene Glycol and Bis[(benzo-15-crown-5)-15-ylmethyl] Pimelate. *Int. J. Mass Spectrom.* **1997**, *165*, 377-390.
- [9] von Helden, G.; Wyttenbach, T.; Bowers, M.T. Conformation of Macromolecules in the Gas Phase: Use of Matrix-Assisted Laser Desorption Methods in Ion Chromatography. *Science*. **1995**, *267* (5203), 1483-1485.
- [10] von Helden, G.; Wyttenbach, T.; Bowers, M.T. Inclusion of a MALDI Ion Source in the Ion Chromatography Technique: Conformational Information on Polymer and Biomolecular Ions. *Int. J. Mass Spectrom.* **1995**, *146*, 349-364.

- [11] Seyfried, B.K.; Siekmann, J.; Belgacem, O.; Wenzel, R.J.; Turecek, P.L.; Allmaier, G. MALDI Linear TOF Mass Spectrometry of PEGylated (glyco)proteins. *J. Mass Spectrom.* **2010**, *45* (6), 612-617.
- [12] Wesdemiotis, C.; Solak, N.; Polce, M.J.; Dabney, D.E.; Chaicharoen, K.; Katzenmeyer, B.C. Fragmentation Pathways of Polymer Ions. *Mass Spectrom. Rev.* **2011**, *30* (4), 523-559.
- [13] Wu, J.; Polce, M.J.; Wesdemiotis, C. Unimolecular Chemistry of Li<sup>+</sup>- and Na<sup>+</sup>-Coordinated Polyglycol Radicals, a New Class of Distonic Radical Cations. *J. Am. Chem. Soc.* **2000**, *122* (51), 12786-12794.
- [14] Alvarez, E.J.; Wu, H.-F.; Liou, C.-C.; Brodbelt, J. Collisionally Activated Dissociation of Transition Metal Ion/Polyether Complexes in a Quadrupole Ion Trap. *J. Am. Chem. Soc.* **1996**, *118* (38), 9131-9138.
- [15] Wu, H.-F.; Brodbelt, J.S. Gas-Phase Complexation of Monopositive Alkaline Earth Metal Ions with Polyethers: Comparison with Alkali Metal Ion and Aluminum Ion Complexations. *J. Am. Chem. Soc.* **1994**, *116* (14), 6418-6426.
- [16] Liou, C.C.; Wu, H.F.; Brodbelt, J.S. Hydrogen-bonding Interactions in Gas-phase Polyether/Ammonium Ion Complexes. *J. Am. Soc. Mass Spectrom.* **1994**, *5* (4), 260-273.
- [17] Maleknia, S.; Brodbelt, J. Cavity-size-dependent Dissociation of Crown Ether/Ammonium Ion Complexes in the Gas Phase. *J. Am. Chem. Soc.* **1993**, *115* (7), 2837-2843.
- [18] Liou, C.C.; Brodbelt, J.S. Comparison of Gas-phase Proton and Ammonium Ion Affinities of Crown Ethers and Related Acyclic Analogs. *J. Am. Chem. Soc.* **1992**, *114* (17), 6761-6764.
- [19] Liou, C.-C.; Brodbelt, J.S. Determination of Orders of Relative Alkali Metal Ion Affinities of Crown Ethers and Acyclic Analogs by the Kinetic Method. *J. Am. Soc. Mass Spectrom.* **1992**, *3* (5), 543-548.
- [20] Lattimer, R.P. Tandem Mass Spectrometry of Poly(ethylene glycol) Lithium-attachment Ions. *J. Am. Soc. Mass Spectrom.* **1994**, *5* (12), 1072-1080.
- [21] Loudon, G.M.: *Organic Chemistry*, Benjamin/Cummings Pub. Co., Redwood City, CA, 1995.
- [22] Holmes, J.L.; Aubry, C.; Mayer, P.M.: *Assigning Structures to Ions in Mass Spectrometry*, CRC Press, Boca Raton, FL, 2007.
- [23] Babcock, L.M.; Adams, N.G.: *Advances in Gas Phase Ion Chemistry*, Elsevier Science, Greenwich, CT, 2001.

## CHAPTER 8

### DEPROTONATED POLYETHYLENE GLYCOL

Studies were carried out on samples of polyethylene glycol, PEG and were the earliest in the author's research timeline. These studies became a cornerstone for how mass spectrometry data were collected and displayed, and what experimental and theoretical methods would be used to analyze future chemical systems. The findings were published in 2013 as an article in the journal *Rapid Communications in Mass Spectrometry*.<sup>1</sup>

Polyethylene glycols, PEGs, are soluble molecules utilized in a wide range of applications. Mass spectrometry and fragmentation patterns of positively charged PEG oligomers are well-known, but decomposition mechanisms of the deprotonated ions have not been studied. Deprotonated PEGs were generated by electrospray ionization of PEG in water/acetonitrile. Collision-induced dissociation, CID, experiments were carried out in a tandem mass spectrometer. The anions were studied using a tandem mass spectrometer to carry out CID experiments. A series of small PEG oligomers, with 1 to 8 monomer units, were studied in order to monitor size-dependent effects on fragmentation reactions.

Because deprotonated PEG ions have a unique charge site, their dissociation pathways can easily be monitored. The ions fragment by loss of  $C_2H_4O$  monomer units, with an alternating intensity pattern that suggests the loss of an even number of monomer units is favored. Smaller oligomers and oligomer fragments also yielded fragments corresponding to  $H_2$  elimination and  $H_2O$  loss. Elimination of  $H_2$  occurs by the generation of a hydride ion which deprotonates an alcohol upon leaving, whereas dehydration appears to be a charge-remote

process. The fragmentation of deprotonated PEG is dominated by intramolecular  $S_N2$  reactions involving the terminal oxide anion.

### 8.1 Introduction

The development of electrospray ionization, ESI, and matrix-assisted laser desorption/ionization as routine methods for generating high molecular weight ions has allowed the development of mass spectrometry methods for analyzing complex mixtures, such as those containing polymers. High-resolution mass spectrometry is useful for determining average molecular weight and composition,<sup>2-5</sup> whereas more advanced methods, such as CID, can yield structure and sequence information.<sup>2,6-8</sup> Monomer structure and end-group functionalities of polymers often determine the most appropriate method for ion generation. Lewis base groups incorporated into a monomer attach protons, molecular, or metal cations and form singly or multiply charged ions,<sup>9</sup> whereas species with acidic groups lose protons to form negative ions. After ion formation, intramolecular interactions such as ion-dipole interactions or hydrogen bonding determine the solution and gas-phase ion structures,<sup>10-16</sup> which may be different. In general, it is easy to generate positively charged polymers or polymer complexes of species with Lewis base sites, and nearly all fragmentation studies of polymers, oligomers and macromolecular compounds have focused on analyzing positively charged species.<sup>9</sup> However, positive ion complexes with large molecules have fundamental challenges because of the nature of cation binding. For example, in protonated species, the proton may be located at many different, but nearly equivalent positions. This produces a large number of isomers for each mass.<sup>17-22</sup> However, every isomer produces a unique fragmentation pattern, so the composite

spectrum from dissociation of a cation complex is challenging to analyze. Additional problems may include scrambling of the charge prior to dissociation of an energized compound.

An ideal experiment would differentiate the isomers prior to analysis, perhaps by ion-mobility methods, or would employ methods that generate only one isomer. One possible approach to achieve single isomer generation is through chemical methods, such as deprotonation. For example, deprotonation generally occurs at the most acidic position, and, if a polymer has only one highly acidic proton, then negative ions generated by deprotonation will produce fragmentation spectra representative of that single isomer. Although such an approach is not suitable for every system, a large number of species are available that meet this requirement. Deprotonated PEG is a good example of a system where chemical methods can be used to generate a single isomer because there are only two acidic positions, the terminal alcohols. Even though there are two acidic positions at the termini of normal PEG molecules, they are chemically equivalent, so deprotonation generates a single negative ion isomer. The aim of the present study was to investigate negative-ion ESI and fragmentation reactions of deprotonated PEG starting with ethylene glycol as a function of oligomer length. The negative ion charge may also open new dissociation reactions that are not observed in cation complex, which could be useful for structure and sequence analysis.

These results are compared with the fragmentation spectra of protonated PEG, and several important differences are immediately evident. This study demonstrates that negative ion fragmentation may have a greater potential for analysis of PEGs because the dissociation spectrum is free from multiple isomers but yields a large number of fragment ions.

## 8.2 Methods

All chemicals were purchased from VWR International (Randor, PA, USA) and used without purification. Separate solutions of each PEG<sub>*n*</sub> oligomer were prepared for  $n = 1 - 8$  (99% pure, VWR) at a 1 mM concentration in 1:1 (volume/volume) ratio of HPLC-grade solvents, acetonitrile and water. No base was added to the solution, and anions are presumably formed by the natural acidity of PEG<sub>*n*</sub> in solution. All experiments were carried out using a TSQ-7000 tandem mass spectrometer (Finnigan MAT, San Jose, CA, USA) operating with the Excalibur software program.

## 8.3 Results and Discussion

Representative CID mass spectra of deprotonated PEG<sub>*n*</sub> ( $n = 1 - 8$ ) are shown in Figure 8.1. The spectra were recorded with an offset voltage of 30 eV applied to the octopole collision cell. The intensity scale has been expanded to show the relative intensity of the fragment ions. The major fragments appear at regular intervals according to the function:  $m/z = m(44) + 17$ , where  $m$  is the number of monomer units remaining in the fragment. We use the notation,  $b_m$ , to indicate the fragment size as a function of the number of monomer units.<sup>9</sup> Fragmentation of deprotonated ethylene glycol,  $n = 1$ , yielded only a single low-intensity fragment at  $m/z$  17, corresponding to OH<sup>-</sup>. Dissociation of deprotonated diethylene glycol,  $n = 2$ , yielded a fragment at  $m/z$  61,  $b_1$ , and a second fragment at  $m/z$  59 with low abundance. Upon dissociation of [PEG<sub>3</sub> - H]<sup>-</sup>, the  $b_1$  fragment is the most abundant, whereas the  $b_2$  fragment has very low relative abundance. The  $m/z$  59 peak was also detected in the CID spectrum of [PEG<sub>3</sub> - H]<sup>-</sup>. Only for [PEG<sub>4</sub> - H]<sup>-</sup>,  $n = 4$ , and higher values of  $n$  were multiple  $b_m$  ions observed in high relative abundance in the CID spectrum. Upon decomposition of [PEG<sub>4</sub> - H]<sup>-</sup>, all three smaller

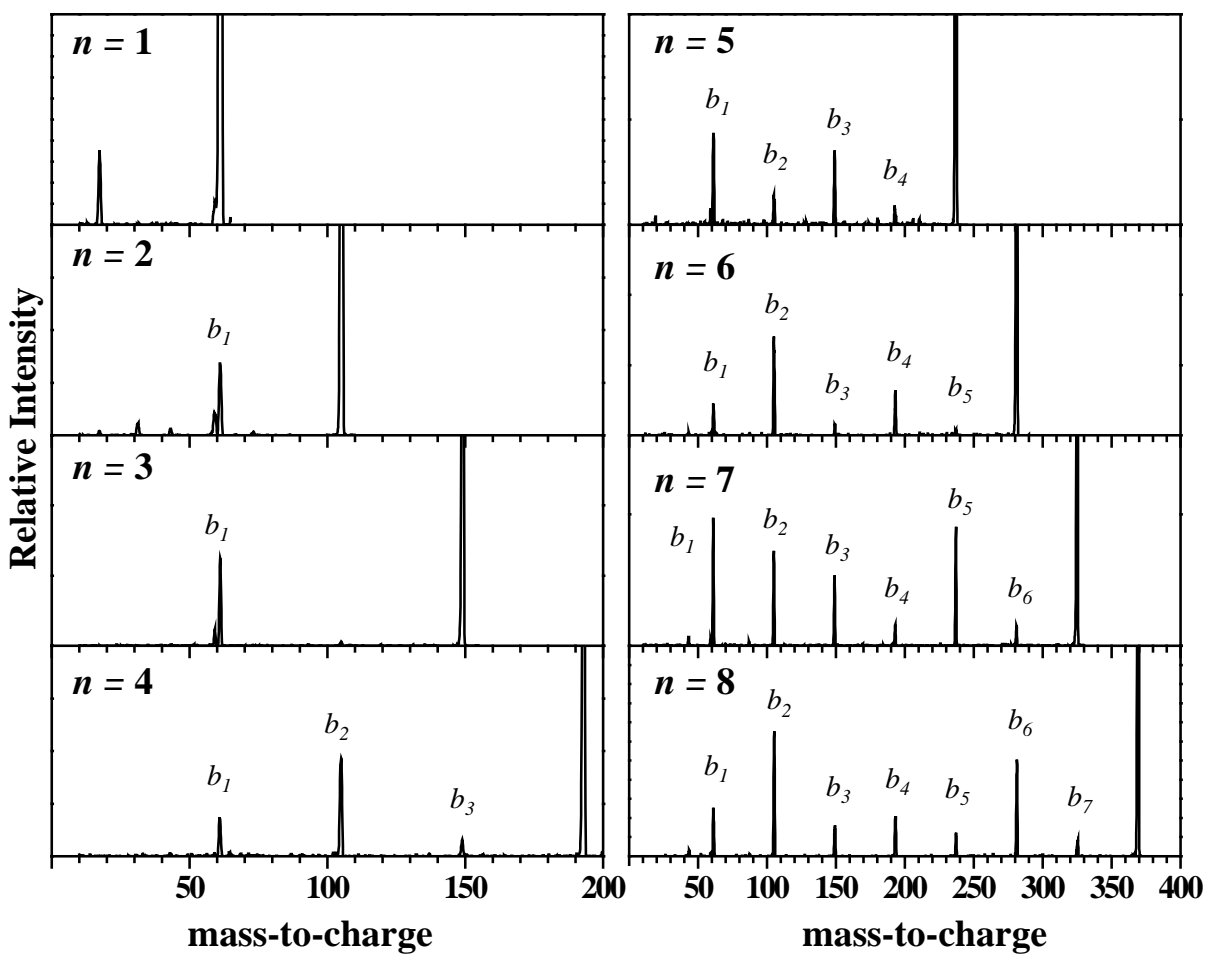


Figure 8.1 Negative-ion CID spectra of deprotonated PEG,  $[\text{PEG}_n - \text{H}]^-$  ( $n = 1 - 8$ ). All spectra were recorded at 30 eV collision energy, lab-frame, with argon collision gas at a pressure of 0.20 mTorr.

fragments,  $b_1 - b_3$ , are detected, and  $b_2$  is the most intense product. Upon dissociation of the longer  $[\text{PEG}_n - \text{H}]^-$  oligomers, all possible fragment sizes,  $b_1 - b_{n-1}$ , were detected. The precursor ions,  $n = 4 - 8$ , produced alternating intensity patterns in their CID spectra. If  $n$  is an even number in the precursor  $[\text{PEG}_n - \text{H}]^-$ , then even-numbered  $b_m$  fragments tend to have greater relative intensity compared to odd-numbered  $b_m$  fragments, whereas, if  $n$  is odd, then odd  $b_m$  fragments have greater intensity than even-numbered  $b_m$  fragments.

The CID spectra of deprotonated PEG are considerably different from the well-known spectra of the protonated compounds,  $[\text{H}+\text{PEG}_n]^+$ .<sup>17,18,20,23</sup> Example CID spectra for similarly sized  $[\text{H}+\text{PEG}_n]^+$  precursor ions were shown in Figure 7.4. Dissociation of  $[\text{H}+\text{PEG}_n]^+$  yields primary fragments at low mass with little to no product ion intensity near the precursor ion peak.<sup>17</sup> The spacing between each peak is 44  $m/z$  units, corresponding to the size of a single monomer unit, but, unlike the deprotonated  $\text{PEG}_n$  CID spectra, there is no alternation of peak intensities for even- or odd-sized oligomer fragments. The fragment peaks from  $[\text{H}+\text{PEG}_n]^+$  are located at  $m/z = m(44) + 1$ , which is a difference of 16  $m/z$  units compared to the positions of the anion peaks. This is due to an additional terminal oxygen atom in the anions. The fragments from dissociation of  $[\text{H}+\text{PEG}_n]^+$  are also labeled by the number of monomer units in the cation,  $b_m$ , but the differences between cations and anions should be carefully noted. One reason for the different appearance between protonated and deprotonated oligomer CID spectra arises from precursor ion structure. Protonated PEG is generated as a mixture of multiple isomers because the proton can be located on any oxygen atom along the molecule. In contrast, deprotonated PEG has only one isomer due to the loss of a proton from a terminal alcohol group. Another difference with negative ions is the relatively high abundance of the  $b_m$  fragment ions in Figure 8.1 compared to the relative intensity of the  $[\text{H}+\text{PEG}_n]^+$  precursor. Dissociation of the

anions under similar conditions yields only very low-intensity fragments. The high fragment intensities for protonated species imply that fragmentation rates of  $[\text{H}+\text{PEG}_n]^+$  are fast, whereas those of  $[\text{PEG}_n - \text{H}]^-$  are slower under the conditions used in this experiment.

The mechanism of protonated PEG dissociation has been studied in detail previously and by our group.<sup>17,18,20,23</sup> The molecules initially undergo C-O bond cleavage at the protonation site to generate a short neutral PEG and an unstable primary carbocation. Assuming protons are evenly distributed along the precursor backbone, the average length of the primary carbocation fragment is expected to be approximately half the length of the precursor ion. However, the carbocation is an unstable intermediate that readily undergoes rapid sequential decomposition reactions, either by cyclization and loss of a cyclic ether fragment in Figure 7.2, or by a hydride shift and loss of acetaldehyde in Figure 7.3. The secondary structure of the ions may also influence fragmentation, but this is difficult to determine by CID. Both routes allow the loss of multiple monomer units leading to the product ion masses in the CID spectra. Due to sequential decomposition of the initial fragment ions, most fragments in Figure 7.4 are located at low mass, in the size range from  $b_1$  to a maximum of  $b_{n/2}$ , where  $n$  is the length of the initial PEG ion.

Unlike protonated PEG, deprotonated  $\text{PEG}_n$  yields products with a wide range of sizes, from  $b_1$  to  $b_{n-1}$ . The relative intensity of  $b_{n-1}$  is extremely low in all spectra, whereas the relative intensity of the  $b_{n-2}$  fragment is always significantly higher, and is often one of the most intense peaks in the spectrum. Peaks that correspond to loss of an even number of monomer units tend to have a greater relative intensity compared to peaks corresponding to loss of an odd number of monomer units. The intensity pattern implies that the dissociation mechanism of  $[\text{PEG}_n - \text{H}]^-$  should incorporate the preferential loss of even numbers of monomer units. The preferential loss of two monomer units corresponds to elimination of 1,4-dioxane, the same type of six-membered

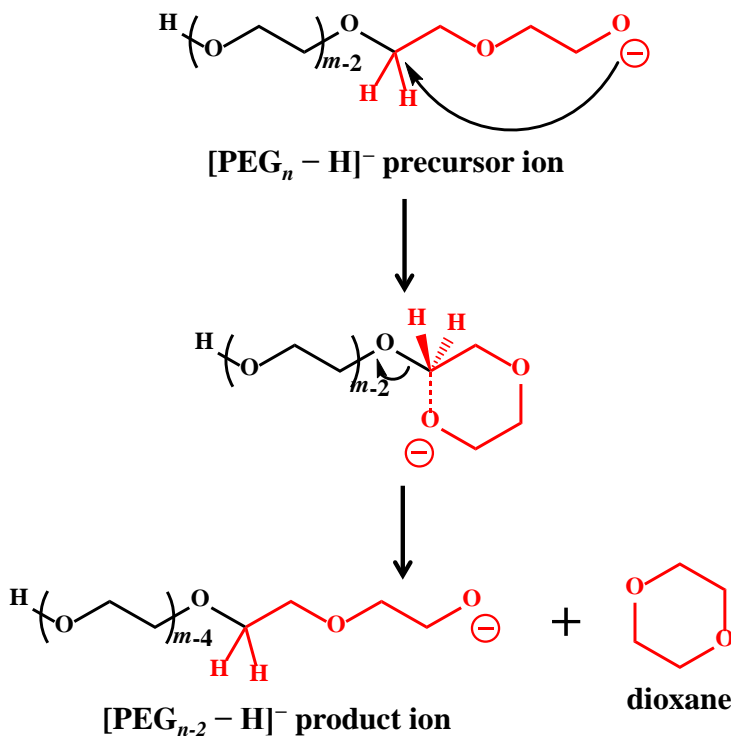


Figure 8.2 Schematic decomposition reaction for multiple monomer unit loss from  $[\text{PEG}_n - \text{H}]^-$  via the formation of a cyclic intermediate. Cleavage at the external C-O bond of the cyclic moiety yields a neutral cyclic ether and a smaller anion fragment. This reaction can repeat to yield ever smaller fragments.

cyclic fragment proposed in  $[\text{H} + \text{PEG}_n]^+$  dissociation, Figure 7.2. The most direct route to elimination of 1,4-dioxane from  $[\text{PEG}_n - \text{H}]^-$  is an intramolecular  $\text{S}_{\text{N}}2$  reaction by attack of the terminal oxide at an interior carbon atom as indicated in Figure 8.2. The reaction mechanism shown in Figure 8.2 illustrates the process for a six-membered ring, but any  $3x$ -membered ring ( $x = 1, 2, \dots$ ) could conceivably form. The low ring strain of 1,4-dioxane compared to larger or smaller rings favors elimination of 1,4-dioxane over other cyclic compounds such as ethylene oxide or 1,4,7-trioxane. Elimination of 1,4-dioxane from  $[\text{PEG}_n - \text{H}]^-$  generates a nascent  $b_{n-2}$  fragment, but if the ion has sufficient internal energy remaining, it can continue to undergo further elimination reactions. The favorable structures corresponding to 1,4-dioxane elimination produce the alternating intensity pattern observed in Figure 8.1, whereas random deviation allows the introduction of the odd series of peaks in the spectrum.

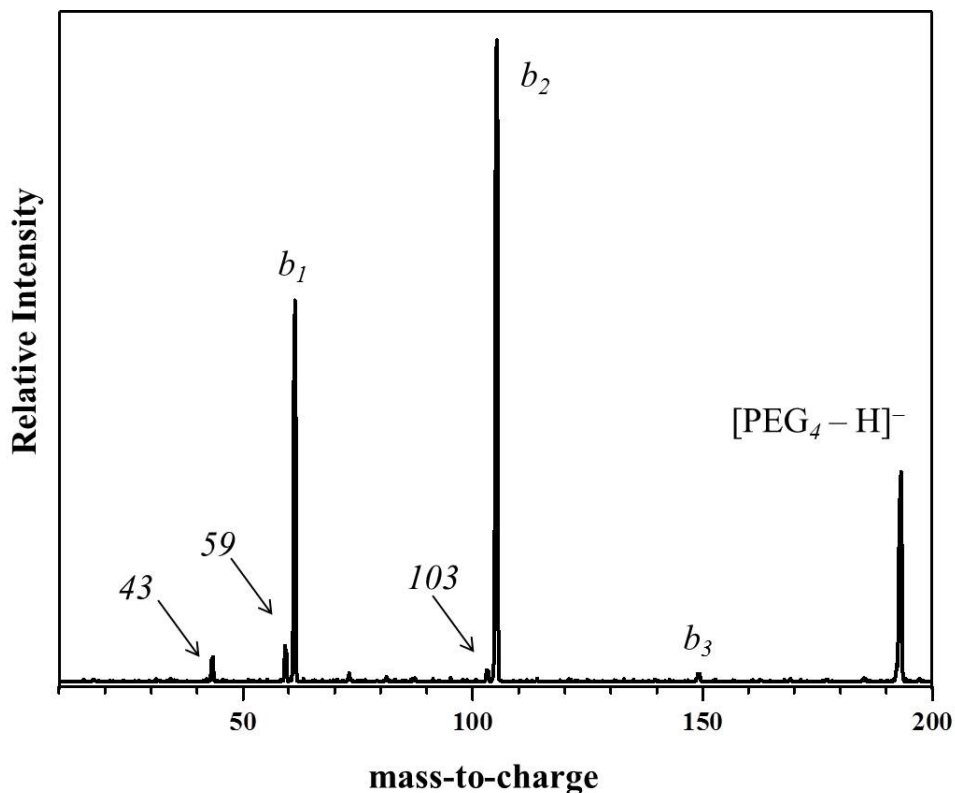


Figure 8.3 Negative-ion CID of  $[\text{PEG}_4 - \text{H}]^-$  at  $30 \text{ eV}_{\text{lab}}$  with  $1.00 \text{ mTorr}$  argon collision gas.

Although the process of dissociation in  $[\text{H}+\text{PEG}_n]^+$  is fundamentally different from  $[\text{PEG}_n - \text{H}]^-$ , it is interesting that both species share the common elimination of 1,4-dioxane. As indicated in Figure 7.2, the primary carbocation formed upon dissociation of protonated PEG can undergo cyclization followed by the sequential loss of 1,4-dioxane or other cyclic species. However, this reaction only occurs after the initial C-O bond cleavage. Deprotonated PEG also eliminates 1,4-dioxane, but this reaction occurs directly from the precursor ion. In both cases, 1,4-dioxane elimination reactions require a terminal charge site.

The primary fragments in the CID spectra of deprotonated PEG arise from the loss of monomers, but other dissociation reactions were also observed. The appearance of  $m/z$  59 in the CID spectra of  $[\text{PEG}_n - \text{H}]^-$ ,  $n = 2 - 4$ , suggests that smaller fragment ions eliminate  $\text{H}_2$  from  $b_1$ . The weak channels could be enhanced slightly by increasing the pressure in the collision cell, presumably due to multiple collisions. Figure 8.3 shows the CID spectrum of  $[\text{PEG}_4 - \text{H}]^-$  at

higher pressure. In addition to  $m/z$  59, fragments at  $m/z$  103 and  $m/z$  43 were detected. The  $m/z$  103 fragment corresponds to the elimination of  $H_2$  from the  $b_2$  fragment. The loss of  $H_2$  is an interesting process, and has been observed as a product in the ion-molecule reaction of  $OH^-$  with ethylene oxide, which involves a  $b_1$ -type intermediate.<sup>24,25</sup> One route to the elimination of  $H_2$  from the  $b_1$  fragment,  $HO(CH_2)_2O^-$ , is shown in Figure 8.4. The terminal oxide ejects the hydride ion from the adjacent carbon atom, and the hydride ion attacks the acidic alcohol proton as it departs, generating  $H_2$  and the anionic aldehyde,  $^-OCH_2(C=O)H$ .<sup>26</sup> Elimination of  $H_2$  from the  $b_2$  fragment at  $m/z$  105 can generate  $m/z$  103, via a similar mechanism with a six-membered transition state. Products from elimination of  $H_2$  were not detected for larger  $b_m$  fragments.

The formation of  $m/z$  43 in Figure 8.3 corresponds to the loss of  $H_2O$  from  $b_1$ . One possible route to dehydration of  $b_1$  involves a charge-remote process, as indicated in Figure 8.5. The alcohol group forms a bond with an alkyl proton to yield water and vinoxide. The formation of vinoxide at  $m/z$  43 is reasonable due to the structural similarity to  $b_1$  and anionic resonance stabilization, so it would be a favorable product. In summary, the negative charge site on PEG opens new decomposition reactions that are not observed upon CID of cationic PEG complexes.

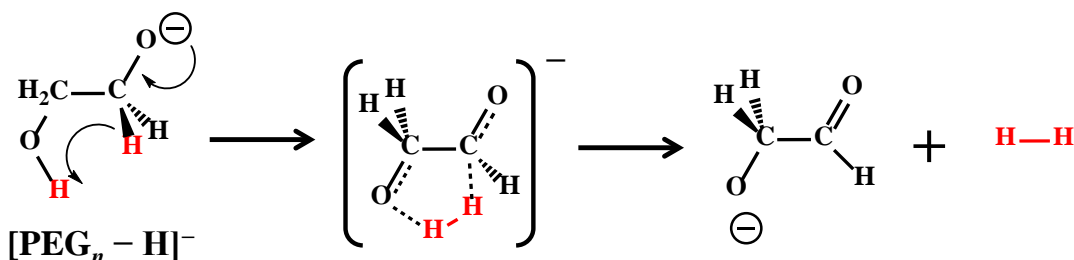


Figure 8.4 Schematic decomposition reaction for loss of  $H_2$  from  $[PEG_n - H]^-$  for  $n = 1, 2$ .

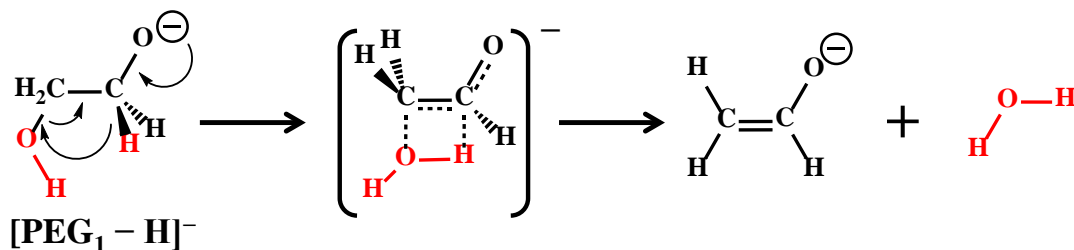


Figure 8.5 Schematic decomposition reaction for loss of  $H_2O$  from  $[PEG_1 - H]^-$ .

## 8.4 Conclusions

This study showed that deprotonated PEG yields rich fragmentation spectra that arise from dissociation reactions involving the terminal oxide position. The small oligomers used in this study yielded fragments corresponding to the loss of multiple monomer units. In general, there is a propensity for the loss of an even number of monomer units over an odd number. This implies sequential dissociation of the precursor ion by elimination of 1,4-dioxane from intramolecular S<sub>N</sub>2 reactions. Some alternative dissociation products were observed for the smaller oligomers, and small oligomer fragments. These reactions correspond to the loss of H<sub>2</sub> and H<sub>2</sub>O, but are much less significant.

## 8.5 References

- [1] Hester, T.H.; Castillo, D.E.; Goebbert, D.J. Fragmentation of Deprotonated Polyethylene Glycols, [PEG – H]<sup>-</sup>. *R. Comm. Mass Spectrom.* **2013**, 27 (14), 1643-1648.
- [2] Nielen, M.W.F. Maldi Time-of-flight Mass Spectrometry of Synthetic Polymers. *Mass Spectrom. Rev.* **1999**, 18 (5), 309-344.
- [3] Schriemer, D.C.; Li, L. Detection of High Molecular Weight Narrow Polydisperse Polymers up to 1.5 Million Daltons by MALDI Mass Spectrometry. *Anal. Chem.* **1996**, 68 (17), 2721-2725.
- [4] Bahr, U.; Deppe, A.; Karas, M.; Hillenkamp, F.; Giessmann, U. Mass Spectrometry of Synthetic Polymers by UV-Matrix-Assisted Laser Desorption/Ionization. *Anal. Chem.* **1992**, 64 (22), 2866-2869.
- [5] Schulten, H.-R.; Lattimer, R.P. Applications of Mass Spectrometry to Polymers. *Mass Spectrom. Rev.* **1984**, 3 (2), 231-315.
- [6] Hanton, S.D. Mass Spectrometry of Polymers and Polymer Surfaces. *Chem. Rev.* **2001**, 101 (2), 527-570.
- [7] Miladinović, S.M.; Kaeser, C.J.; Knust, M.M.; Wilkins, C.L. Tandem Fourier Transform Mass Spectrometry of Block and Random Copolymers. *Int. J. Mass Spectrom.* **2011**, 301, 184-194.
- [8] Montaudo, M.S., *Mass Spectrometry*. John Wiley & Sons, Inc., 2008, p. 299-307.

- [9] Wesdemiotis, C.; Solak, N.; Polce, M.J.; Dabney, D.E.; Chaicharoen, K.; Katzenmeyer, B.C. Fragmentation Pathways of Polymer Ions. *Mass Spectrom. Rev.* **2011**, *30* (4), 523-559.
- [10] Howdle, M.D.; Eckers, C.; Laures, A.M.F.; Creaser, C.S. The Use of Shift Reagents in Ion Mobility-Mass Spectrometry: Studies on the Complexation of an Active Pharmaceutical Ingredient with Polyethylene Glycol Excipients. *J. Am. Soc. Mass Spectrom.* **2009**, *20* (1), 1-9.
- [11] Hilton, G.R.; Jackson, A.T.; Thalassinou, K.; Scrivens, J.H. Structural Analysis of Synthetic Polymer Mixtures Using Ion Mobility and Tandem Mass Spectrometry. *Anal. Chem.* **2008**, *80* (24), 9720-9725.
- [12] Gidden, J.; Wyttenbach, T.; Batka, J.J.; Weis, P.; Jackson, A.T.; Scrivens, J.H.; Bowers, M.T. Poly (Ethylene Terephthalate) Oligomers Cationized by Alkali Ions: Structures, Energetics, and Their Effect on Mass Spectra and the Matrix-Assisted Laser Desorption/Ionization Process. *J. Am. Soc. Mass Spectrom.* **1999**, *10* (9), 883-895.
- [13] Gidden, J.; Wyttenbach, T.; Jackson, A.T.; Scrivens, J.H.; Bowers, M.T. Gas-Phase Conformations of Synthetic Polymers: Poly(ethylene glycol), Poly(propylene glycol), and Poly(tetramethylene glycol). *J. Am. Chem. Soc.* **2000**, *122* (19), 4692-4699.
- [14] Wyttenbach, T.; von Helden, G.; Bowers, M.T. Conformations of Alkali Ion Cationized Polyethers in the Gas Phase: Polyethylene Glycol and Bis[(benzo-15-crown-5)-15-ylmethyl] Pimelate. *Int. J. Mass Spectrom.* **1997**, *165*, 377-390.
- [15] von Helden, G.; Wyttenbach, T.; Bowers, M.T. Conformation of Macromolecules in the Gas Phase: Use of Matrix-Assisted Laser Desorption Methods in Ion Chromatography. *Science.* **1995**, *267* (5203), 1483-1485.
- [16] von Helden, G.; Wyttenbach, T.; Bowers, M.T. Inclusion of a MALDI Ion Source in the Ion Chromatography Technique: Conformational Information on Polymer and Biomolecular Ions. *Int. J. Mass Spectrom.* **1995**, *146*, 349-364.
- [17] Hester, T.H.; McCraney, K.K.; Castillo, D.E.; Goebbert, D.J. The Sequential Dissociation of Protonated Polyethylene Glycols. *J. Mass Spectrom.* **2013**, *48* (4), 459-464.
- [18] Selby, T.L.; Wesdemiotis, C.; Lattimer, R.P. Dissociation Characteristics of  $[M + X]^+$  Ions ( $X = H, Li, Na, K$ ) from Linear and Cyclic Polyglycols. *J. Am. Soc. Mass Spectrom.* **1994**, *5* (12), 1081-1092.
- [19] Lattimer, R.P. Tandem Mass Spectrometry of Poly(ethylene glycol) Lithium-attachment Ions. *J. Am. Soc. Mass Spectrom.* **1994**, *5* (12), 1072-1080.
- [20] Lattimer, R.P. Tandem Mass Spectrometry of Poly(ethylene glycol) Proton- and Deuteron-attachment Ions. *Int. J. Mass Spectrom.* **1992**, *116* (1), 23-36.
- [21] Lattimer, R.P. Tandem Mass Spectrometry of Lithium-attachment Ions from Polyglycols. *J. Am. Soc. Mass Spectrom.* **1992**, *3* (3), 225-234.

- [22] Lattimer, R.P.; Münster, H.; Budzikiewicz, H. Tandem Mass Spectrometry of Polyglycols. *Int. J. Mass Spectrom.* **1989**, *90* (2), 119-129.
- [23] Kalinoski, H.T.; Hargiss, L.O. Collision-induced Dissociation Mass Spectrometry of Nonionic Surfactants Following Direct Supercritical Fluid Injection. *J. Am. Soc. Mass Spectrom.* **1992**, *3* (2), 150-158.
- [24] Blanksby, S.J.; Kato, S.; Bierbaum, V.; Ellison, G.B. Fragmentations of Deprotonated Alkyl Hydroperoxides (ROO<sup>-</sup>) Upon Collisional Activation: A Combined Experimental and Computational Study. *Aust. J. Chem.* **2003**, *56* (5), 459-472.
- [25] Bierbaum, V.M.; DePuy, C.H.; Shapiro, R.H.; Stewart, J.H. Flowing Afterglow Studies of the Reactions of Hydroxide, Amide, and Methoxide Ions with Ethylene Oxide and Propylene Oxide. *J. Am. Chem. Soc.* **1976**, *98* (14), 4229-4235.
- [26] de Hoffmann, E.; Stroobant, V.: *Mass Spectrometry: Principles and Applications*, John Wiley & Sons, Inc., Chichester, 2002.

## CHAPTER 9

### CONCLUSIONS AND OUTLOOK

The majority of studies in this dissertation involve decomposition studies of metal nitrate anion complexes. These studies reveal the importance of metal  $3d$  occupancy and  $3d$  orbital energy level on the redox properties of metal oxides. A representative set of MO diagrams will be provided as a guide for the three disparate regimes of metal oxide redox character. A table is provided that succinctly lists the redox outcomes for the observed losses from each complex.

#### *9.1 Summary of Dissociation Trends*

Metal nitrate complexes decompose primarily via  $\text{NO}_2^\bullet$  loss. The metal cation abstracts  $\text{O}^{\bullet-}$  from a nitrate ligand to form a metal-oxygen bond. The formation of this bond can show evidence of metal oxidation for early transition metals or it can show no metal redox activity for middle-to-late transition and main group metals. Figure 9.1 shows three panels containing the three most representative MO diagrams for the observed outcomes of orbital mixing in metal-oxygen bond formation. Figure 9.1A shows the hypothetical atomic orbital mixing in the formation of  $[\text{CoO}]^+$ . This MO diagram captures the observed redox properties for the chromium and cobalt systems, and is expected to apply for adjacent elements: manganese and iron. These early transition metal complexes were found to undergo metal oxidation upon each  $\text{O}^{\bullet-}$  abstraction, yielding a metal oxide with higher oxidation states for both the metal and oxygen atoms.

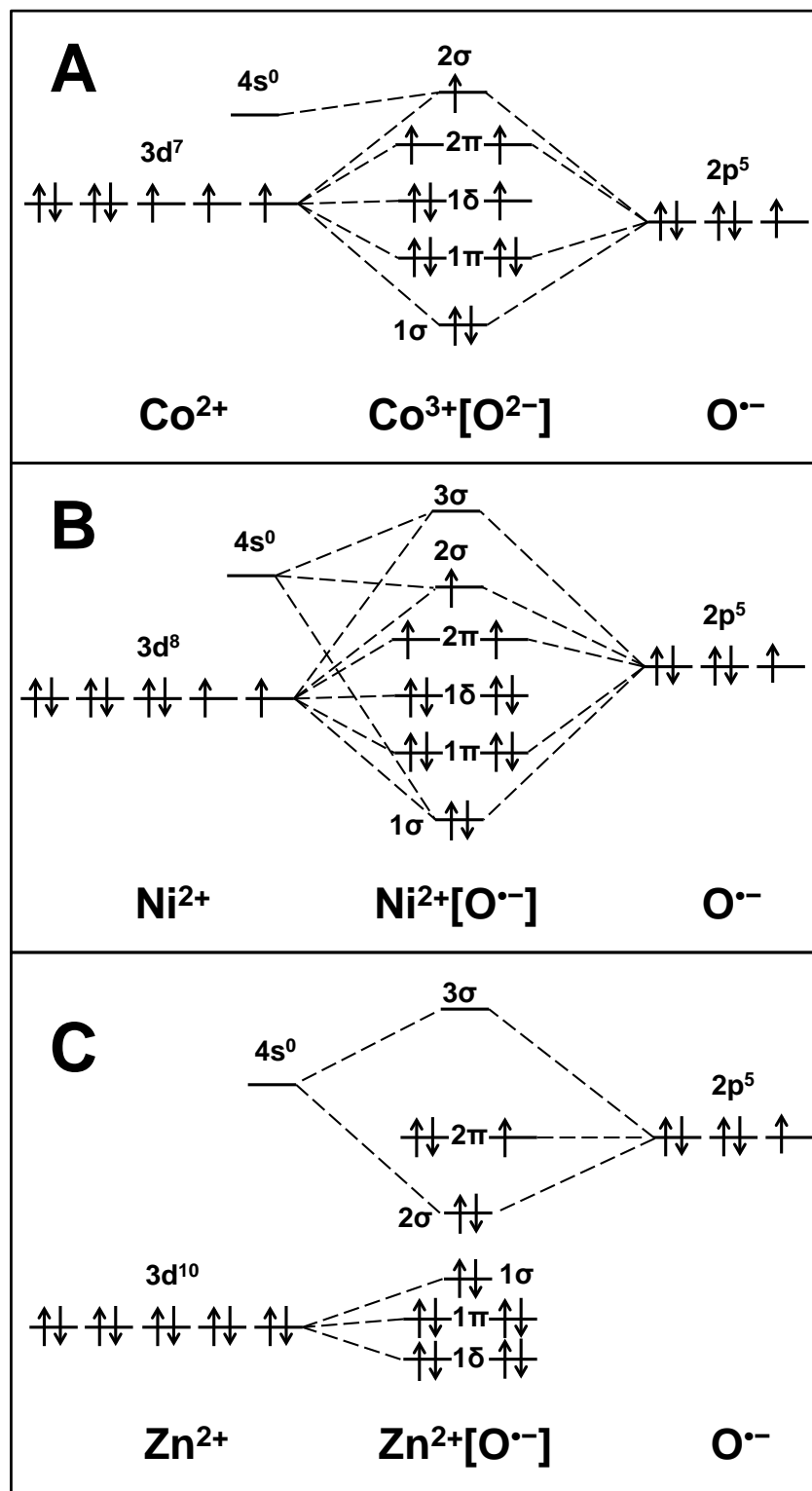


Figure 9.1 Three representative molecular orbital diagrams for metal oxide bond formation in the three redox regimes of the transition metals studied. Panel A shows the hypothetical diagram for [CoO]<sup>+</sup>, panel B shows the hypothetical diagram for [NiO]<sup>+</sup>, and panel C shows the hypothetical diagram for [ZnO]<sup>+</sup>.

Figure 9.1B shows the MO diagram for the formation of  $[\text{NiO}]^+$ . This diagram applies only to the nickel system, since the metal lies in the transition metal series, at the inflection point between two disparate modes of metal-oxygen bond formation. Rather than undergoing metal oxidation, the nickel cation was observed to undergo a slight reduction upon  $\text{O}^{\bullet-}$  abstraction. The slightly lower energy orbital vacancies of the  $\text{Ni}(3d)$  subshell are nearly degenerate with the  $\text{O}(2p)$  orbitals, allowing for delocalization of electron density from the ligand to the metal. The slight delocalization results in a minor contributor to the description of the  $[\text{NiO}]^+$  core as  $\text{Ni}^+[\text{O}]$ . Although the  $\text{Ni}^{2+}[\text{O}^{\bullet-}]$  description represents the major character for the  $[\text{NiO}]^+$  core, the slight neutral character of the oxygen ligand is considered important due to elimination of neutral O atom from the  $[\text{NiO}(\text{NO}_3)_2]^-$  complex.

Figure 9.1C shows the last regime of metal redox activity upon  $\text{O}^{\bullet-}$  abstraction. The MO diagram of  $[\text{ZnO}]^+$  reflects the redox behavior of the late transition and main group metals. A metal-oxygen bond forms upon  $\text{O}^{\bullet-}$  abstraction without any reduction or oxidation of the metal. The metal and ligand ions retain their initial oxidation states due to non-mixing of the very low energy  $3d$  subshell of the metal and the high  $\text{O}(2p)$  orbital energy level.

The dissociation patterns for all metal oxide nitrate complexes in this manuscript can be explained using the MO diagrams of Figure 9.1, taking into account the initial and mixed orbital energies. The frequent losses of  $\text{NO}_3^\bullet$ , atomic oxygen, and molecular oxygen in the metal nitrate anion complexes involve transfer of an electron to the lowest available orbital vacancy. This electron transfer is very well explained using orbital energy considerations from MO diagrams. Electron transfer within late transition and main group metal complexes always results in ligand reduction because the  $\text{O}(2p)$  level is lower than the metal  $4s$  orbital. If no ligand is available, the metal is necessarily reduced. The nickel system is a special case, in which the

transferred electron becomes effectively located in a metal-oxygen  $\pi$ -bond due to atomic orbital near degeneracy. Early transition metals strongly favor  $\text{NO}_2^\bullet$  loss; therefore, they only undergo losses upon electron transfer when the metal oxide complex contains no nitrate ligands. Loss of atomic or molecular oxygen from these complexes is accompanied by electron transfer, and the lowest available orbital vacancy is filled accordingly.

## 9.2 Gallium System

Gallium nitrate complexes have decomposition patterns similar to those observed for the aluminum nitrate system.<sup>1</sup> The two metals are Group 13 elements with the same +3 charge in the precursor complex. These main group metals contain a completely vacant valence  $s$ -orbital, leading to the similar dissociation pattern of the nitrate complexes. Any difference in the dissociation spectra of these complexes lies in the orbital energy of the valence orbital. For instance, the gallium complex,  $[\text{GaO}_2(\text{NO}_3)_2]^-$ , was observed to undergo  $\text{O}_2$  loss to yield  $[\text{Ga}(\text{NO}_3)_2]^-$ . The high sequential intensity observed for this product ion in the CID spectrum of the  $[\text{Ga}(\text{NO}_3)_4]^-$  precursor corresponds to a favorable charge density on the relatively large gallium atom for the product. The analogous sequential dissociation intensity for aluminum nitrate shows an unfavorably higher charge density on the smaller aluminum cation.<sup>1</sup>

Table 9.1 lists the losses for each metal nitrate complex studied. Identifiable differences in the decomposition for these metals are noted. Gallium nitrate complexes undergo multiple losses of  $\text{NO}_2^\bullet$  and  $\text{NO}_3^\bullet$ . All metal systems showed losses of  $\text{NO}_2^\bullet$ , whereas losses of  $\text{NO}_3^\bullet$  occurred only for the late transition and main group metals. Electron transfer from a nitrate ligand results in the elimination of  $\text{NO}_3^\bullet$  from  $[\text{GaO}(\text{NO}_3)_3]^-$  and  $[\text{GaO}_2(\text{NO}_3)_2]^-$  due to the electrostatic attraction of the highly positively charged core in those complexes and the low

energy of the vacant O(2*p*) orbital. Elimination of O<sub>2</sub> from [GaO(NO<sub>3</sub>)<sub>3</sub>]<sup>-</sup> and [GaO<sub>2</sub>(NO<sub>3</sub>)<sub>2</sub>]<sup>-</sup> occur via nitrate isomerization. An oxygen atom from a nitrate ligand is abstracted, generating a new oxygen ligand and a nitrite, NO<sub>2</sub><sup>-</sup>, ligand. Neutral O<sub>2</sub> is eliminated, formally reducing the metal. The highly charged core and low energy 4*s* orbital facilitate the nitrate isomerization and the subsequent metal reduction.

### 9.3 Zinc System

Zinc nitrate complexes<sup>2</sup> decompose very similarly to the gallium and aluminum<sup>1</sup> complexes. The 3*d*<sup>10</sup> electron configuration for Zn<sup>2+</sup> is identical to that of Ga<sup>3+</sup> and of Cu<sup>+</sup>, whereas none of the charges are the same. The copper system dissociates differently than the other late transition and main group metals because electron transfer dominates. The Cu<sup>2+</sup> complex undergoes reduction upon NO<sub>3</sub><sup>•</sup> loss, but the Cu<sup>+</sup> product complex undergoes the expected sequential elimination of NO<sub>2</sub><sup>•</sup>.<sup>3</sup>

All dissociation pathways are very similar between the four systems due to their vacant valence *s*-orbitals. The unusual case in zinc occurs for [ZnO<sub>2</sub>(NO<sub>3</sub>)]<sup>-</sup>. Table 9.1 notes the expected elimination of NO<sub>2</sub><sup>•</sup> is not observed for this zinc complex. The intensity of zinc-containing precursors in the CID spectra are extremely weak, so further CID investigation into the formation of the analogous, hypothetical [ZnO(O<sub>2</sub>)]<sup>-</sup> fragment was impossible. A potential reason for the absence of [ZnO(O<sub>2</sub>)]<sup>-</sup> in all spectra is the favorable, low energy loss of O<sub>2</sub>. Direct elimination occurs via reduction of the low 4*s* orbital of zinc, whereas nitrate rearrangement generates an oxygen ligand that becomes reduced upon O<sub>2</sub> loss. The decomposition of zinc nitrate anion complexes is determined by the full 3*d* subshell and low energy of the 4*s* orbital in zinc and by nitrate ligand isomerization.

Table 9.1 Overview of the dissociation reactions for the metal complexes. Observed losses are listed for each metal complex and the corresponding reduction event is given. The sequential loss of  $\text{NO}_2^\bullet$  is observed for all metals studied, except for the metal complexes listed in that row. Complexes containing no nitrate ligands are labeled as “BARE”.

	Complex				
	$[\text{M}(\text{NO}_3)_x]^-$	$[\text{MO}(\text{NO}_3)_{x-1}]^-$	$[\text{MO}_2(\text{NO}_3)_{x-2}]^-$	$[\text{MO}_3(\text{NO}_3)_{x-3}]^-$	$[\text{MO}_4]^-$
$\text{NO}_3^\bullet$ loss (electron transfer)	<b>Cu:</b> low $3d$ vacancy $3d^9 \rightarrow 3d^{10}$	<b>Ga, Zn:</b> low $2p$ vacancy $\text{O}^{\bullet-} \rightarrow \text{O}^{2-}$  <b>Ni:</b> low $3d, 2p$ vacancy $3d^8[\text{O}^{\bullet-}] \rightarrow 3d^{8.5}[\text{O}^{1.5-}]$	<b>Ga:</b> low $2p$ vacancy $\text{O}^{\bullet-} \rightarrow \text{O}^{2-}$  <b>Ni:</b> low $2p$ vacancy $\text{O}^{\bullet-} \rightarrow \text{O}^{2-}$		
O loss		<b>Ni:</b> low $3d$ vacancy $3d^8 \rightarrow 3d^9$	<b>Co:</b> highly charged metal $3d^5 \rightarrow 3d^7$	<b>Ni:</b> likely but no CID available  <b>Co:</b> BARE low $3d$ vacancy $3d^4 \rightarrow 3d^6$	<b>Cr:</b> BARE low $3d$ vacancy $3d^0 \rightarrow 3d^1$
$\text{O}_2$ loss		<b>Ga, Zn:</b> low $4s$ vacancy nitrate rearrangement $4s^0 \rightarrow 4s^1$	<b>Ga, Zn:</b> low $2p$ vacancy nitrate rearrangement $\text{O}^{\bullet-} \rightarrow \text{O}^{2-}$  <b>Ni:</b> low $3d, 2p$ vacancy nitrate rearrangement $3d^8[\text{O}^{\bullet-}] \rightarrow 3d^{8.5}[\text{O}^{1.5-}]$	<b>Ni:</b> likely but no CID available  <b>Co:</b> BARE low $3d$ vacancy $3d^4 \rightarrow 3d^8$	<b>Cr:</b> BARE low $3d$ vacancy $3d^0 \rightarrow 3d^3$
* $\text{NO}_2^\bullet$ loss ( $\text{O}^{\bullet-}$ abstraction)	<b>Cu:</b> no loss, reduction dominates		<b>Zn:</b> no loss, reduction dominates	<b>Ga:</b> likely but no CID available	

\* Cr through Co: metal oxidation. Ni through Zn (including Ga): no metal redox

#### 9.4 Nickel System

Nickel nitrate complexes do not differ significantly in their decomposition compared to the other late transition metals, but the redox character of the metal oxide bonds is noticeably different.<sup>4</sup> Table 9.1 shows that elimination of O<sub>2</sub> from [NiO(NO<sub>3</sub>)<sub>2</sub>]<sup>-</sup> does not occur, whereas loss of O atom is observed. This complex contains an oxygen ligand with slight neutral character due to the nearly degenerate, pseudo-covalent nature of the mixed Ni(3*d*) and O(2*p*) orbitals. Elimination of atomic oxygen results in metal reduction. Elimination of O<sub>2</sub> is not observed because the low energy vacancies of the Ni(3*d*) subshell in [NiO(NO<sub>3</sub>)<sub>2</sub>]<sup>-</sup> favor the other decomposition pathways.

Elimination of NO<sub>3</sub><sup>•</sup> from [NiO(NO<sub>3</sub>)<sub>2</sub>]<sup>-</sup> yields a product complex, [NiO(NO<sub>3</sub>)]<sup>-</sup>, containing a neutral NiO core best described as Ni<sup>1.5+</sup>[O<sup>0.5-</sup>]. An electron effectively lies equally on both atoms of the metal oxide core due to the near degeneracy of the nickel and oxygen valence orbitals. The competitive elimination of NO<sub>2</sub><sup>•</sup> from [NiO(NO<sub>3</sub>)<sub>2</sub>]<sup>-</sup> yields [NiO(NO<sub>3</sub>)<sub>2</sub>]<sup>-</sup>. This intermediate undergoes nitrate isomerization to eliminate O<sub>2</sub>, yielding [NiO(NO<sub>2</sub>)]<sup>-</sup> with the same neutral NiO core of [NiO(NO<sub>3</sub>)]<sup>-</sup>. The nickel nitrate system is the earliest in the transition metal series that shows a wide variety of dissociation routes in the decomposition scheme. The decomposition of nickel nitrate complexes is primarily controlled by the low energy of the O(2*p*) orbitals of the unique oxygen ligands. These ligands are typically radical oxygen anions that drive the many observed dissociation reactions. The low energy vacancies in the Ni(3*d*) subshell were found to contribute significantly to the redox character of the nickel oxides and to the unusual O atom loss from [NiO(NO<sub>3</sub>)<sub>2</sub>]<sup>-</sup>.

## 9.5 Cobalt System

Cobalt nitrate complexes undergo dissociation most similar to that observed for the previously studied chromium nitrate system. Cobalt is the latest transition metal that undergoes regular metal oxidation upon  $O^{\bullet-}$  abstraction, and only undergoes metal reduction upon elimination of O or  $O_2$ . Table 9.1 shows the unique dissociation qualities of cobalt oxide nitrate complexes. The cobalt-containing complex,  $[CoO_2(NO_3)]^-$ , undergoes the surprising elimination of atomic oxygen. The extremely high charge of +4 for the cobalt cation in  $[CoO_2(NO_3)]^-$ , along with the relatively low energy of the  $3d$  subshell, facilitates double electron transfer from an  $O^{2-}$  ligand to the metal upon O atom loss. The analogous loss of O atom from  $[CrO_2(NO_3)_2]^-$  was not observed, despite the high charge of +5 for chromium, because of the much higher energy of the  $Cr(3d)$  subshell.<sup>5</sup> The cobalt and chromium oxide anions were observed to undergo competitive losses of O and  $O_2$ . Additional theoretical calculations on the chromium system, beyond what are provided in the published manuscript, show  $[CrO_4]^-$  undergoes O atom elimination to yield  $[CrO_3]^-$  at 3.27 eV and  $O_2$  elimination to yield  $[CrO_2]^-$  at 3.66 eV. The analogous losses of O and  $O_2$  from  $[CoO_3]^-$  to yield  $[CoO_2]^-$  and  $[CoO]^-$  occur at 3.76 eV and 4.12 eV, respectively. The cobalt system behaves very similarly to the chromium system, differing only in the  $3d$  orbital energy level of the metal.

## 9.6 Future Outlooks

The research presented in this dissertation is primarily focused on the decomposition of metal nitrate anion complexes. Other ligands can be studied, especially small organic ligands such as acetate and acetylacacetate. These ligands are frequently used in solution-phase transition metal catalyst systems and may be involved in redox processes in those experiments. It would

be very interesting to extend our work of synthesizing metal oxides from metal nitrate complexes into mixed ligand systems. The reactivity of radical oxygen ligands with organic ligands can be investigated and may give insight into catalytic carbon activation and atom insertion into bonds. Our group has obtained preliminary data on the reactivity of radicals within these metal oxide nitrate complexes using ion-molecule reactions. Further research in this area could be useful in experimentally supporting theoretical claims of radical character for specific atoms.

### 9.7 References

- [1] Lightcap, J.; Hester, T.H.; Kamena, K.; Albury, R.M.; Pruitt, C.J.M.; Goebbert, D.J. Gas-Phase Fragmentation of Aluminum Oxide Nitrate Anions Driven by Reactive Oxygen Radical Ligands. *J. Phys. Chem. A* **2016**, *120* (9), 1501-1507.
- [2] Hester, T.H.; Goebbert, D.J. Experimental and Theoretical Study of the Decomposition of  $[\text{Zn}(\text{NO}_3)_3]^-$ . *Chem. Phys. Lett.* **2016**, In Press.
- [3] Pruitt, C.J.M.; Goebbert, D.J. Experimental and Theoretical Study of the Decomposition of Copper Nitrate Cluster Anions. *J. Phys. Chem. A* **2015**, *119* (20), 4755-4762.
- [4] Hester, T.H.; Albury, R.M.; Pruitt, C.J.M.; Goebbert, D.J. Fragmentation of  $[\text{Ni}(\text{NO}_3)_3]^-$ : A Study of Nickel-Oxygen Bonding and Oxidation States in Nickel Oxide Fragments. *Inorg. Chem.* **2016**, *55* (13), 6634-6642.
- [5] Albury, R.M.; Pruitt, C.J.M.; Hester, T.H.; Goebbert, D.J. Fragmentation of  $\text{Cr}(\text{NO}_3)_4^-$ : Metal Oxidation upon  $\text{O}^+$  Abstraction. *J. Phys. Chem. A* **2015**, *119* (47), 11471-11478.

## APPENDIX

The following program code was written for use by the Xcalibur software on the TSQ-7000 to automate the collection of ERMS data. Each line is numbered as a visual aid. The “runerms” program opens dialog boxes asking for the precursor  $m/z$ , the fragment  $m/z$ , the voltage step increment, the collision voltage range, and the number of total scans to perform. The “runerms” program opens a subprogram, either “prog4neg” for negative mode or “prog4pos” for positive mode. The subprogram puts the instrument in ERMS mode to monitor the intensity of the fragment  $m/z$ , and plots it on a graph in the software window while recording the values for data export.

### **runerms**

1. vmake: .#an: .#qu: .#pr: DAU: uclr: initg
2. nask(0, 1): .#precmass?: .sm: .#ulist(1, 1)=\$
3. REPEAT 5: precmass=ulist(1, 1): END
4. nask(0, 1): .#fragmass?: .dfm+0.5: .#ulist(1, 1)=\$
5. REPEAT 5: fragmass=ulist(1, 1): END
6. nask(0, 1): .#vstep?: .#1/2: .#ulist(1, 1)=\$
7. REPEAT 5: vstep=ulist(1, 1): END
8. REPEAT 5: coff=(pos-neg)\*(10): END
9. nask(0, 1): .#initcoff?: .coff: .#ulist(1,1)=\$
10. REPEAT 5: initcoff=ulist(1, 1): END

```

11. REPEAT 5: coff=(neg-pos)*(50): END
12. nask(0, 1): .#fincoff?: .coff: .#ulist(1,1)=$
13. REPEAT 5: fincoff=ulist(1, 1): END
14. nask(0, 1): .#howmany?: .#5: .#ulist(1,1)=$
15. REPEAT 5: howmany=ulist(1, 1): END
16. GTITLE: ..#Running ERMSs of : ..precmass: ..#to: ..fragmass
17. uclr: initg: vmake(4): .#an: .#ul: .#pr: .#gr
18. if neg=1: prog4neg
19. else: prog4pos

```

### **prog4neg**

```

1. doze 4: loopstart=STIME: startcoff=initcoff-6*vstep
2. DAU(precmass, fragmass-0.5, fragmass+0.5, 1, startcoff)
3. GTITLE: ..precmass: ..#to: ..fragmass: ..# ERMSs (: ..howmany: .#)
4. vsend: .#analysis: .#sn=0
5. uclr 1: uclr 2
6. %1=ulist(1, 4): %1+=1: uins(%1, 1, 4)
7. if dau: when stime>=loopstart+800
8. REPEAT: dau(precmass, fragmass-0.5, fragmass+0.5, 1, startcoff)
9. q1ms: dau
10. until abs(umax-fincoff)<=0.5*vstep
11. coff=initcoff+(usize(1)-6)*vstep
12. SCN: UAPP(COFF, 1): UAPP(mean, 2)
13. PLOT(ULIST(USIZE(1), 1), ULIST(USIZE(2), 2), %1+1)
14. if umax>=initcoff-4.5*vstep: vsend: .#analysis: astart
15. if usize>=7+(abs(fincoff-initcoff)/vstep)

```

```

16. vsend: .#analysis: lstop
17. if %1>=howmany: doze 5: vsend: .#analysis: .#sn=1: abort: else
18. until stime>=loopstart-500+abs(fincoff-initcoff)*10/vstep
19. doze: END: prog4neg: END: END: END: END: END: END: END: END

```

### **prog4pos**

```

1. doze 4: loopstart=STIME: startcoff=initcoff+6*vstep
2. DAU(precmass, fragmass-0.5, fragmass+0.5, 1, startcoff)
3. GTITLE: ..precmass: ..#to: ..fragmass: ..# ERMSs (: ..howmany: ..#)
4. vsend: .#analysis: .#sn=0
5. uclr 1: uclr 2
6. %1=ulist(1, 4): %1+=1: uins(%1, 1, 4)
7. if dau: when stime>=loopstart+800
8. REPEAT: dau(precmass, fragmass-0.5, fragmass+0.5, 1, startcoff)
9. q1ms: dau
10. until abs(umin-fincoff)<=0.5*vstep
11. coff=initcoff-(usize(1)-6)*vstep:
12. SCN: UAPP(COFF, 1): UAPP(mean, 2)
13. PLOT(ULIST(USIZE(1), 1), ULIST(USIZE(2), 2), %1+1)
14. if umin<=initcoff+4.5*vstep: vsend: .#analysis: astart
15. if usize>=7+(abs(fincoff-initcoff)/vstep)
16. vsend: .#analysis: lstop
17. if %1>=howmany: doze 5: vsend: .#analysis: .#sn=1: abort: else
18. until stime>=loopstart-500+abs(fincoff-initcoff)*10/vstep
19. doze: END: prog4pos: END: END: END: END: END: END: END: END

```